2017-04-07

Engineering SIBS for Biomedical Applications: Effects of Composition, Processing Parameters, and Lipid-Induced Degradation

Mauro Fittipaldi
University of Miami, maurofittipaldi1@gmail.com

UNIVERSITY OF MIAMI

ENGINEERING SIBS FOR BIOMEDICAL APPLICATIONS: EFFECTS OF COMPOSITION, PROCESSING PARAMETERS, AND LIPID-INDUCED DEGRADATION

By

Mauro Fittipaldi

A DISSERTATION

Submitted to the Faculty
of the University of Miami
in partial fulfillment of the requirements for
the degree of Doctor of Philosophy

Coral Gables, Florida

May 2017

UNIVERSITY OF MIAMI

A dissertation submitted in partial fulfillment of
the requirements for the degree of
Doctor of Philosophy

ENGINEERING SIBS FOR BIOMEDICAL APPLICATIONS: EFFECTS OF COMPOSITION, PROCESSING PARAMETERS, AND LIPID-INDUCED DEGRADATION

Mauro Fittipaldi

Approved:

_____
Michael R. Swain, Ph.D.
Associate Professor
Mechanical and Aerospace Engineering

_____
Landon R. Grace, Ph.D.
Assistant Professor
North Carolina State University

_____
Emrah Celik, Ph.D.
Assistant Professor
Mechanical and Aerospace Engineering

_____
Guillermo Prado, Ph.D.
Dean of the Graduate School

_____
Leonard Pinchuk, Ph.D.
Research Professor
Biomedical Engineering

FITTIPALDI, MAURO (Ph.D., Mechanical Engineering)
Engineering SIBS for Biomedical Applications: (May 2017)
Effects of Composition, Processing Parameters,
And Lipid-Induced Degradation

Abstract of a dissertation at the University of Miami.

Dissertation supervised by Professor Landon R. Grace.
No. of pages in text. (131)

Poly(Styrene-block-Isobutylene-block-Styrene) (SIBS) is a biocompatible thermoplastic elastomer used extensively in the biomedical field. The outstanding biocompatibility and tailorability of this material make it an ideal candidate for a wide range applications. From coating applications in coronary stents to ophthalmic devices for glaucoma treatment, SIBS has shown great potential in many devices. In this work, the use of SIBS in prosthetic applications is investigated, along with the requisite analysis of material relaxation to better understand long-term performance. An efficient, low-cost, automated, novel method to fabricate orbital prosthesis based on non-contact facial topography mapping and 3-D printing is proposed and validated. The virtual anatomy map is reconstructed and manipulated in order to create a perfectly symmetric, custom fitting virtual prosthesis and its subsequent negative mold for injection molding. This method is the first of its kind to allow the use of thermoplastic elastomers for the fabrication of orbital prosthesis, allowing the prosthesis to last longer and be repaired instead of having to be discarded and refabricated. A SIBS thermoplastic elastomer is selected for the application due to its exceptional biocompatibility. The patient commented on the more comfortable fit and the closer matching symmetry of the 3D printed prosthesis compared to the conventional silicone casted prosthesis. A fluid-immersed, electromagnetically driven, dynamic ocular piece is also proposed for the orbital prosthesis. An infrared camera that

captures the contralateral pupil is used to detect the position of the healthy eye and maps the dynamic ocular piece for real-time synchronized movement of the prosthesis. The device showed potential for usage in ocular prosthesis, surpassing human saccade speeds and achieving the necessary rotations to simulate the human eye.

Fabrication and material plasticization were also analyzed in order to maximize material performance for prosthetic applications. A Taguchi method coupled with a Response Surface Methodology and Artificial Neural Network are used to determine the optimal injection molding parameters of SIBS for maximum tensile strength. Optimized validation samples tensile strengths are predicted with errors of less than 3% and 2.55% respectively. Lipid uptake is analyzed via gravimetric measurements in SIBS by simulated immersion in triglycerides. The effect of molecular weight and relative styrene content are used to predict diffusion behavior of SIBS based on a first order polynomial model. Saturation lipid content was inversely related to polystyrene content and molecular weight. Diffusion showed slight non-Fickian behavior due to relaxation and plasticization effects of the polymer network. Swelling and degradation due to polymer relaxation and plasticization are analyzed in order to predict performance in long-term in vivo applications. SIBS is contaminated up to various lipid saturation contents in order to characterize mechanical and viscoelastic behavior with lipid exposure. Plasticization is fully analyzed via uniaxial tension, stress relaxation, dynamic creep, microscopy and spectroscopy. New degradation mechanisms are observed and described that explain the mechanics of lipid-induced plasticization in SIBS. Higher molecular weight showed slower lipid-induced plasticization, potentially allowing an ultra-high molecular weight SIBS be used for load bearing applications without sacrificing biocompatibility with particle

reinforcements. A hyperelastic material model is used to model the mechanical behavior of contaminated SIBS and used to predict long-term performance in lipid-rich environments using a coupled diffusion-swelling finite element method approach. This novel method to calculate swelling coefficient can be readily expanded to different material systems and allows more accurate evaluation of lipid-induced relaxation.

To Emilse Mandolesi and Ricardo Bara

Acknowledgements

First and foremost, I would like to thank my advisor Dr. Landon Grace, without whom this work would not have been possible. Thank you for your guidance and for always expecting the highest possible standard. And most of all, thank you for not allowing me to give up when situations or results were most adverse.

I would also like express my eternal gratitude to Cristina Maria Andrade-Feraud, for all your relentless support and motivation to keep moving forward. I would not have been able to accomplish this work without you, so this work is also your accomplishment.

Finally, to the support of my friends and family throughout the entire endeavor, without whom this work would not be a reality. I am blessed with such wonderful people in my life, so thank you very much for all always being a pillar when I needed one.

Table of Contents

List of Figures

List of Tables

Chapter 1

Problem Statement

Although the work described here is primarily driven by a specific application of Poly(Styrene-block-Isobutylene-block-Styrene) (SIBS), the knowledge developed is broadly applicable to the use of SIBS in a wide range of biomedical applications. The methodologies and concepts covered here apply to any biomaterial system and is not limited to SIBS, hence this knowledge can improve long-term analysis of any implantable device. The practical impetus behind this work is in the field of ophthalmology, where loss or absence of an eye and orbital region caused by a tumor, trauma or congenital defects are extremely distressful and can severely affect human interactions. The most common rehabilitation method utilized are orbital prostheses. Although fabrication of a high quality facial prosthesis is not a simple task, as it is a multiple step process that requires several visits of the patient to a highly skilled artist that will craft the prosthesis by hand, making the process extremely expensive [1]. Moreover, all techniques available today make use of thermosetting silicone elastomers or similar room temperature vulcanizing materials, which are not ideal materials due to their susceptibility to ultraviolet (UV) light, sweat, facial oils and/or dirt. The unsuitability of these materials for long term use due to their discoloration, degradation and nonrepairability is stated almost ubiquitously on every facial prosthetic publication [1-6].

Computer aided design (CAD) efforts have been previously made in order to produce high quality prostheses in a rapid manner [7-10]. However, none of the reports in the literature describe a completely automated process from digital data to prosthesis fabrication in a single appointment with the patient. Some projects report manually

determining the facial symmetry plane of the patient, while others do not make use of the defect topography, or in some cases wax models are still produce lengthening and complicating the entire process. Moreover, all reported methods rely on silicone elastomers, which are not well suited for facial prosthesis as they are prone to degrading and discoloring in very short time frames (1-2 years) [2].

Another existing problem with orbital prosthesis is the lack of mobility of the ocular piece. Current prosthesis design does not allow for movement of the ocular piece nor blinking of the prosthetic eyelid. This brings attention to the prosthesis while interacting with a patient. The development of a dynamic ocular piece is very constrained due to its critical location in the orbital socket. Some of these constraints are minimal vibration, minimal heat dissipation, quiet operation, ultra-low response times, high movement speed and acceleration, low battery consumption, and minimal size (approximately 1 inch in diameter). These make a dynamic ocular piece a challenging, yet fascinating, biomedical device to design.

A biocompatible elastomer

Fabricating orbital prosthesis via injection molding allows for the use of thermoplastic elastomers. Thermoplastic elastomers are much better suited for prosthetic applications compared to silicone rubbers because they provide softer characteristics, are repairable and have better long-term performance. Hence, selection of the best possible material is extremely important to ensure the best performance of the prosthesis. After careful consideration, the selected material for this work was SIBS.

SIBS is a thermoplastic elastomer with a phase-separated morphology that shows a very high degree of biocompatibility. With almost no foreign body reaction produced when

implanted in the human body, SIBS is an ideal candidate for uses in biocompatible coatings and/or as the load-bearing structure in implantable devices [11-15]. The high compatibility and in vivo stability of SIBS is attributed to the absence of cleavable moieties and lack of groups that suffer oxidation, hydrolysis or enzymatic cleavage such as esters, amides, ethers, carbamates, urea, and others. SIBS is also hemocompatible and has been used in drug-eluting coating applications [15-17]. In addition to this excellent biocompatibility, SIBS can be tailored to achieve different mechanical properties based on the styrene/isobutylene ratio and molecular weight. A simplified chemical structure of SIBS with no chemical initiator can be seen in Figure 1.

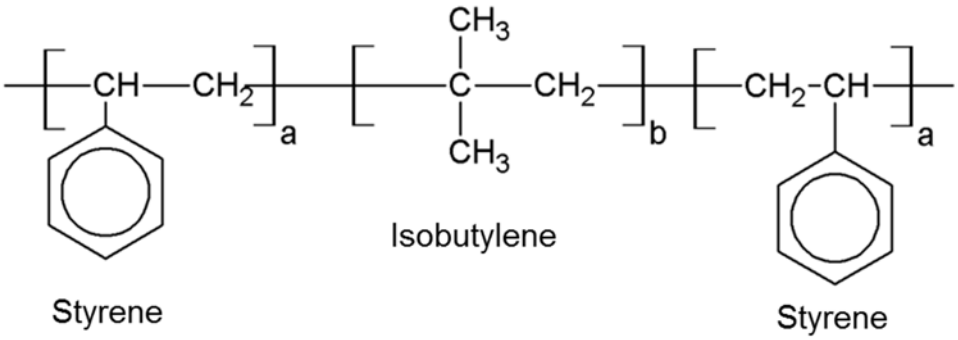

Figure 1-Simplified chemical triblock structure of SIBS

The styrene phase and isobutylene phase are incompatible, and the resulting morphology is a separated styrene domain that varies in shape and size depending on composition [14, 18-21]. St. Lawrence et al. [22] performed a microstructure characterization of SIBS and found that at lower mass fractions of styrene, the styrene forms spherical structures throughout the polymer. At higher styrene contents, the spherical domains become cylindrical and then become double gyroid structures, and at even higher weight percentages these structures become lamellar. Figure 2 depicts a low styrene content SIBS with a spherical styrene domain. Circles represent hard polystyrene

spherical domain, and lines represent the soft isobutylene domain. Tailorability of SIBS is a great asset, as mechanical properties can be adapted for specific applications. Extensive work has been done to characterize different SIBS properties based on molecular weight and polystyrene content [23, 24]. Varieties with lower relative styrene content have a mechanical response similar to that of a rubber, whereas formulations with a higher relative styrene content behave like a toughened plastic [19, 20, 22, 25, 26]. As a result, SIBS is suitable for a wide range of applications with different mechanical requirements without sacrificing biocompatibility. Other types of SIBS have also been studied to determine the effect of different polymer network structures. Arborescent or hyperbranched networks were explored to modify mechanical properties without the need of using fibers or other type of fillers [27, 28]. These materials demonstrated improved solvent resistance because of the increased network rigidity and were capable of achieving higher elongations with similar tensile strength. Furthermore, the effect of carbon fillers have also been studied in different SIBS polymers [29, 30], showing promising results with improved thermal properties and retaining good biological implantation performance. Other benefits of thermoplastic elastomer materials, like SIBS, is that they can be thermoformed via standard molding processes, thereby significantly reducing manufacturing or environmental cost. This also allows the material to retain rubbery properties at room temperature after processing or sterilizing, making it highly desirable in the biomedical field.

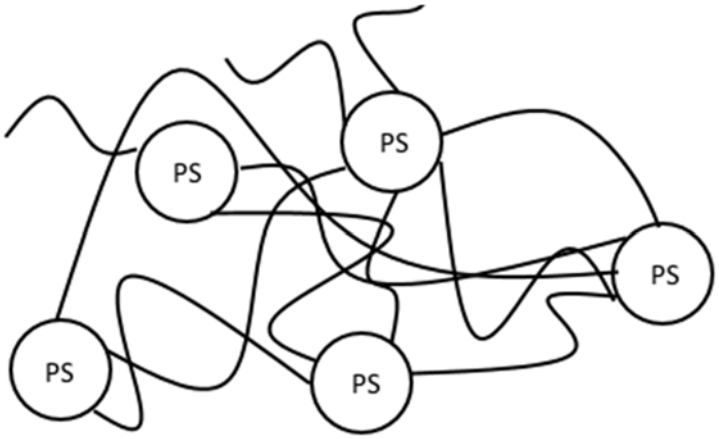

Figure 2-SIBS microstructure

Together, these characteristics form a strong argument for the use of SIBS in biomedical applications, regardless of the mechanical requirements of any particular application. SIBS has been successfully used in the biomedical industry, and has been the focus of many studies. Some application examples are the drug eluting stents such as the TAXUS^{TM} stent [11, 15], and a microshunt to treat glaucoma [31]. Moreover, SIBS has shown promise for uses as alternatives to silicone breast implants [32]. Due to its excellent biocompatibility and its tailorability to different mechanical properties, SIBS is the selected material for this work. The developed method for rapid orbital prosthesis fabrication was designed in order to fabricate a SIBS-based prosthesis. In order to fully exploit the benefits of a thermoplastic elastomer, the selected fabrication process is plastic injection molding. The conventional fabrication process for silicone based prosthesis is room temperature vulcanization, however this process can take more than 24 hours to fabricate one prosthesis depending on the type of silicone used. Injection molding allows for quick repeatability of the prosthesis, with a fabrication time of less than 10 minutes to produce one.

Background on plastic injection molding

Understanding the fabrication process is extremely important for producing high quality prosthesis. Inconsistencies or impurities in the fabrication process can lead to prosthesis with defects that are unusable or weakened mechanical properties the render the prosthesis unusable in a short period of time. Hence it is extremely important to understand the processing conditions of SIBS to ensure proper prosthesis fabrication. Plastic injection molding (PIM) is one of the most common manufacturing techniques for thermoplastics, and the selected fabrication method for this work. Its main advantages are fast production of parts, material and color flexibility, little to no waste and low labor costs. PIM consists of a screw or a ram that compresses plastic pellets and extrudes the plastic through a heated nozzle. As the thermoplastic heats up, it starts flowing and mixing with other pellets. The plastic flow is injected under high pressure into a mold with a cavity of the desired product. Once the injection is finalized, the mold is allowed to cool down until the plastic solidifies again. Once the plastic is cooled down to a desired temperature, the mold is opened and the part is obtained from the mold. In this work, the injection molder used was a Galomb benchtop injection molder. This setup is a hobby-level injection molder equipment and does not have injection control capability. Thus the injection molder was modified to be used with a 1000 pound linear actuator to precisely control the injection rate. Figure 3 shows a picture of the benchtop injection molder with its temperature controller. The ram clevis was detached from the handle and connected to the linear actuator for direct injection control.

Figure 3-Benchtop injection molder

There are a few disadvantages to this process that make it unsuitable for certain applications, such as the high initial tooling cost, design restrictions and complex process parameters that affect the performance of the product. Among these process parameters are nozzle temperature, mold temperature, injection speed, holding time, holding pressure and cooling time [33, 34]. Each parameter is very delicate, and improper parameter selection interrupts the process, for example a low nozzle temperature could lead to insufficient plastic flow and solidification of plastic before filling the mold entirely. The complexity of the PIM process is exacerbated not only by the sheer number of variables affecting material properties, but also by the relationships among these variables. In order to deal with this complexity, many studies have employed design of experiment and engineering optimization techniques to better understand PIM, to minimize defects during production, or to maximize desired product characteristics [35-43]. For example, Altan investigated the effect of PIM parameters on shrinkage utilizing the Taguchi method, analysis of variance and artificial neural networks (ANN). Polypropylene and polystyrene

were measured experimentally and the process parameters for minimum shrinkage were found [44]. Using both techniques it was possible to minimize shrinkage to 0.937% and 1.224% for polypropylene and polystyrene respectively. Mamaghani et al. also employed the Taguchi method design of experiment in order to maximize tensile strength and hardness of an Acrylonitrile Butadiene Styrene (ABS) organoclay composite. Optimal Taguchi parameters produced a nanocomposite with an improvement of 11.5% in ultimate tensile strength and 8.5% in Rockwell hardness compared to that of the base material [43]. In another example of PIM optimization, Farshi et al. simulated warpage and shrinkage defects of a polyethylene automobile ventiduct grid. Using a sequential simplex algorithm, process parameters were optimized to minimize shrinkage and warpage [45]. Further insight into PIM optimization was provided by Tzeng et al., who proposed response surface methodology (RSM) and genetic algorithms coupled with ANN to optimize injection molding parameters for maximum strength and impact resistance of a Polycarbonate composite [46]. Both methods proved to be effective predictors and optimizers of injection molding parameters. Parameter optimization methods have also been divided into stages. Chen et al., for example, proposed a two-stage method for optimizing multi-input multi-output PIM processes. In the first stage, Taguchi methods were coupled together with ANN and genetic algorithms in order to reduce process variance. The second stage of the method integrated particle swarm optimization in order to find final optimal process parameters [47]. Experimental results not only showed that the process satisfied quality requirements but also improved process stability. In a separate study, Chen et al. made use of Taguchi methodology for parameter selection and neural networks coupled with genetic algorithms in order to search for optimized responses [48]. It was proposed that this approach was able

to solve multiple-input multiple-output optimization problems. Using the coupled procedure it was possible to maximize quality based on weight and length of the injection molded parts.

Thorough understanding of PIM process parameters is of fundamental importance to fabricate orbital prosthesis. Prosthesis are required to have ultra-thin edges to better hide the prosthesis-skin interface. If the edges are too thick, the prosthesis will be noticeable and the patient will not be comfortable wearing it. Hence, it is necessary to determine the optimal process parameters in order to minimize edge thickness and edge warping. No experimental study has been previously reported for injection molding optimization of SIBS, and the observed responses for this material showed a high degree of variation, making this optimization process an important step to improve prosthesis quality.

Lipid absorption

Biological implantation conditions can be extremely harsh on material performance and longevity, and are extremely complex due to the multiphysics involved in such scenarios. The presence of lipids in the immediate environment of the implant, or prosthesis, and the nearly universal deleterious response of the polymer further complicates material performance predictions. The well-known Fick's laws of diffusion are the most fundamental theoretical models to understand and predict mass transport systems. The first law states the flux moves from regions of high concentration to regions of low concentration with a magnitude proportional to the concentration gradient. This can be written in the following mathematical form:

$$\boldsymbol{J} = -D\nabla\phi \tag{1}$$

Where $\boldsymbol{J}$ denotes the diffusion flux vector, D is the diffusion coefficient, ∇ is the gradient operator and φ is the concentration. Fick's second law relates the concentration varies with time due to the movement of diffusing particles. The following equation shows Fick's second law of diffusion.

$$\frac{\partial \phi}{\partial t} = D\nabla^2\phi \tag{2}$$

Where ∇^2 is the Laplacian, and time is represented by t. Extensive literature is available regarding the diffusion of particles in polymer systems.

Significant effort has been devoted to understanding the kinetics of mass transport in polymers and the degrading effects of absorbed fluids on mechanical and chemical properties [49-51]. Understanding the fundamental mechanisms of mass transport is extremely important to fully understand long-term behavior of materials and to predict lifespan performance. Equations (1) and (2) have been applied widely and to a variety of different polymeric systems that are exposed to moisture [50, 52-59]. Non-Fickian models have also been proposed to explain diffusion mechanisms where the penetrant interacts chemically or physically with the matrix. These models are especially useful when polymer relaxation and plasticization modify diffusion dynamics and the Fickian model fails to predict material performance [50, 60-66]. Soft materials, such as rubbers and hydrogels, usually exhibit more complicated fluid uptake behavior because of coupled relaxation and swelling of the polymer network. Due to the ubiquitous nature of water, most work has focused on this fluid to characterize diffusion in polymeric materials. As a result, there is a general lack of information related to lipid transport in biomedical materials despite an awareness of the plasticizing effects lipids have on polymers. Moreover, gravimetric fluid

uptake procedures are well defined for water immersion studies, but there is no defined or widely-used protocol for lipids or other non-volatile fluids.

In a previous study, Fourier transform infrared attenuated total reflectance (FTIR-ATR) was used to characterize diffusion of water in SIBS, and it was observed that the diffusion coefficient decreased with increasing styrene content [67]. Although there is a study of water diffusion in SIBS and sulfonated SIBS membranes, there is no comprehensive study of lipid diffusion in SIBS. This is extremely important for this study due to the presence of lipids in human sebum secreted by the sebaceous gland [68], and the well-known degradation of silicone in orbital prosthesis due to facial skin oils.

Ultrahigh molecular weight polyethylene (UHMWPE) was the focus of several studies related to the effects of lipid uptake. Squalene, a lipid present in synovial fluid, was found to accelerate the oxidation and degradation mechanisms that UHMWPE undergoes in vivo. The cross link density of UHMWPE was significantly affected by the presence of the unsaturated fatty acid in the polymer network [69]. Puppulin et al. studied the microstructural changes in UHMWPE due to accelerated aging and lipid absorption by spectroscopic characterization. It was found that the presence of lipids accelerated the oxidation-induced recrystallization in all types of UHMWPE studied [70]. Furthermore, it was found that degradation could occur even without the presence of free radicals in the polymer matrix. Squalene was used to simulate ageing of UHMWPE joint replacements and it was observed that maximum degradation was localized at the surface, where lipid concentration is largest [71]. Biodurability of another implantable polymer, polyurethane urea, was also studied by simulated ageing of physiological fluids in vitro using a palm oil solution. Results showed that although being stable in a lipid medium, a significant

degradation occurs due to the plasticization effects of lipids; tensile strength, elongation at break, elastic modulus and hardness of the polymer decreased [72]. Takahara et al. studied the effect of lipid immersion on fatigue behavior and micro phase plasticization in biomedical segmented poly(urethaneureas). It was found that higher hard phase aggregation was needed to reduce lipid absorption and delay degradation. The presence of lipids in the polymer matrix induced the formation and propagation of cracks as well as plastic deformation in the matrix [73, 74].

SIBS has been thoroughly investigated for use in artificial polymeric heart valve applications [75, 76]. The in vitro performance of SIBS was comparable to that of mechanical heart valves and porcine bioprosthetic tissue valves. The thrombogenic potential of SIBS heart valves were very similar to the other heart valves. The mechanical performance of SIBS also showed potential for use in heart valves when fiber reinforcements were used to improve fatigue properties and tensile properties. However, SIBS suffers lipid-induced plasticization that leads to surface cracking in vivo. The final study on the SIBS trileaflet heart valve that was implanted on sheep failed due to lipids deteriorating the polymer network [77]. Out of the six animals, only one with a SIBS heart valve reached the end of the study after 20 weeks. The three other sheep with SIBS heart valves died at 6, 6.5 and 10 weeks due to material failure or myocardial infarction. The study revealed deformation and cracks on the leaflets which were attributed to lipid-induced plasticization, although no confirmation work has been performed. The cracks exposed the polyethylene terephthalate (PET) reinforcing fibers, leading to calcification and failure of the device. The experiment concluded that in its current state SIBS must be improved to provide structural integrity in load-bearing applications. However, no work

has been performed to determine the root-cause of the problem and to characterize this lipid-induced degradation mechanism. Understanding this relaxation is extremely important to further develop SIBS (or similar materials) properties to withstand load bearing applications, or to point at possible reinforcements that could hinder the mechanical degradation of SIBS. This present gap in scientific knowledge is the key to unlocking the full potential of biocompatible materials for polymeric heart valves and other load-bearing implants. The aforementioned research efforts are part of a larger trend indicating that saturated and unsaturated fatty acids have extreme degrading effects on different types of polymers used in biomedical applications. Therefore, there is a significant and currently unmet requirement to fully characterize the susceptibility of these materials to lipid absorption and the associated plasticization, thereby enabling better material selection and longevity predictions for in vivo conditions.

This issue is of extreme importance to the development of prosthetic applications because of the ultra-thin prosthetic edges. It has been reported that on average, maxillofacial prostheses have to be remade or refurbished every 1.5 to 2 years [6], and the main affected area is the prosthetic edge. Thin edges are susceptible to more degradation due to contact with facial oils, humidity, dirt, and UV exposure. Hence, understanding absorption and plasticization mechanisms in polymers is extremely important yet there is very little scientific work performed in this area.

Scope

The progression of this work will flow from the specific, practical application of SIBS in orbital prosthesis application in Chapters 2 and 3, to a more general investigation of SIBS in Chapters 4-7. This sequence is used in order to firmly establish the motivation

behind the more fundamental research of the later chapters. It is of importance to highlight that throughout this document the term degradation is used for mechanical degradation and not chemical degradation.

In this work, a novel cost-effective, non-contact method that allows the use of any thermoplastic elastomer for the fabrication of orbital prosthesis via laser scanning and rapid prototyping is proposed and validated in Chapter 2. This method allows for the production of custom made prosthetics for patients locally, or overseas, with only one visit to a scanning center. Moreover, this method minimizes time required for a skilled operator to produce the digital prosthesis, cutting down on production cost and time. This method is the first to allow the use of thermoplastic elastomers for prosthetic applications, as it is based on injection molding rather than room temperature vulcanization.

Chapter 3 will focus on the development and testing of a fluid-immersed, electromagnetically driven, ocular piece for prosthetic applications. This piece includes an infrared camera for pupil detection and real-time mapping of the dynamic prosthesis. A thorough description of the device calibration and pupil detection algorithm is presented.

The focus of Chapter 4 is the plastic injection molding process. In this this chapter, a Taguchi orthogonal array design of experiment was utilized to determine the effect of different injection molding parameters on the ultimate tensile strength of a 30 weight percentage styrene SIBS block copolymer (denominated SIBSTAR 103T). Selected injection molding parameters were melt temperature (T), mold temperature (T_m), injection rate (Sp) and packing time (t). RSM and ANN techniques were applied in order to model and predict tensile strength. Predictions from both methods were compared to experimental results in order to validate the performance of these methods.

Chapter 5 proposes a new protocol for lipid uptake by gravimetric measurement. It also presents the absorption results based on the protocol and the associated model of diffusion based on SIBS polystyrene content and molecular weight. Diffusion kinetics of four different formulations of SIBS were studied by gravimetric measurements. The recovered diffusion parameters of three different formulations were analyzed and used to predict the behavior of the remaining SIBS formulation based on the molecular weight and composition. The goal is to provide a tool for engineers to estimate lipid diffusion parameters and to be able to predict long-term concentration of lipids in SIBS during in vivo use. Swelling of samples was also measured throughout the lipid immersion and a simple swelling model was used to model the change in thickness for the different types of SIBS used.

The scope of Chapter 6 is understanding lipid-induced plasticization in SIBS and the effects of composition on relaxation resistance. Extensive material characterization is performed in terms of mechanical and viscoelastic properties. Chemical interactions are also studied between the polymer and the intruding triglycerides. A new degradation mechanism is observed related to polymer plasticization. Pore formation prior to surface cracking is observed in samples with low molecular weight.

Finally, in Chapter 7 the relationship between lipid uptake and relaxation is experimentally investigated and a new method for determining the swelling coefficient via finite element method is introduced. A coupled multiphysics model based on the strain energy density function recovered from experimental observation, and the lipid transport properties is validated. The model is calibrated individually with diffusion and tensile strength data, to match experimental results. The swelling coefficient is selected by

matching the finite element model swelling to the measured swelling of diffusion samples. This method allows for determination of swelling coefficient due to the absorption of non-volatile fluids in polymeric materials that would not be possible otherwise. With the recovered parameters it is possible to determine long-term material performance in lipid-rich environments, and better design biomedical devices.

Chapter 2

A novel process to fabricate orbital prosthesis

This project was developed with the idea of producing prosthesis for low-income individuals that could not afford prosthesis made by skilled artists, so the equipment utilized here was selected based on availability, cost and performance. The laser scanner utilized was a 3D Scanner Ultra HD manufactured by NextEngine. The claimed dimensional accuracy on this scanner is ±0.127 mm (±0.005 inches). However, if the patient has complete computed tomography or magnetic resonance imaging data it is possible to use that data instead of going through the laser scanning process.

The patient was a middle-aged Caucasian woman, with a right orbital defect. The patient has a prosthesis made with a silicone elastomer by a skilled artist, which served as a comparison. The entire prosthesis fabrication methodology is described step-by-step as follows:

1- Scan the face of the patient using the 3D laser scanner system. This process is best done by having the patient sit down and placing their head on a chin rest. The patient needs to be relaxed with a neutral expression, in order to minimize moving during each scan. Scan from different angles, making sure that the entire orbital defect and contralateral periorbital regions are captured. Each scan takes about two minutes to be complete, so the entire process of scanning takes no more than 45 minutes per patient.

2- Once all the scans are complete, the raw data can be imported to any CAD software capable of handling polygon meshes. The software used in this work is Geomagic Design (3D Systems, South Carolina, USA). All scans have to be aligned using the

best fit alignment tool, which minimizes deviation between overlapping scans, in order to recreate a complete virtual anatomy of the patient. The result of such alignment is shown in Figure 4.

Figure 4- Digitalized anatomic topography of patient

3- The following step is to locate the facial symmetry plane to mirror the digitalized face. However, this step could be extremely time consuming depending on the quality of scan data available. To circumvent this problem an alternate approach is also proposed (see step 3b). In order to find a symmetry plane, the nasal region is extracted and used to fit a plane based on a symmetry search algorithm. The algorithm requires an approximate symmetry plane, which is selected using 3 or more intersections between the plane and the extracted region. This process could fail and the search might be started all over with a new initial plane, making it cumbersome and time-consuming. The resulting symmetry plane can be seen in

Figure 5, the gray colored topography corresponds to the mirrored nasal region. As it can be seen, there is very good symmetry for the scan data used here.

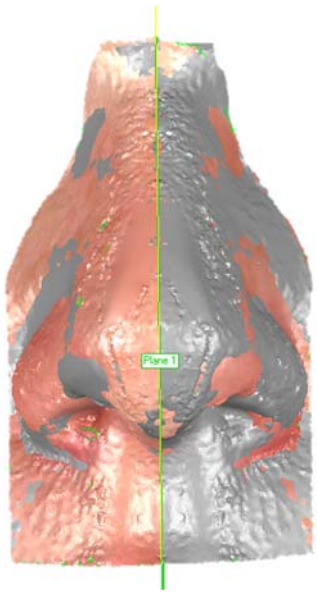

Figure 5-Symmetry plane detection based on nasal region

b. If the symmetry detection fails due to bad quality scan data, it is possible to create an arbitrary plane and mirror the scanned face through it. The mirrored face will not be precisely aligned with the original scan, so a best fit realignment can be performed as it was done before for the individual scans in step 2. The outcome is almost identical to the one described in step 3.

4- It is very important to determine where the original scan and the mirrored scan start deviating due to the orbital defect, in order to select the appropriate boundaries of the prosthesis. This can be done by performing a deviation analysis, which finds the minimum distance between a point in the original scan and a point in the mirror scan. The outcome of this is a colored map of the deviation between scans, which helps chose the correct boundary for the prosthesis as it points to the exact boundary

of the orbital defect. Figure 6 shows the deviation map of the patient scan data. Minimum deviation occurs between yellow and light blue boundary (see color scale bar). This shows how far the prosthesis has to extend to the cheek bone, temple, eyebrow and nasal bone

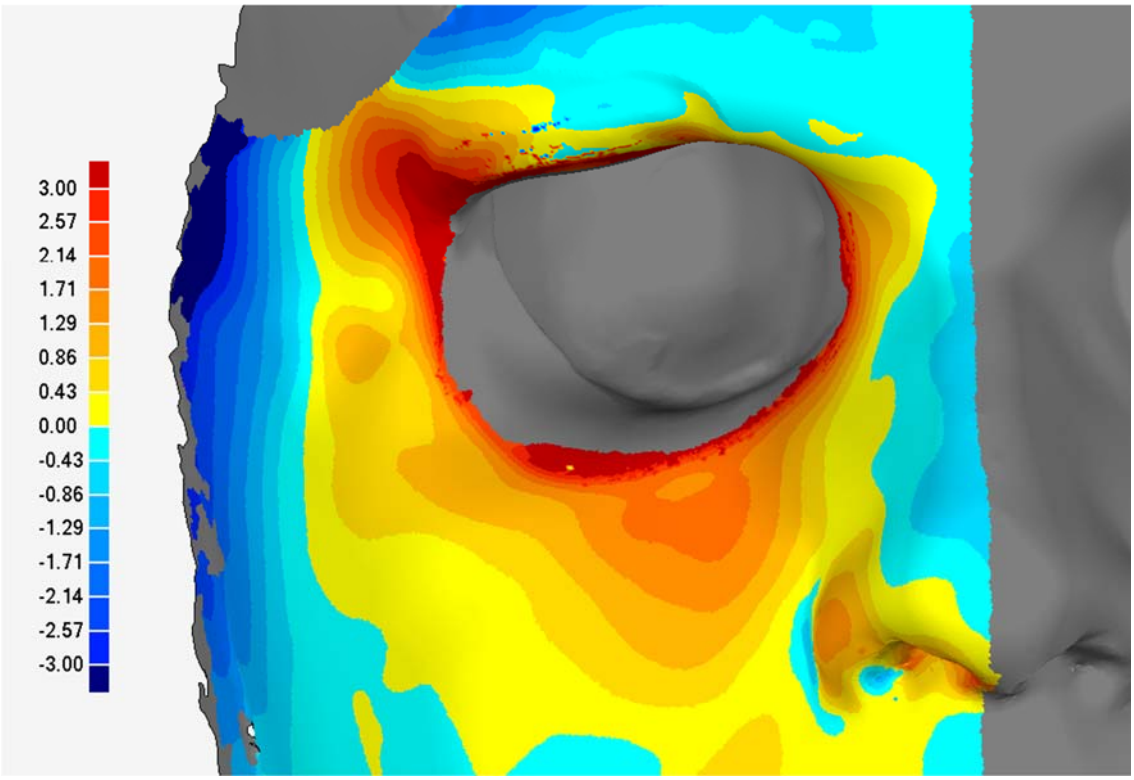

Figure 6-Deviation map surrounding orbital defect.

5- Once the boundary is selected, the data can be trimmed to produce the back and front of the prosthesis. The front part is composed of the mirrored scan and the back part is composed of the orbital defect. These surfaces are stitched together to create a watertight model of the prosthesis, which conforms to the entire orbital socket. As there is no need to cover the entire orbital socket, the back side is cut to half the depth of the defect and concaved to produce a standalone prosthesis that fits the patient without the need of bone implantation or using skin safe adhesive. A front and back view of the digital prosthesis is showed in Figure 7.

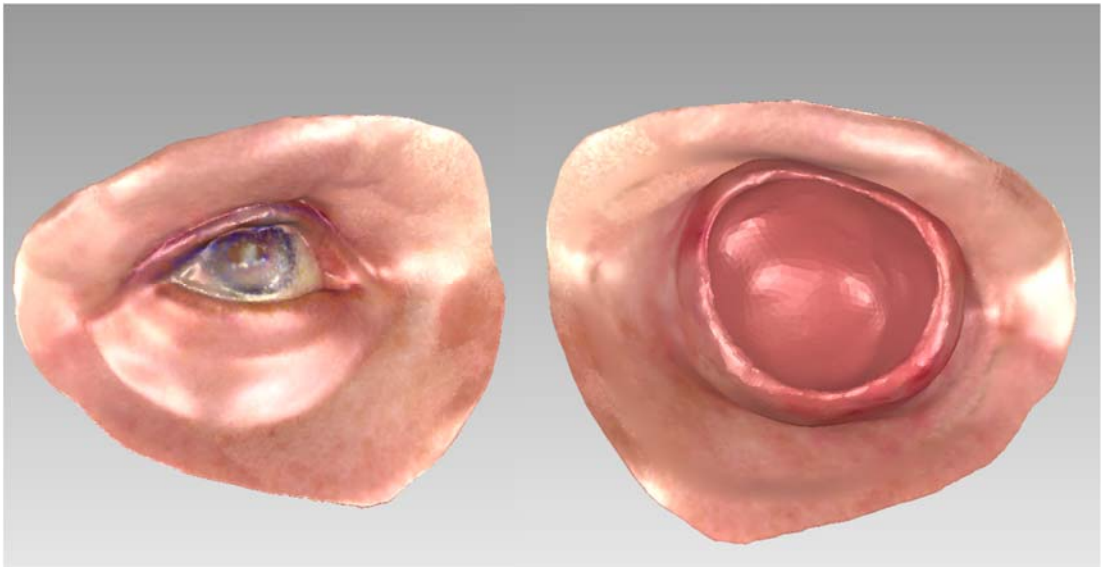

Figure 7-Digital prosthesis model. Front view and back view

6- At this point, it is possible to 3D print the prosthesis and use that to make a negative mold using conventional methods, but this does not allow to use thermoplastic elastomers. A proper injection mold has to be fabricated, either through the use of a master mold and an alumina reinforced high-temperature epoxy or by creating the injection mold virtually. To create the mold virtually, the front and back of the prosthesis are separated along the edge and used to build a two-piece mold with matching shapes. It is crucial that the parting line of the mold is along the prosthesis edge, which will hide the seam line caused in the contact of both mold parts. If this is not done, the seam line will show along the front of the prosthesis rendering the prosthesis unusable for the patient. Figure 8 shows the two-part 3D printed mold that can be used for injection molding the orbital prosthesis. Both the 3D printed mold and the high-temperature epoxy molds produce same quality prosthesis and both molds start breaking after a few number of uses (25 uses or more) due to the high temperature and pressure applied. However, the epoxy mold is preferred

because of its lower cost, and better resistance to breakdown; even though the time to fabricate is longer as the epoxy has to set (usually takes 24 hours).

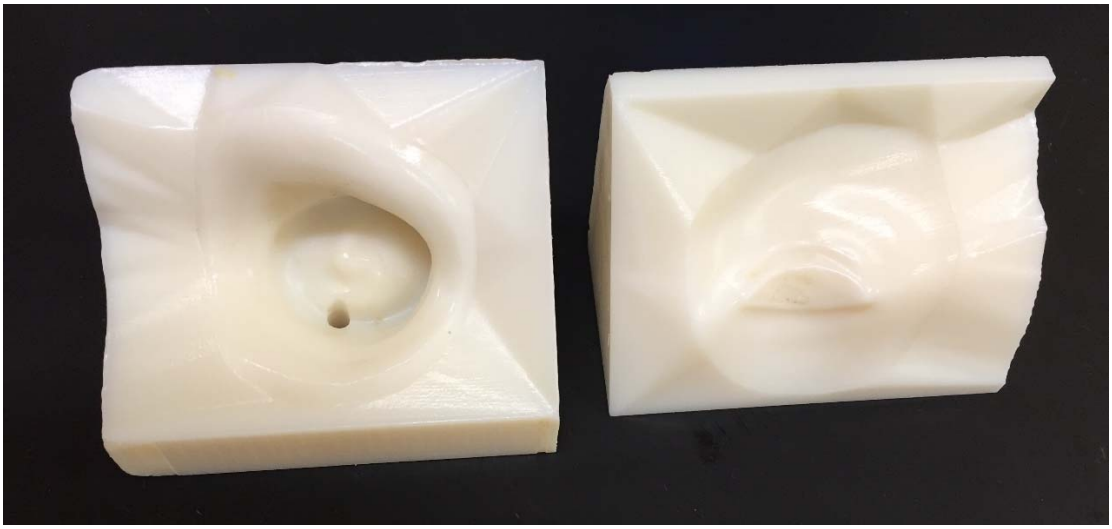

Figure 8-3D printed mold

A low styrene content, low molecular weight formulation of SIBS was selected to produce a prosthesis that feels soft and comfortable to the skin, and has the shine and gloss of human skin. A combination of silica, mica, nanoclay, pigments, and red flocking powder was extruded with SIBS prior to injection molding the prosthesis to achieve intrinsic coloration to match the base skin tone of the patient as closely as possible. This process was repeated until all coloration was homogeneous through SIBS, with no visible flow marks from mixing. The use of injection molding processing is not limited to SIBS, it allows for a vast number of different materials to be used for fabricating the orbital prosthesis, such as thermoplastic olefins, elastomeric alloys, polyurethanes, copolyesters, polyamides, or other styrenic block copolymers among many others.

A mold insert in the shape of a slightly oversized ocular prosthesis was attached to the injection mold to produce the negative cavity for the ocular piece. Once the mold and the skin tone extrusion are complete, skin colored SIBS is injected to the mold to form the

prosthesis. If placement of the ocular insert is not satisfactory, the insert can be removed and repositioned to fabricate an orbital prosthesis with a forward looking expression.

The prosthesis should be allowed to cool down before removing from the mold. Once removed, an ocular piece can be placed in position and fixed with a small amount of cyanoacrylate. Artificial eyelashes are added to the prosthesis and some extrinsic coloration can be added to account for skin tone variations and to better match the skin tone of the patient around the edges of the prosthesis.

Prosthesis results

The entire fabrication process took an hour to scan the patient, 4 hours to digitally reconstruct the prosthesis, 24 hours to cast the high temperature injection mold, 1 hour to mix the intrinsic pigments in SIBS and inject the prosthesis, and 1 hour to post-process the orbital prosthesis. The final product resulted in a perfect fit on the patient without the need of repeating the process. Figure 9 shows a picture of the patient wearing the prosthesis with glasses. Patients that have orbital prostheses usually wear glasses to protect the contralateral periorbital region and to hide the edges of the prosthesis giving more realistic looks. As it can be seen from the picture, the prosthesis shape conforms perfectly to the face of the patient and looks perfectly symmetric to the contralateral orbital region.

Figure 10 shows a comparison of prosthesis fabricated by conventional methods and the prosthesis fabricated via the proposed method. The top picture is the prosthetist-made prosthesis using traditional methods and the bottom picture is fabricated following the method presented here. The prosthesis fabricated with our novel method shows a much better symmetry compared to the hand-made prosthesis because the scanner is able to pick up many small details that are extremely hard to replicate by hand.

Figure 9-Patient wearing custom-made, injection molded orbital prosthesis

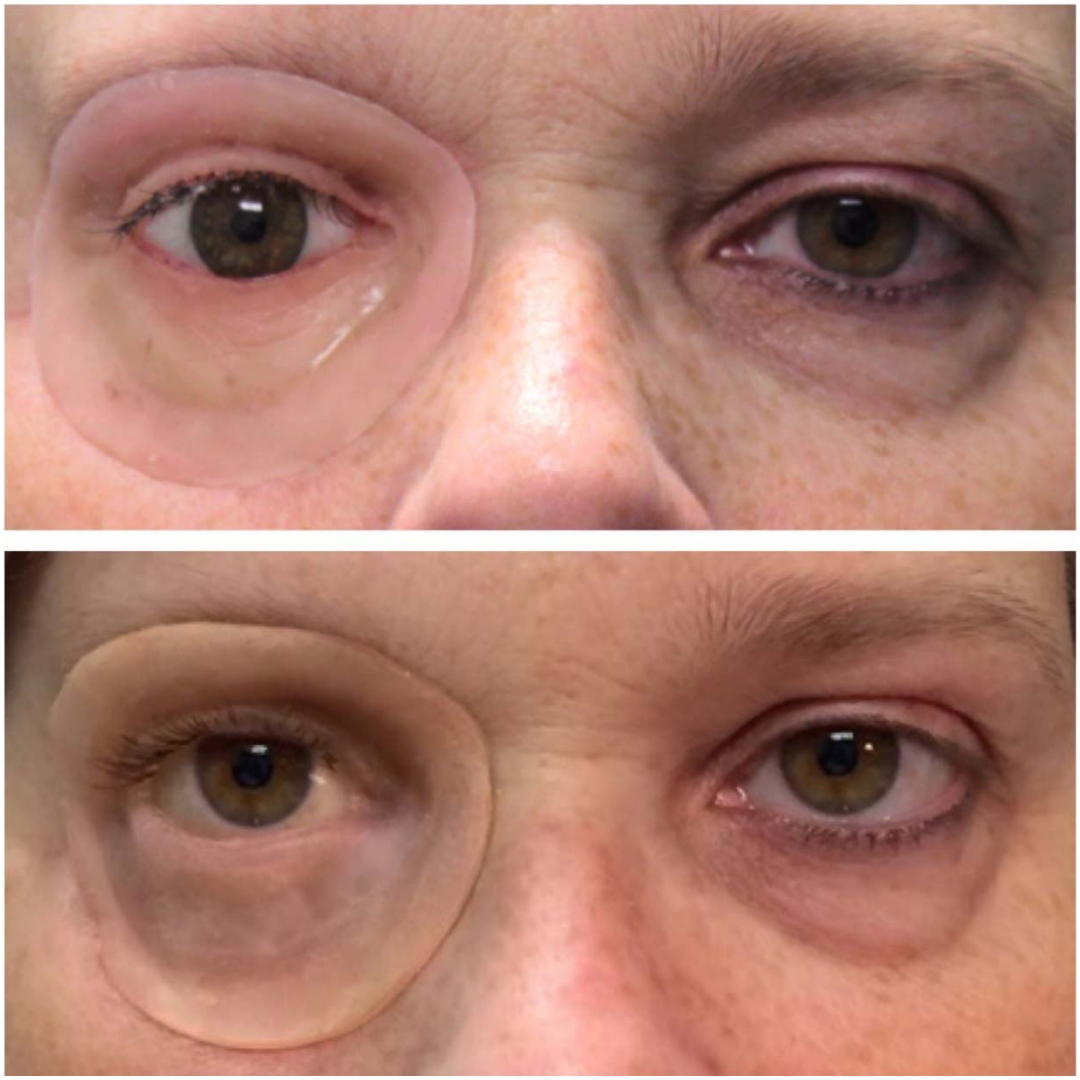

Figure 10-Comparison of prosthesis

Discussion

The patient described our prosthesis as a much more comfortable fit than the prosthesis made by the prosthetist. Moreover, the patient also commented that the SIBS prosthesis felt much better to the touch, making it more comfortable than her prosthesis. This was based on the first impression of the prosthesis. Long-term use of the prosthesis (8-12 hours) could be different, and may vary from patient to patient. The front face of the prosthesis also represented the face of the patient to a much better degree, due to the virtual mirroring operation, making the prosthesis look more natural for the patient. The potential of this work is the possibility to use any sort of thermoplastic elastomer, instead of being limited to room temperature vulcanizing silicone rubbers. The improved fatigue properties of thermoplastic elastomer like SIBS compared to medical grade silicones are well documented in the literature [14], these improved mechanical properties will address the short life spans that orbital prosthesis have today [2, 3, 6]. Furthermore, discoloration can also be addressed as new materials with better resistance to ultraviolet light are used to manufacture prosthesis. It is very important to point out that it is possible to repair thermoplastic prostheses, as it allows for refusing tears and sealing cracks with the application of heat. Lastly, this method gives the possibility to produce prosthesis for patients that are not present locally, as the digitalized scan data can be received and the prosthesis manufactured without the need of the patient being present during the digital reconstruction, 3D printing or injection molding phase. This allows for patients that do not have access to a prosthetist to be able to access custom-made orbital prosthesis, at fractions of the cost of what orbital prosthesis cost today.

It is important to mention that is extremely beneficial to have a color palette matching different skin tones for different materials. This is readily commercially available for some silicone rubbers, but it is not available for thermoplastic elastomers. Prosthesis fabricated for an African American patient required a completely different approach to the additive and flocking selection. Figure 11 shows the different skin tone prosthesis. Much time and resources would be saved with a proper skin tone palette.

Figure 11-Prosthesis for an African American patient

Chapter 3

Background on ocular pieces

Orbital prostheses are the only rehabilitating device that cancer or trauma patients can use post-exenterations. These devices are purely aesthetical in nature and do not have functionalities to restore vision to the patient. A major flaw in current orbital prosthesis technology is the lack of movement of the ocular piece, blinking capabilities and the ability to produce tears during moments of extreme emotion. There are a large number of constraints attached to these devices that present a great number of challenges to produce a functional prosthesis. For example, the prosthesis needs to be able to last for millions of cycles without wearing or deteriorating. Assuming a person performs on average 15 eye movements per minute, that translates to almost 7.9 million movements per year. And due to the nature of prosthetic devices, these have to be designed to last for many years. Because of the wear that this would produce on mechanical parts, the prosthesis has to be designed using a minimum number of moving components. Another constrain on the ocular piece is the level of vibration and noise it produces during operation. Due to the location of the prosthesis in the patient's body, vibration and noise is not tolerated. Even the smallest of the vibrations or noises could lead to headaches or uncomfortable feeling for the user, making the patient go back to using static prosthesis or a patch. Moreover, the device must have an ultra-low response time to be able to properly match the movement of the human eye. Even the faintest of lags would result in attention being focused on the prosthesis, bringing people to notice the prosthesis and interrupting social interactions with the user. Furthermore, the device must be able to reach the high acceleration and movement speed

of the human eye. In a human saccade speed study, it was shown that peak velocity was dependent on saccade amplitude. Longer trajectories reached higher peak velocities than shorter trajectories. A maximum peak velocity of up to 600 degrees/second was observed for eye rotations of 90 degrees in amplitude, and durations of 280 milliseconds. Rotations of 30 degrees showed a velocity of 400 degrees/second, and a duration of almost 120 milliseconds [78]. Although not constant, the speed goes through a smooth acceleration and deceleration as measured in multiple studies [78, 79]. The dynamic ocular piece must be able to match these acceleration and deceleration rates to mimic the human eye effectively. Another constraint of the dynamic prosthesis is the minimal power dissipation it requires. The device cannot heat itself up by dissipating power, because that could burn the user of the prosthesis. Hence, it is necessary for the design to have a neutral equilibrium that can be achieved with no power dissipation. This neutral state would also save battery for the device to last for long periods of time before having to be recharged. Moreover, the ocular piece has to look and move organically mimicking the human eye. If the prosthesis does not look natural, any person interacting with the patient will notice the prosthesis. This also means the controller has to be able to replicate the quick motions of the human saccade, and the smooth motion of the eye while tracking an object. All the mentioned constraints have to be enclosed in a device that has a diameter of approximately 1.2 inches, which is the average volume of orbital socket after an exenterations has been performed.

Due to the aforementioned constraints, the selected method of actuation was electromagnetic. This method presents the minimum number of moving parts, minimum vibration, allows for a stable neutral equilibrium, and allows for fluid-immersion to improve the organic look of the device. Other methods investigated include servo actuator,

piezoelectric actuation and digital display. Servo motors are not small enough to be able to fit properly in the required space, and they generate large vibrations and sounds due to the number of mechanical parts. Moreover, plastic servo motors are not rated for the large number of operating cycles required for this device. Piezoelectric actuation was not able to reach the required speeds for the ocular piece to match human eye speeds, although the smaller size was suitable for this application. Lastly, digital displays were not selected as an option because the lack of over the counter, flexible displays with high resolution definition. A digital display would also encounter problems while operating in dark environments, making the prosthesis bright and stand out.

Development of a dynamic ocular piece

The basic operating principle of the dynamic ocular piece is the same principle that governs permanent magnet stepper motors. In this type of motors, a magnet wire is coiled around a dielectric material to create a magnetic field capable of displacing the rotor. The rotor is made with permanent magnets that will rotate and align with the stator magnetic field. By running a current through the coils in the stator stage, the rotor performs a "step" and aligns to the magnetic field. The dynamic ocular piece was designed with this concept in mind to be able to produce the necessary rotation of the prosthetic eye. Many designs were evaluated and tested prior to finalizing the magnet/coil configuration. The preferred configuration located the magnet and coil array on the posterior side of the device, however this design lacked the sufficient force moment to rotate the eye to a downward gaze. The most efficient prototype had the magnets and coils located close to the poles of the sphere. This configuration also allowed for a weak restoring magnet that enables a neutral gaze expending no energy. A CAD model render of the device is shown in the following figures.

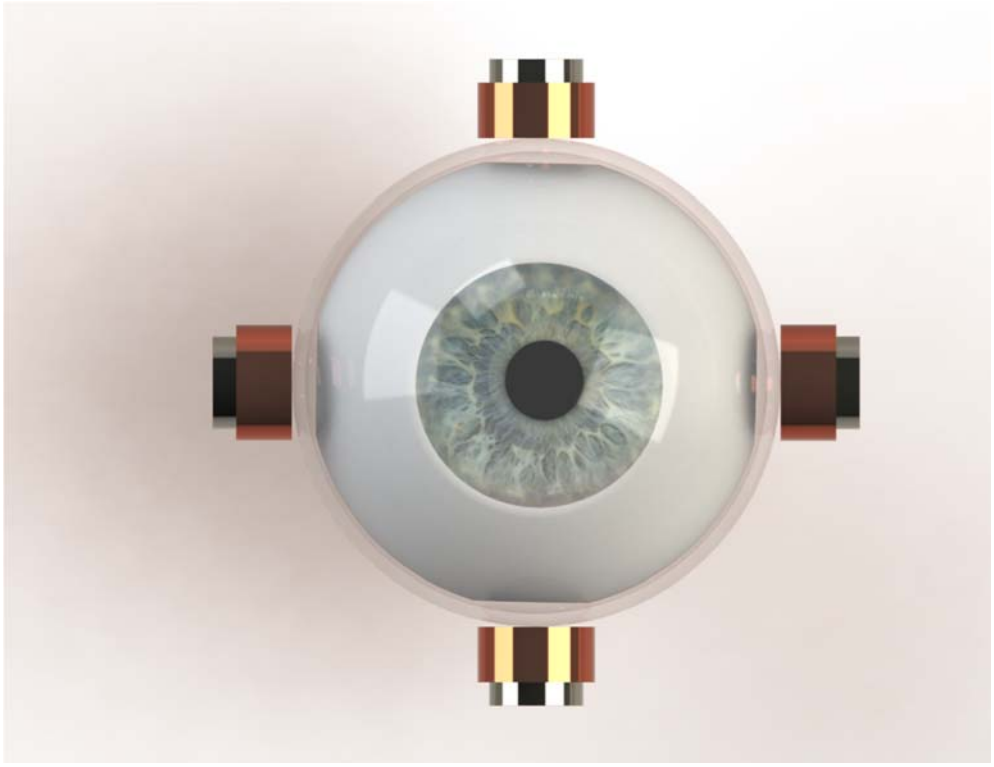

Figure 12-Front view of CAD render

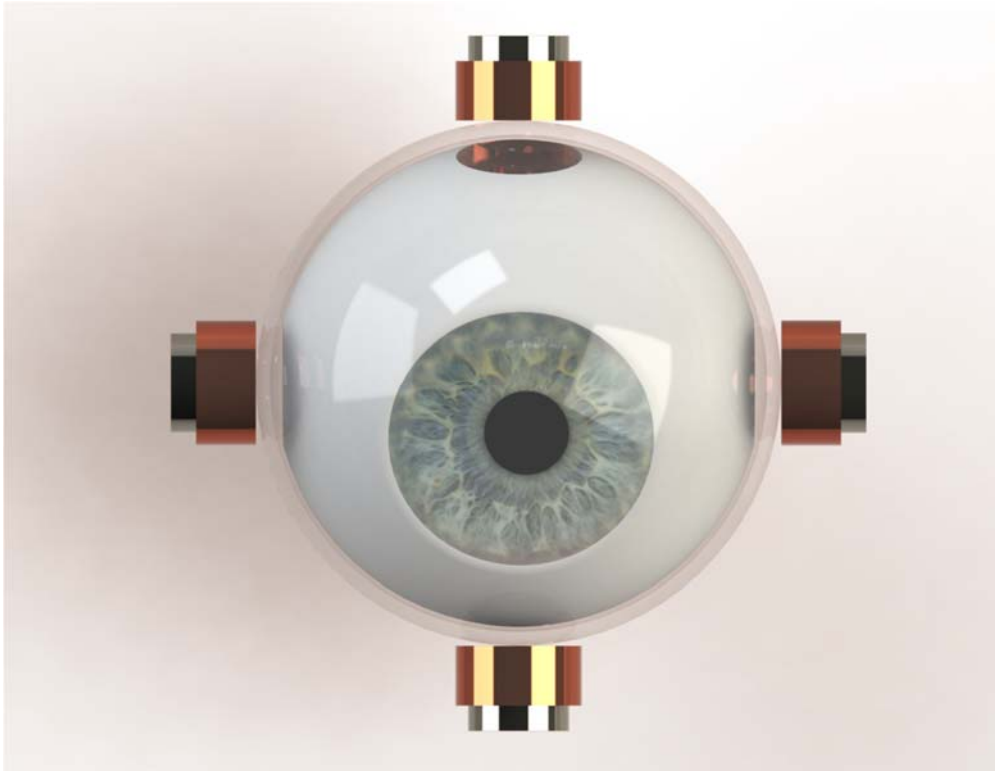

Figure 13- Ocular piece looking downwards

Figure 14-Isometric view of dynamic eye piece

An off-white acetyl sphere of approximately 25 mm in diameter was chamfered to produce a flat surface of dimension similar to the human iris (13 mm in diameter). A high definition digital photography image of a human iris was bonded to the chamfered area of the sphere. Holes with 6.4 mm diameter were drilled to make space for rare-earth neodymium magnets in the north, south, east and west pole of the sphere. Neodymium magnets were inserted to their respective holes until flush with the acetyl sphere and secured in place with cyanoacrylate. Molds to fabricate a custom acrylic shell were designed via CAD and printed using a Form1+ stereo lithography type 3D printer. The hemispherical shells were made slightly bigger than the acetyl sphere, with a thickness under 1 mm. A two-part

optically clear acrylic resin was used to cast the shells. To ensure that no bubbles were entrapped during the casting process, a pressure pot was used for curing under 60 psi of pressure. Enameled magnet wire was coiled around plastic bobbin formers, to ensure symmetry of coils. The resulting coils had a resistance of 10 Ω, and where positioned on the exterior of the acrylic shell with a slight offset to the front and back of the prosthesis (as depicted by Figure 13). A weak restoring magnet was placed between wire coils, in order to restore the gaze to a neutral position. This allows for battery saving, as no current is needed to keep a front gaze position. The dynamic ocular piece was injected with water in order to fill the gap between the acetyl eyeball and the acrylic shell. This also gives the eyeball a very realistic organic looking effect. The following set of images show the final prototype. The prosthesis is contained in a plastic casing solely to protect the coils and outside magnets.

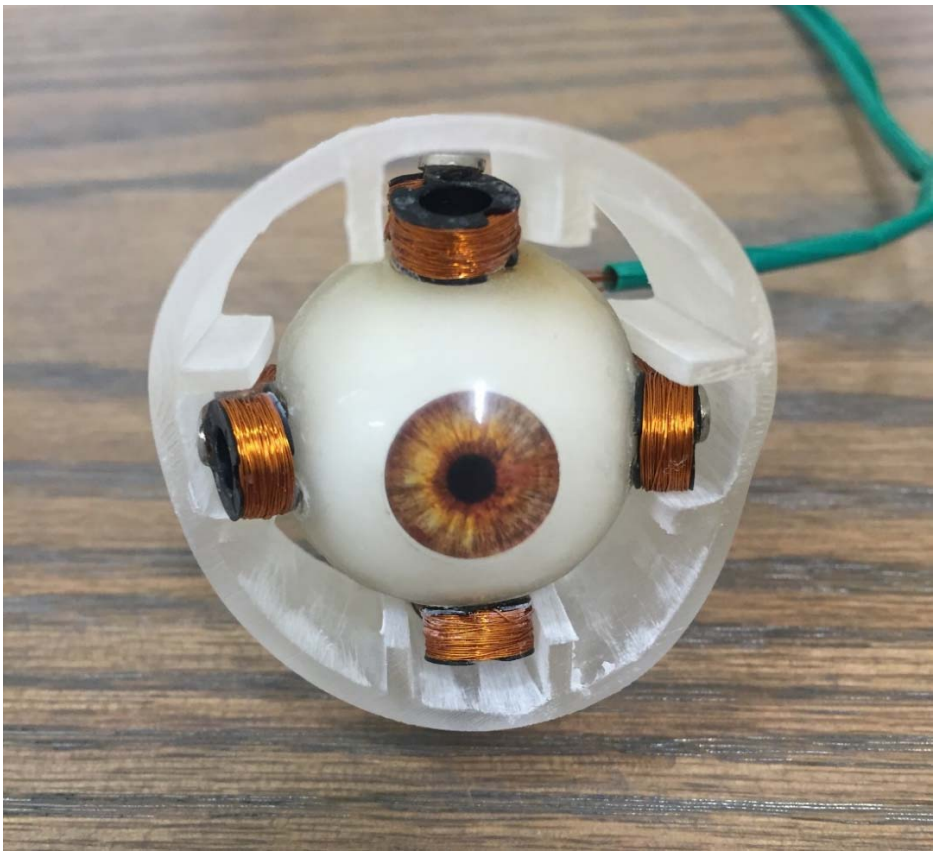

Figure 15- Dynamic ocular piece prototype front view

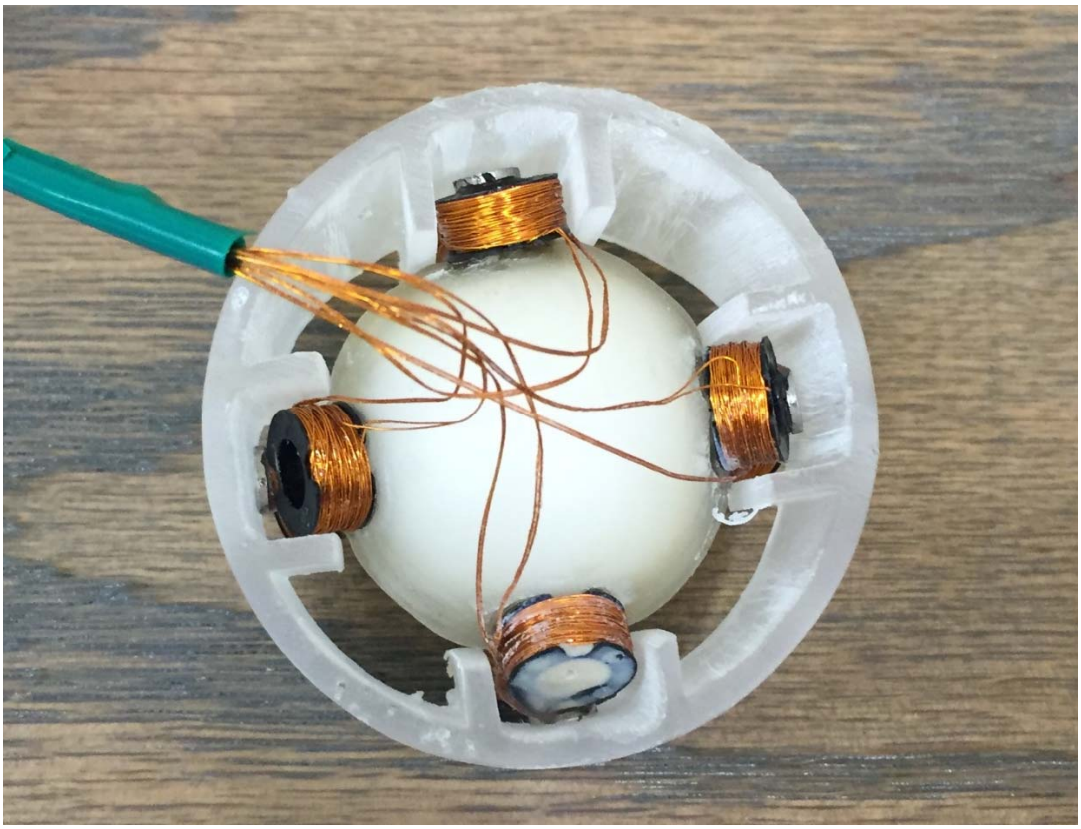

Figure 16-Dynamic ocular piece back view

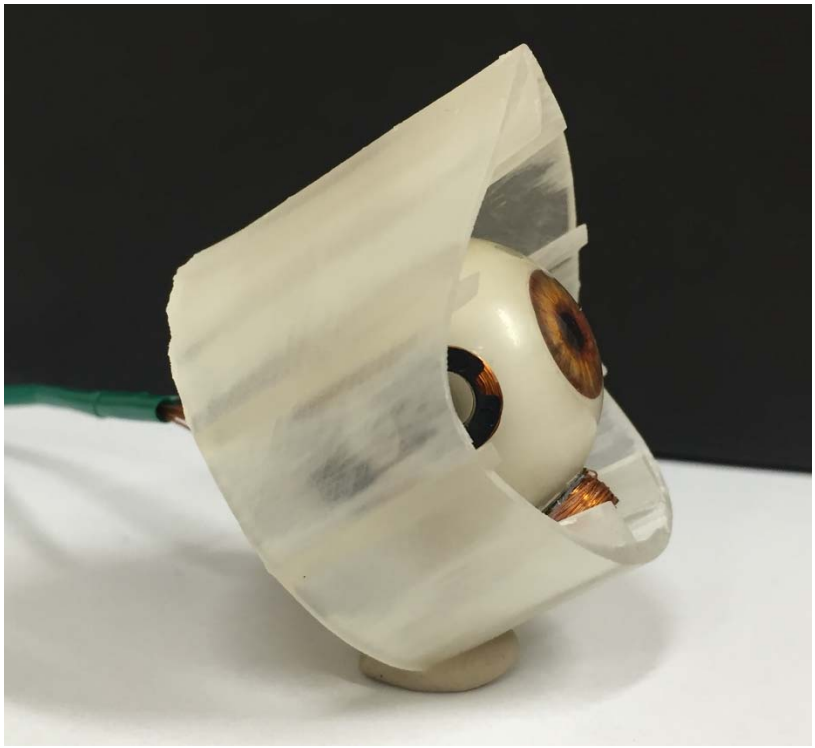

Figure 17-Dynamic ocular piece side view

Figure 18-Dynamic ocular piece with SIBS prosthesis cover

Embedded controller system and calibration

The dynamic ocular piece works by simply applying a DC power supply through the coils. Through electromagnetic induction, the current in the coils generate a magnetic field. By applying an attractive and opposing electromagnetic field in each pole, the eyeball will rotate and adjust its position matching the induced field from the coils. This effect can be performed for both pan and tilt of the dynamic ocular piece. Figure 19 and Figure 20 show the magnetic field arrangement for a simple rotation. As it can be seen from the standby condition, the outer magnet restores the ocular piece to its equilibrium position without powering the coils.

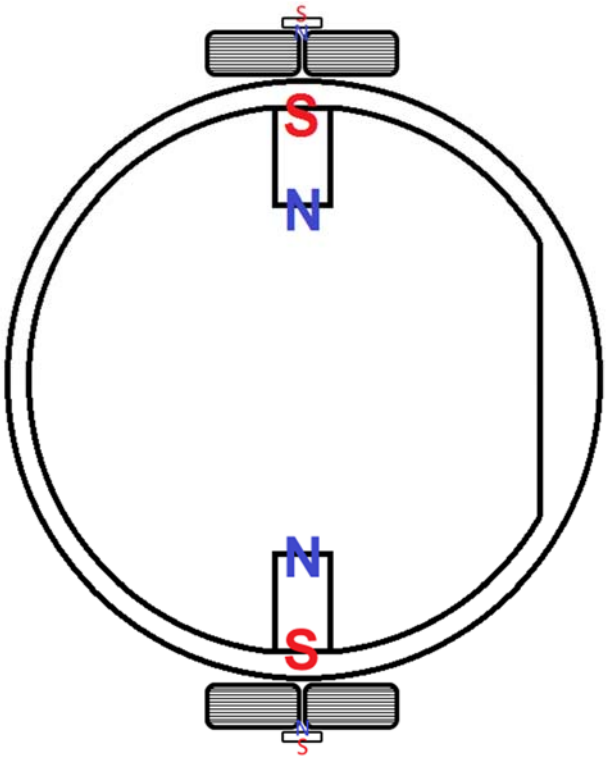

Figure 19-Schematic of ocular piece in neutral condition

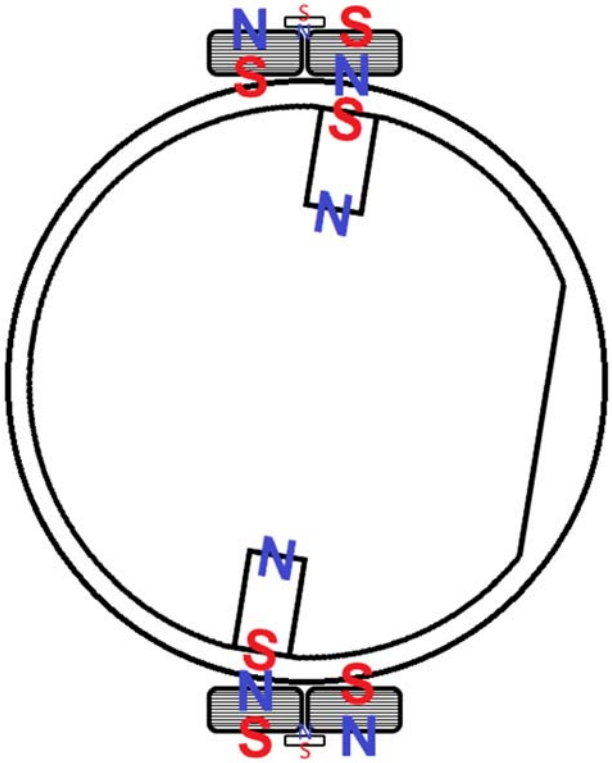

Figure 20-Schematic of ocular piece in rotated condition

To ensure proper motion of the device, angular rotations were measured against different voltage levels. Calibration curves were plotted to map the displacement of the ocular piece and to examine repeatability of motion. A calibration fixture was designed in order to perform all measurements. A camera mounted on a tripod was used for fixed-frame imaging of the prosthesis. A DC power supply was used to regulate voltage of the prosthesis, and multiple images were taken at voltage levels ranging from 1 volts to 7.5 volts in 0.5 volt increments. Each image was analyzed using ImageJ in order to locate the centroid of the pupil and to determine the rotation of the prosthesis. 10 centroid locations were performed per image in order to properly determine the pupil location. The displacement from the neutral gaze position (0 voltage applied) was calculated and converted to angular rotation based on a micrometer scale that was placed next to the device. The resulting calibration curve is shown in Figure 21.

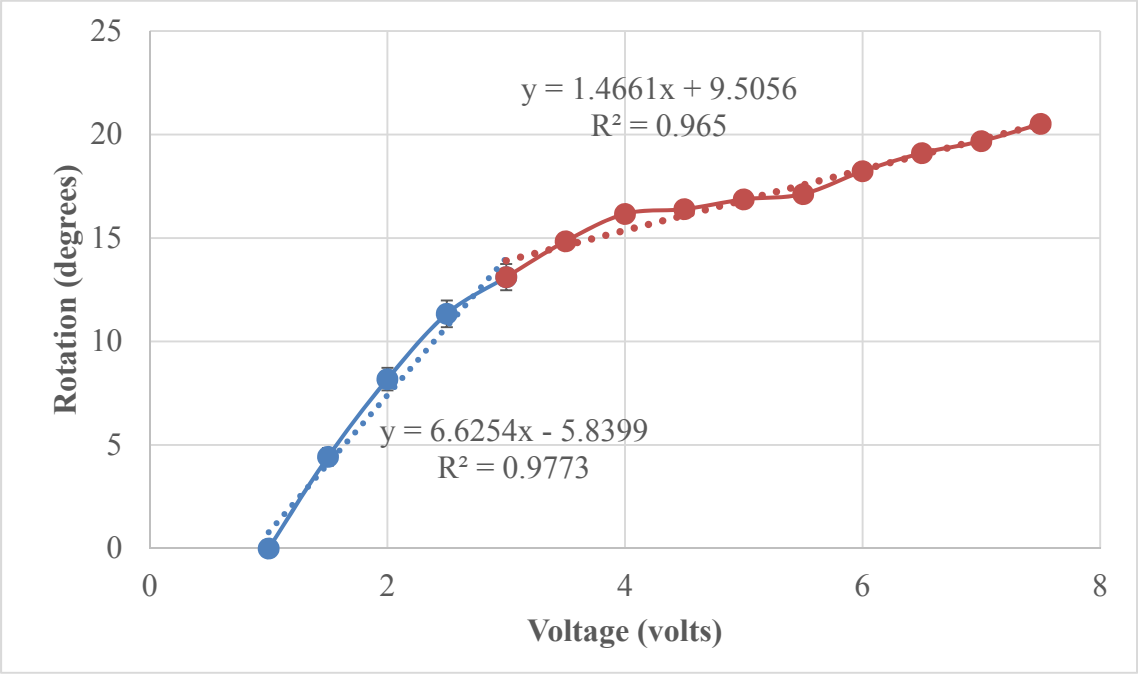

Figure 21-Calibration curve for dynamic ocular piece

As it can be seen from the figure, there are two different linear regions of the ocular piece. The initial region starts at a voltage value of 1 volt due to the restoring magnet. Below that threshold level, the electromagnets are not powerful enough to rotate the eyeball inside. Once the rotation reaches approximately 14°, the slope of the curve changes. This is due to the nature of the magnetic field generated by the coils. The magnetic field is highly concentrated on the inside of the coil and does not spread outwards, so the repelling force decreases substantially the moment the pole magnet is out of line with the center of the coil. As more voltage is applied past that point, the increase in repelling force becomes negligible, leading to smaller rotation steps per extra volt applied.

The controller system for the dynamic ocular piece was built using an Arduino microcontroller and DC motor controllers. Through the Arduino, each motor controller can be precisely controlled using a pulse-width modulation (PWM) signal, and the current direction can be inverted to attract or repel the pole magnets. This allows for coils located in opposite poles to be used simultaneously for the accurate control of the device. Moreover, the Arduino is capable of performing serial communication with any image processing software, allowing to receive any type of input for mapping the prosthesis. The controller requires two different power supplies, a battery system to operate the coils, and another battery supply to power the Arduino board. Figure 22 shows a picture of the setup connections. The USB connection on the Arduino microcontroller (bottom left cable) communicates with the MATLAB image processing algorithm, while the DC motor controllers connect directly to the coils (right side cables). The microcontroller used here is just for prototype purposes, and is not representative of the volume the controller would require.

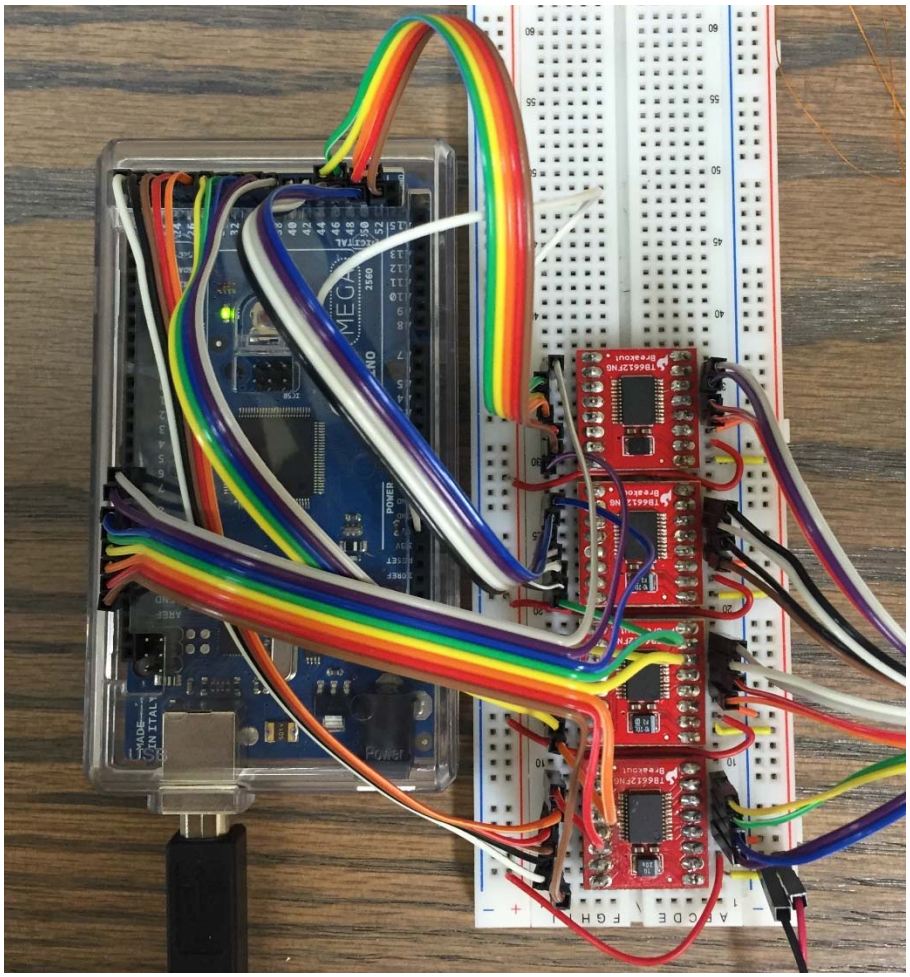

Figure 22-Microcontroller setup

Multiple rotations were performed at maximum speed to measure the dynamic response of rotation. This was necessary to ensure the device would have a dynamic response that matches the motion of the human eye. A fixed-frame video of the prosthesis performing maximum rotations was recorded and analyzed frame-by-frame to measure the rotational capacity. Table 1 shows the measured response of the prosthesis.

Table 1. Measured response

Frame Rate	30 fps
Frames	132 frames
Seconds	4.4 seconds
Pans	12
Degrees	40 deg
Angular velocity	481 deg/sec

The average angular velocity of the ocular piece was measured at 481 degrees per second. According to a quantitative study on saccade amplitude, duration and velocity the peak velocity of the human eye is 600 degrees per second. However this velocity is rated as peak velocity and requires long acceleration and deceleration times. The resulting average speed for healthy human subjects was 370 degrees per second [78]. Another study that investigated the effect of frequency of saccade on peak velocity measured average velocities of the human eye at approximately 270 degrees per second [79]. The dynamic ocular piece was able to outperform the human eye, showing sufficient average speed to move in real-time with the human eye.

Infrared Camera System for Pupil-Detection

A commercial webcam was modified for pupil-tracking, by replacing the light filter. The camera was originally equipped with a low-pass filter that blocks infrared light from the CMOS sensor. A high-pass filter was installed in order to filter visible light from the sensor and only transmit infrared light through. Infrared light is typically used for pupil-detection because of the differential lighting scheme. There is a high contrast between the pupil and all other facial features under infrared light. Also, if the infrared source is off-axis with respect to the focal axis of the camera, the pupil will appear dark [80]. This condition improves the pupil detection robustness, and allows the use of algorithms that are computationally less expensive and can compute a larger number of frames per second. It is important to point out that this technology is readily available in the market and is used in many marketing applications as well as ophthalmological applications. It has also been miniaturized to the point that no obstruction of the vision occurs, allowing patients to continue their daily lives freely. A commercial model manufactured by SMI, can track both

human pupils with sampling rates of up to 120 Hz. This sampling rate is more than sufficient for smooth operation of the dynamic ocular piece.

The custom-made pupil tracking system was built on commercial glasses. The installed lenses were removed for testing purposes because no eyesight correction was necessary for the test subject. A support was designed to extend the camera 10 cm away from the users face and towards the periphery of vision to reduce any obstruction. The final assembly is shown in Figure 23.

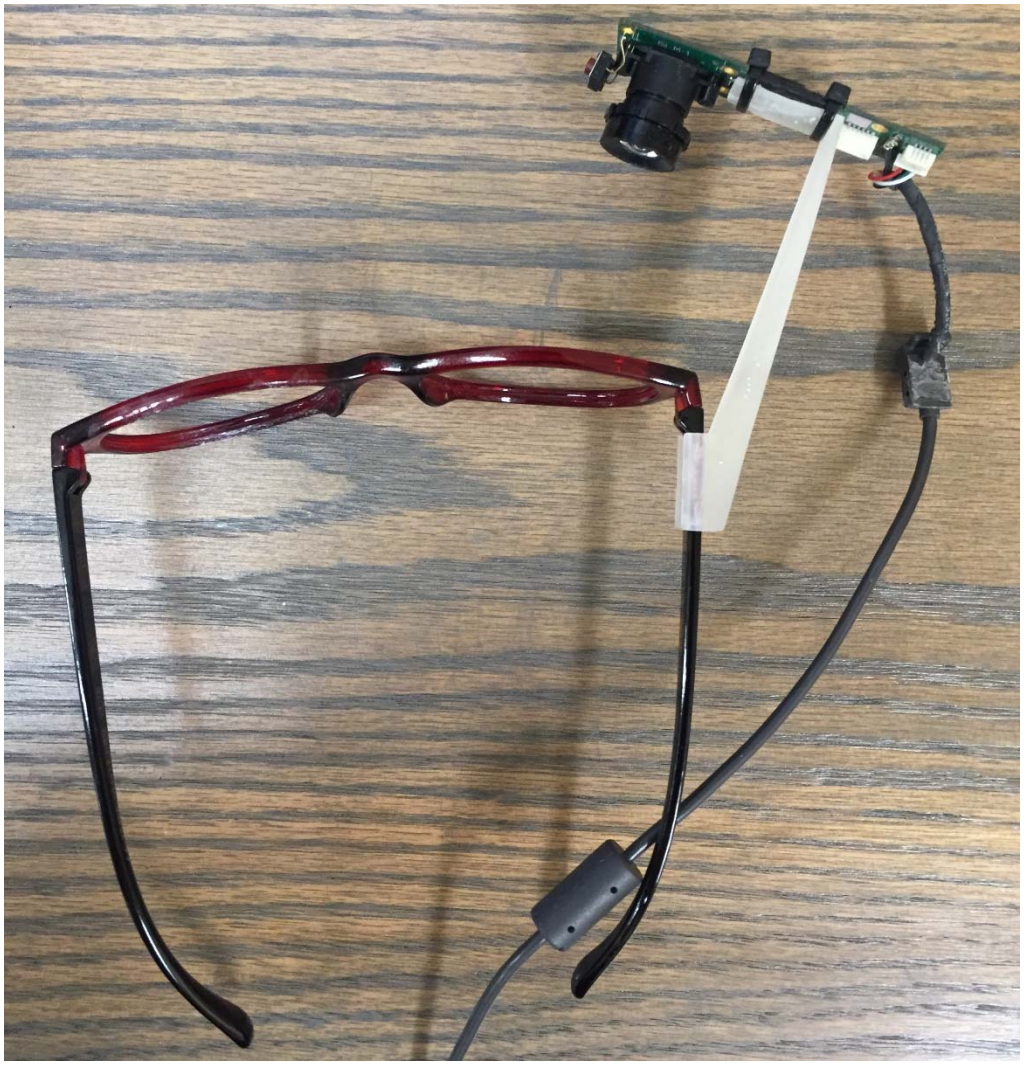

Figure 23-Glasses with mounted camera

Pupil detection algorithm

The pupil detection algorithm was as follows: frame capture, image cropping, grayscale transformation, Gaussian filter, histogram equalization, binary thresholding, first moment calculation and mapping. Below is a description of each individual step.

The first step was to capture a frame from the camera for analysis. This was performed using RGB scale and a 640x480 pixel resolution. The chosen low resolution allows for frame rates of up to 14 frames per second. This is the bottleneck of the process and it limits the performance of the prosthesis. Once the image was acquired and stored in memory, it was cropped to remove all unnecessary information. The camera is fixed relative to the patient's face, so the image size can be reduced to the limits of the eye. This process reduces computational cost and background noise for all subsequent operations. A calibration operation was performed by trial and error to find the proper cropping limits for the image.

The reduced picture was transformed to a gray scale. This is a pixel representation with a value from 0 to 1. As discussed earlier, the pupil produces a noticeably black signature under off-axis infrared light and has a high contrast with the white sclera of the eye. Figure 24 shows the grayscale image captured by the camera. The red and white circle indicates the location of the pupil.

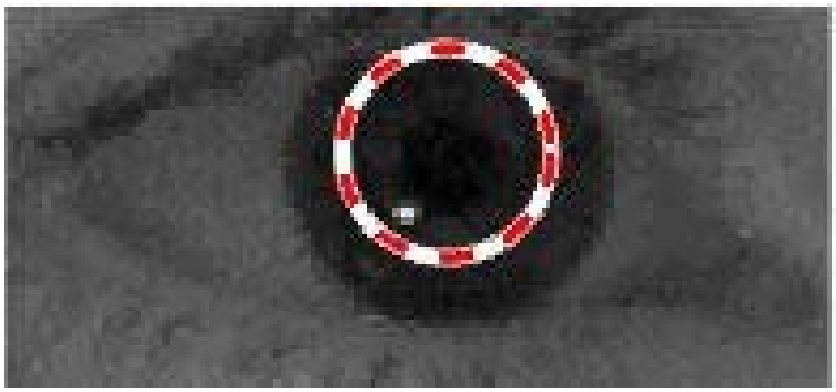

Figure 24-Grayscale Image of eye

A Gaussian filter is applied to the image to blur the eyelashes from the picture. Eyelashes were found to create noise in subsequent steps of the algorithm. Gaussian filtering averages out values to reduce contrast between high and low values. This process applied to eyelashes, that are extremely thin, effectively erases them from the detection range. The pupil is unaffected because of its large area. This is a very effective tool to clean up images before performing the thresholding operation.

The following step is histogram equalization. This is a normalization of the light intensity throughout the picture. This adjustment is necessary for extremely bright or dark environments, where contrast between features is limited. Without this step, the correct threshold value would be dynamic and changing based on the environment.

Once the image has been completely cleaned up for detection, the binary thresholding can be computed. During this operation all values below a certain value are replaced by zero, and all values above are replaced by one. The result of this operation is a white image with a black dot that represents the pupil of the eye. Figure 25 shows the resulting image after thresholding. This is the result from applying the algorithm to Figure 24.

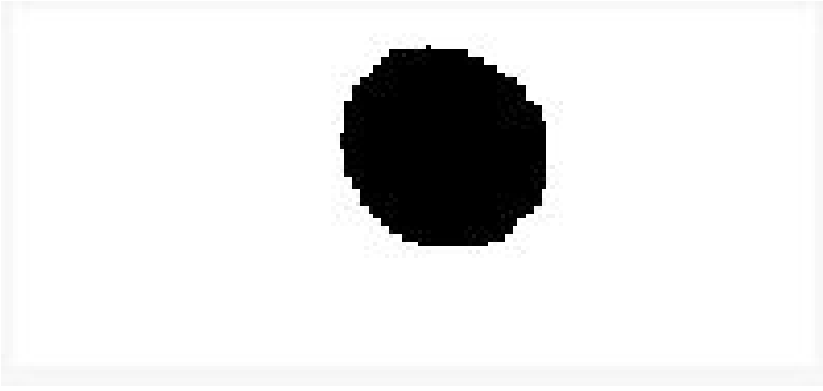

Figure 25-Pupil threshold image

The remaining last steps are performing a row and column count toe calculate the first moment of area. The first moment of area is the centroid location of the pupil with respect to the frame. This information is used to map the prosthesis with the gaze direction, and can be communicated via serial communication to the Arduino controller.

This algorithm is also able to detect blinks of the eye. When the eyelid is closing, the area and aspect ratio of the threshold image decreases. This value can be compared to a calibrated value to determine if the person is blinking or the eye is closed. When the algorithm detected the eye was closed, the prosthesis was mapped to a neutral gaze position for battery saving.

Discussion and Conclusion

The dynamic ocular piece was able to successfully match the human eye movement while testing. The movement of the device was extremely organic and showed potential for use in prosthetic applications, as well as animatronic applications. By utilizing a different embedded system, such as a Gumstix, it would be possible to perform all operations on the same controller board instead of a computer. Another improvement could be performed by coiling four electromagnets with the same wire. This exploitation of symmetry reduces the number of DC motor controllers necessary to just one, and number of output pins required two four.

Further steps required in order to improve the device performance includes selecting a smaller sized camera, to reduce any peripheral vision obstruction. There are cameras that are capable of much higher sampling rate increasing the response of the device. Lastly, the coil strength could be increased and positioned further back to allow for more rotation of the prosthesis to match the complete human eyeball rotation. The device successfully

proved the concept of using a fluid-immersed, electromagnetically driven eyeball for prosthetic and animatronic applications. There are still challenges that need to be addressed such as blinking and tears, however with the current size of the device no feasible method for blinking would be easily applied.

Chapter 4

Experimental set-up

KANEKA Corporation generously provided pellets of a 30% styrene content SIBS with a molecular weight of 105,000 g/mol (commercial name of SIBSTAR 103T). Pellets were processed with a specialized bench top injection molding setup. Dumbbell specimens were fabricated using a mold compliant with ASTM Standard D638 Type V. The injection molder was equipped with a linear actuator and speed controller in order to precisely control the injection speed. For each of the different parameter settings, the first SIBS specimens injected were discarded in order to ensure process stability. Subsequently, a group of eight samples were fabricated and tested in order to reduce measurement variation. All process parameters outside those being optimized remained fixed throughout the experiment. Cooling time was held constant at two minutes at room temperature prior to demolding. The custom injection molding system was designed specifically for precise control of injection rate in lieu of active control or passive measurement of packing pressure. As such, packing pressure was excluded from the optimization process. For commercial systems capable of precise control of packing pressure, this additional variable (or any other) can easily be incorporated into the method outlined here, with the potential for even greater improvement in tensile strength. Dumbbell specimens were tested using an Instron 5966 Tensile Testing Machine at a constant rate of 500 mm/min until failure of the sample.

Taguchi Method

The Taguchi method is a widely used engineering technique to analyze and optimize processes. This method utilizes orthogonal arrays in order to quantify individual effects of parameters and predict experimental outcomes without running full-factorial experimental domains. To accomplish this, it utilizes a specific Signal to Noise ratio (S/N) to characterize product quality. The S/N ratio is determined based on the goal of the experiment. It can be divided into three different types: larger is better, nominal is best, and smaller is better. The relevant equations are as follows:

$$\frac{S}{N} = -10 \log_{10}\left[\frac{1}{n}\sum_{i=1}^{n}\frac{1}{y_i^2}\right] \text{ Larger is better} \tag{3}$$

$$\frac{S}{N} = 10 \log_{10}\left[\frac{\overline{y_i^2}}{\sigma^2}\right] \text{ Nominal is best} \tag{4}$$

$$\frac{S}{N} = -10 \log_{10}\left[\frac{1}{n}\sum_{i=1}^{n} y_i^2\right] \text{Smaller is better} \tag{5}$$

Where y_i is the observed response of the i^{th} measurement, n is the number of measurements, σ is the standard deviation of the observed response and $\bar{y}$ is the mean of the response. One drawback of this method is that it does not work with continuous factors, so it is used in experimental setups where factors are categorical or to reduce experimental complexity. In this study, the selected S/N ratio was *Larger is Better* based on the goal of maximizing tensile strength, and an L_9 orthogonal array was used to analyze the four variables at three distinct levels. All of the analysis was performed with Minitab statistical software.

Response Surface Methodology

RSM is a modeling technique in which the relationships between inputs and outputs are described in terms of a second order polynomial [33]. This methodology makes use of statistical techniques in order to represent and determine the relationship between the design variables and the measured response. Furthermore, it also takes into consideration the effect of combined interactions between design variables, which is a critical aspect of PIM optimization. The general model equation of RSM is:

$$\eta = \beta_0 + \sum_{i=1}^{k} \beta_i x_i + \sum_{i=1}^{k} \beta_{ii} x_i^2 + \sum_{\substack{i=1 \\ i<j}}^{k} \sum_{j=1}^{k} \beta_{ij} x_i x_j \qquad (6)$$

Where η is the response of a set of k design variables $x_1, x_2, \ldots, x_k$, and β denotes fitting coefficients. Again, all of the analysis for RSM was performed with Minitab.

Artificial Neural Network

ANN is an extensive coordinated network of interconnected processing units, sometimes referred to as neurons, in which each unit receives input information from other neurons and calculates an output that is transferred to subsequent neurons. ANN can be trained to recognize patterns and to predict results of nonlinear functions, which makes them an ideal candidate for prediction and optimization of PIM processes. There are various training algorithms developed for different types of data. A Bayesian regulation back propagation training function was selected for this case study and all programming was done utilizing the Neural Network toolbox in MATLAB. The selected structure for the ANN is shown in Figure 26-Schematic of the selected ANN structure. The network consisted of 3 layers and 30 neurons.

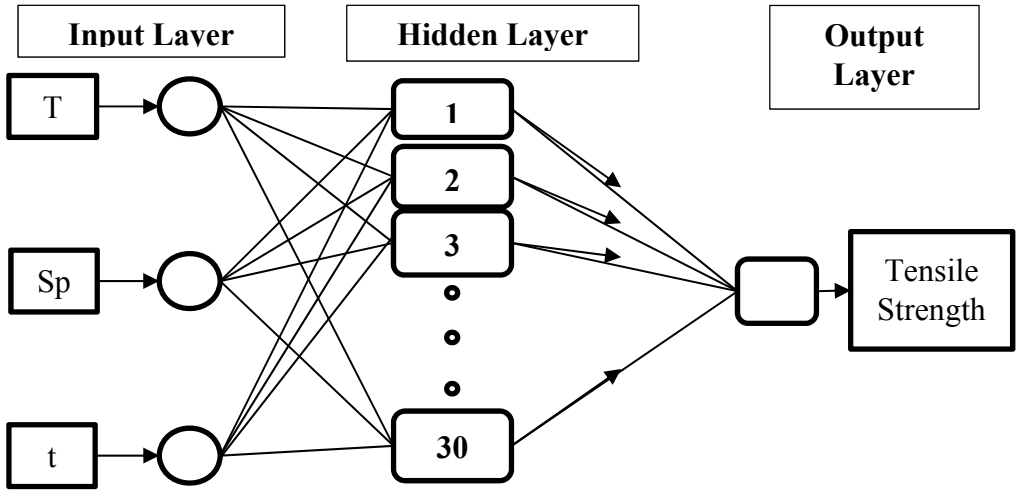

Figure 26-Schematic of the selected ANN structure

Results and Discussion

Taguchi Method

The performance indicator of S/N is shown in Table 2. This indicator is utilized by designers and engineers in order to characterize the effect of the different parameters on the process response. Parameter levels were: melt temperature 218°C, 246°C and 274°C; mold temperature 50°C, 85°C and 120°C; injection rate 45 mm^3/s, 100 mm^3/s and 120 mm^3/s; and packing time 2 seconds, 6 seconds and 10 seconds. Levels were based on suggested parameters by KANEKA Corporation and prior experience with this material. An injection rate of 45 mm^3/s was the slowest injection rate possible without getting short shots. Table 3 shows the rank of each of the parameters selected for the experiment. It can be observed that injection speed and holding time have the largest effect on tensile strength of SIBS, while mold temperature has the smallest effect. Figure 27 shows the main effect of each parameter on the tensile strength. Individual effects are calculated as the average response of all experimental runs under constant parameter levels. As expected, the curves

for injection speed and packing time are steeper, indicating more influence on the measured response. Also, in Figure 27 we can observe the levels that would produce the largest S/N ratio and ultimate tensile strength and predict its outcome without the need to run the experiment.

Table 2. S/N and Tensile Strength values for SIBS

T (°C)	T_m (°C)	Sp (mm^3/s)	t (s)	S/N	σ_{uts} (MPa)
218	50	45	2	24.32	16.5
218	85	100	6	23.63	15.3
218	120	120	10	23.60	15.1
246	50	100	10	24.08	16.0
246	85	120	2	22.66	13.6
246	120	45	6	24.00	15.9
274	50	120	6	22.69	13.7
274	85	45	10	24.37	16.6
274	120	100	2	22.45	13.3

Table 3. Injection molding parameter rank for SIBS

Level	T (MPa)	Tm (MPa)	Sp (MPa)	t (MPa)
1	15.64	15.41	16.33	14.48
2	15.18	15.16	14.85	14.94
3	14.51	14.76	14.15	15.92
Delta	1.13	0.65	2.17	1.44
Rank	***3***	***4***	***1***	***2***

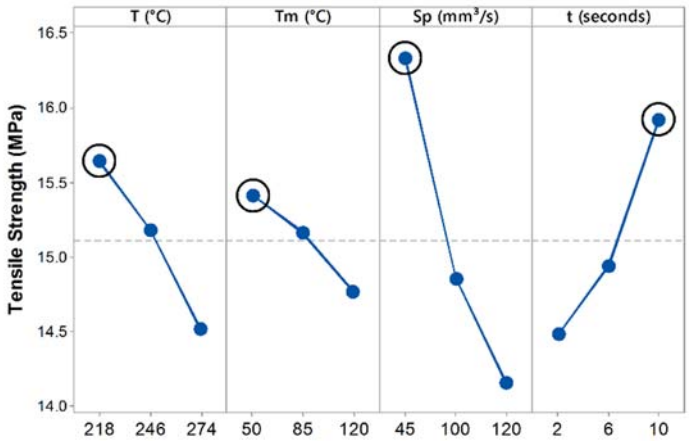

Figure 27-Individual effects of injection molding parameters on tensile strength of SIBS. Parameters with highest tensile strength and S/N are circled as predicted by Taguchi method

To calculate the ideal performance, the difference between average performance and the contribution from each optimal parameter is added to the average experimental response, as in the following example:

$$Y = \mu + (T_{218} - \mu) + (T_{M\,50} - \mu) + (Sp_{45} - \mu) + (t_{10} - \mu) \qquad (7)$$

where μ is the average performance, T_{218} is the average performance for nozzle temperatures of 218°C, $T_{M\,50}$ is the average performance for mold temperatures of 50°C, Sp_{45} is the average performance for injection rates of 45 mm^3/s and t_{10} is the average performance for packing times of 10 seconds.

According to this method, the predicted S/N ratio and tensile strength are 25.19 and 17.96 MPa respectively. Experimental validation of these parameter settings showed that Taguchi Method over predicts the tensile strength of SIBS. Samples fabricated at the optimum levels had an ultimate tensile strength of 17.25 MPa.

The effect of mold temperature on the tensile strength of SIBS is not as significant as the other injection molding parameters. The delta value in Taguchi designs is defined as

the difference between the maximum and minimum characteristic response across that given factor. In the case of SIBS, the delta value for the mold temperature effect is on par with the standard deviations of the settings tested, which was 0.65 MPa on average. Variation due to mold temperature changes is relatively insignificant in terms of effect on tensile strength for the range of temperature evaluated. Thus, the mold temperature parameter was removed from consideration to reduce experimental complexity and number of samples required in order to perform RSM and develop the ANN. A mold temperature of 85°C was selected as the standard for the set of samples fabricated for the remaining methodologies.

Response Surface Methodology

Samples were fabricated according to a Box-Behnken design for optimizing performance in order to fit the second order polynomial shown in Equation (6). Each factor value was spaced equally in order to cover most of the experimental domain [81]. Samples were fabricated and tested using different parameter settings according to the Box-Behnken design, which required 120 total samples. All tested parameters are shown in Table 4. Figure 28 shows the plot of residuals from the samples tested. As evidenced by the normal probability plot, residuals of SIBS specimens tested do not seem to deviate from a normal distribution. Although there are a few unusual observations that deviate from normality, the vast majority of residuals are normally distributed around zero. Furthermore, the observation order does not show any trend or particular pattern, which indicates consistency with stochastic error and no evidence that error depends on observation order.

Table 4. Parameters settings for RSM

T (°C)	Sp (mm^3/s)	t (s)
218	45	6
218	100	2
218	100	10
218	120	6
246	45	2
246	45	10
246	100	6
246	120	2
246	120	10
274	45	6
274	100	2
274	100	10
274	120	6

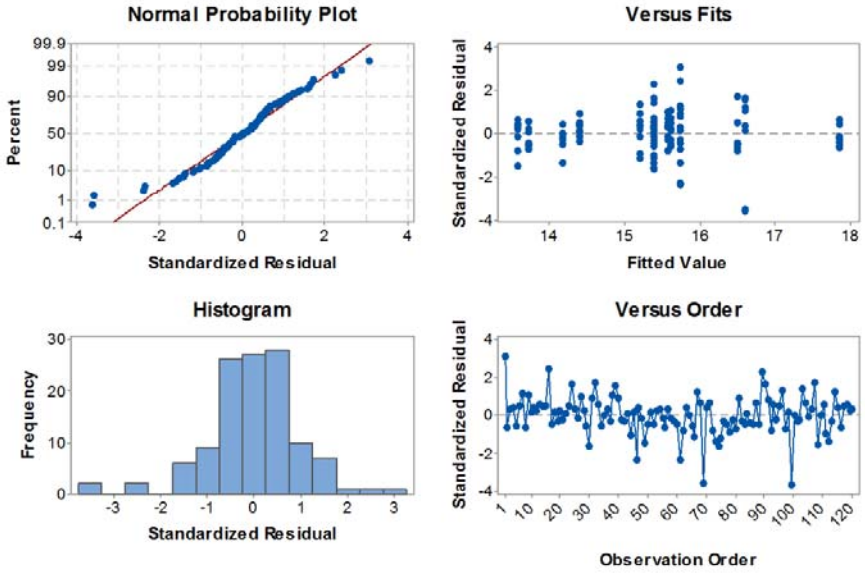

Figure 28-Residuals plot of SIBS samples tested

Figure 29 shows the main effect of the plastic injection molding parameters on the tensile strength of SIBS. As expected, the effect of temperature is concave down, reaching a maximum between 240°C and 260°C. This is the expected behaviour of tensile performance, which is limited by thermal degradation of the thermoplastic at high nozzle

temperatures and limited by incomplete material fusion at low nozzle temperatures. Comparing Figure 27 and Figure 29 shows a very different trend in the effect of nozzle temperature calculated by the different methodologies. The differences between these figures is a result of the differences in experimental designs between Taguchi orthogonal arras and the Box-Behnken design. Moreover, a larger fraction of the full factorial experimental set is covered for RSM than for Taguchi method, as it contains a larger combination of parameters together with less variables, capturing in more depth the effect that each parameter has over the tensile strength of SIBS. The results indicate that injection speed and tensile strength are inversely related, while packing time and strength are directly proportional. It was observed during testing that specimens injected at a lower speed had an abrupt failure and a smooth, relatively uniform failure surface. Specimens injected at faster rates suffered from cracks at multiple locations in the gauge section and had jagged failure surfaces. Figure 30 shows an image of two tested specimens side by side, which highlights the different failure mechanisms. The specimen on the left was injected at faster rates than the specimen on the right. These different failure behaviors and failure surfaces have not been previously reported for SIBS, and is likely relevant to SIBS with different polystyrene (PS) content or polymer chain structure. It is likely that the fast injection rates are detrimental to the separated microphase formation of the spherical PS domains leading to a reduction in tensile strength of the material. It might also be plausible that slow injection rates minimize air entrapments as the plastic is flowing into the mold. Microvoids formed during the faster injection process may lead to premature and non-uniform breakage. Of note is the geometry of the failure surface for the higher quality sample on the right side of the figure, which was injected at a slower speed. Failure occurred wholly

along the plane of maximum shear stress oriented at 45 degrees to the tensile axis. Figure 31 through Figure 35 show scanning electron microscopy (SEM) images of the failure surfaces. Specimens were suppetered coated with gold in order to reduce charging and avoid burning the specimens. The slow injected specimen shows a relatively smooth surface through the entire section, whereas the fast injected sample shows multiple cracks that propagated through the specimen. From the microscopy images there is no indication of unfused pellets through the specimens, which suggests that the different responses of SIBS are due to microvoids or weakend interphase between the spherical PS domains and the isobutylene rather than incomplete fusion of pellets.

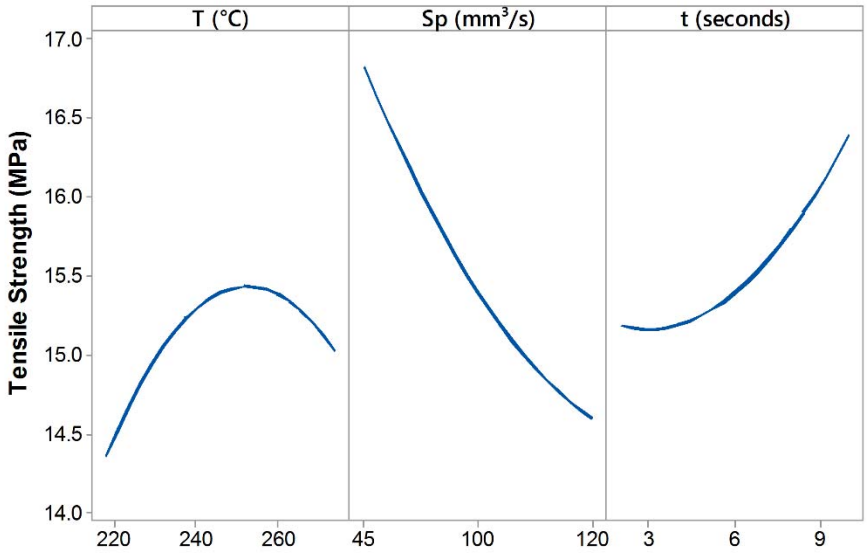

Figure 29-Main effects of injection molding parameters as calculated by RSM

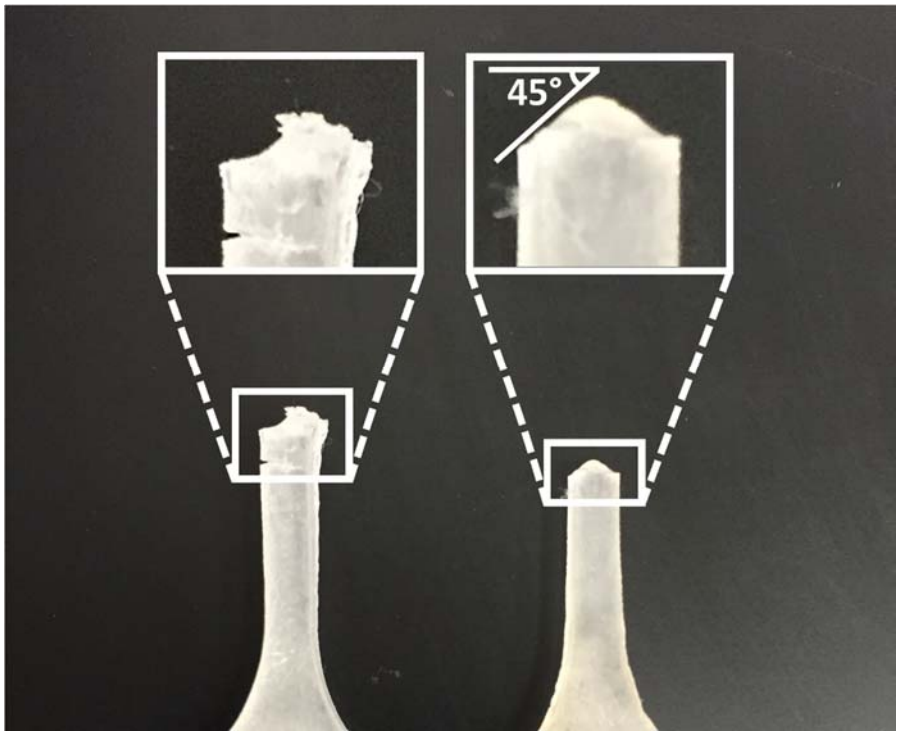

Figure 30-Narrow section failure of two specimens. Left specimen was injected at fast rates and the specimen on the right was injected at slow rate

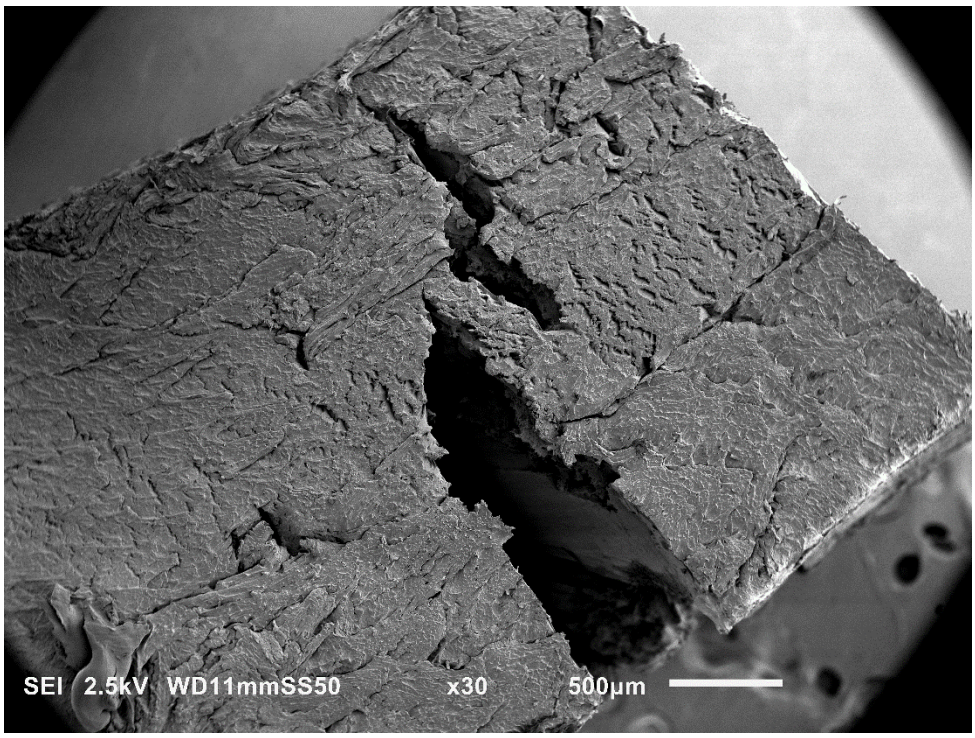

Figure 31-SIBS fast injection side view

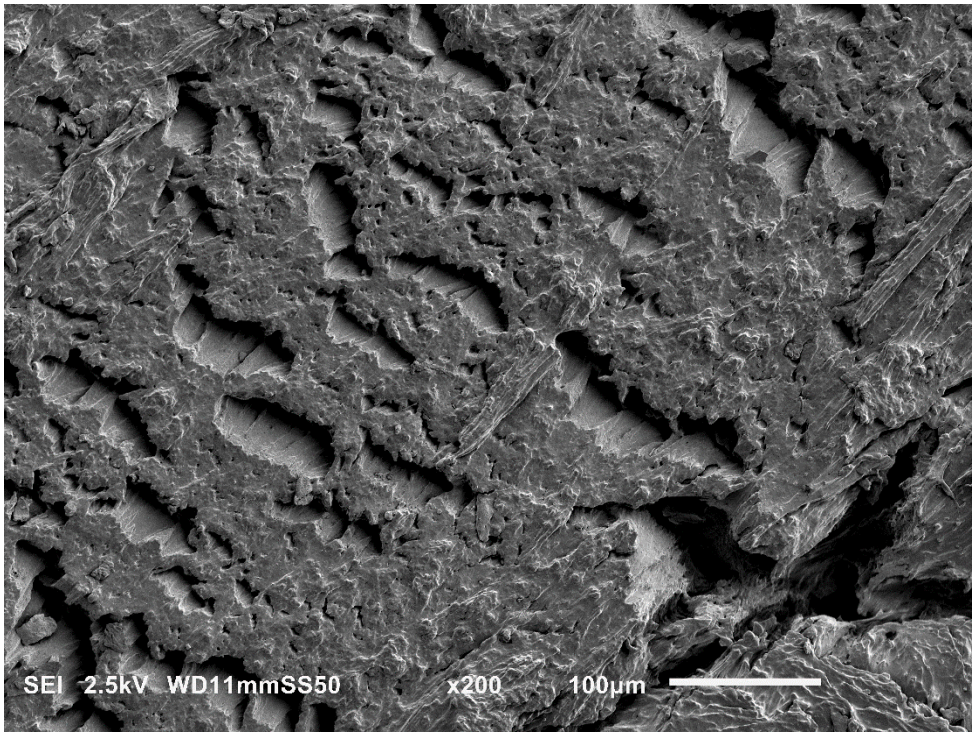

Figure 32-SIBS fast injection side view

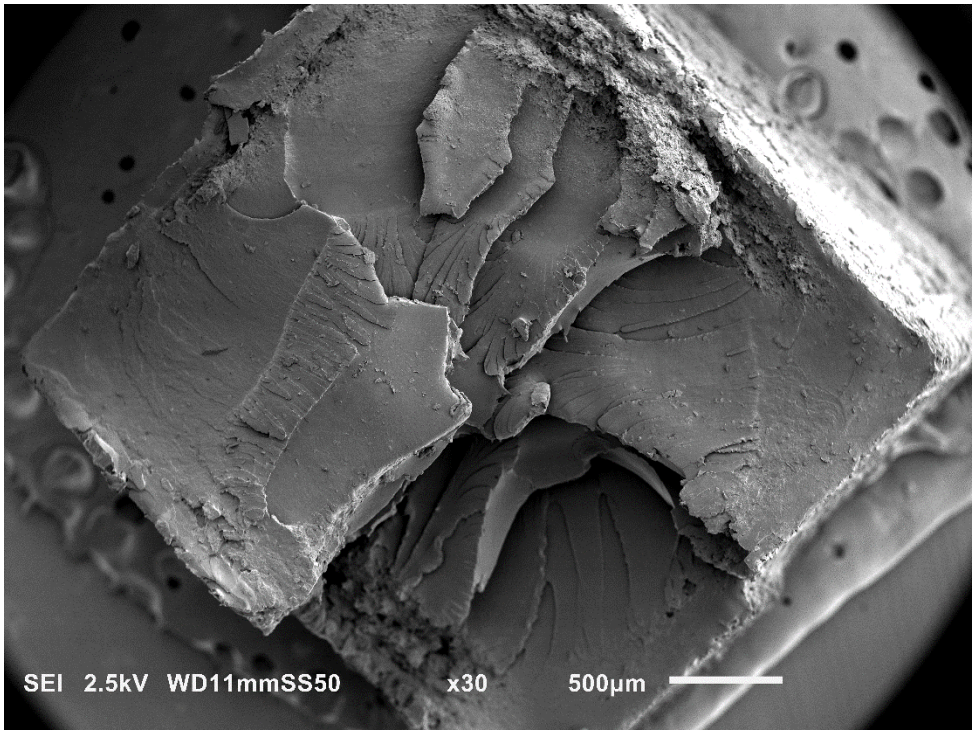

Figure 33-SIBS fast injection failure surface

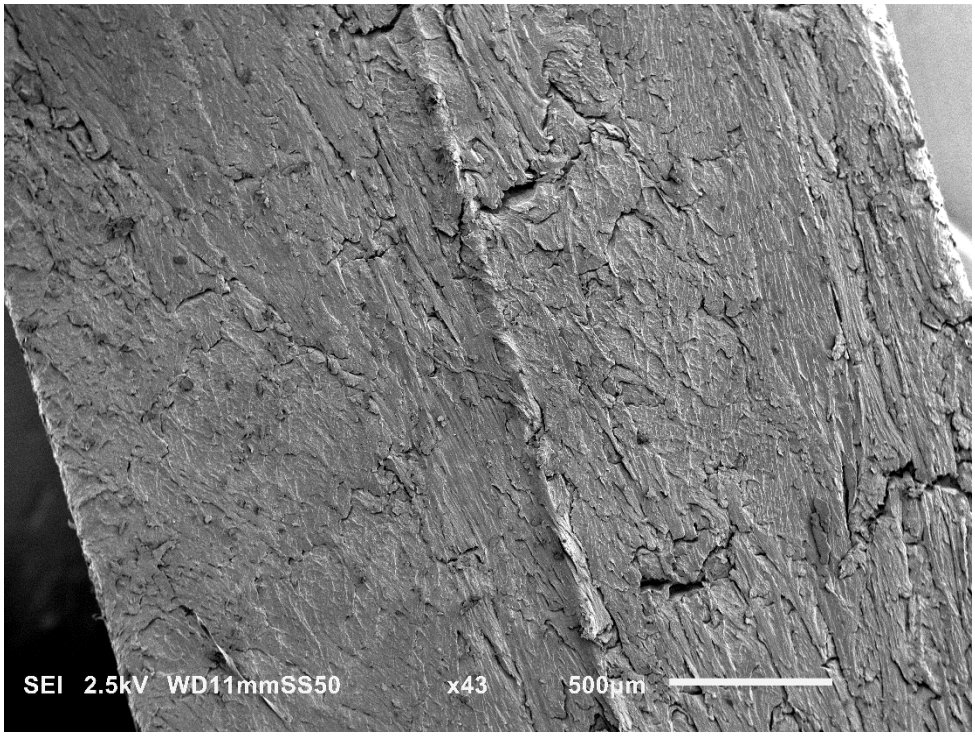

Figure 34-SIBS slow injection side view

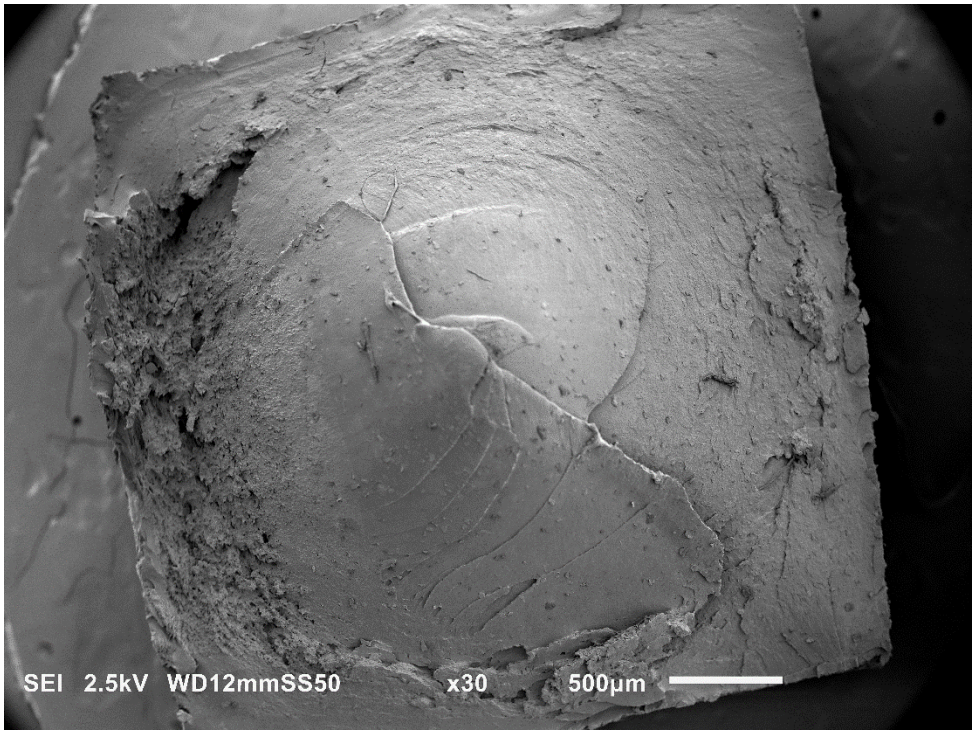

Figure 35-SIBS slow injection failure surface

Contour plots and interaction plots are shown in Figure 36 and Figure 37 respectively. Contour plots are produced using equation (6), the calculated fitted coefficients and by holding one of the variables constant at a certain value. Levels kept constant are shown as "hold values" in Figure 36. Interaction plots are the mean values for a factor with the level of the interacting factor held constant. In the event of an interaction between factors, curves will not be parallel to each other, as seen for the nozzle temperature and packing time interaction. This shows that the only interaction between selected parameters is packing time and nozzle temperature. Injection rate proved to have the largest effect on the tensile strength of SIBS. The contour plots show the significant difference in ultimate tensile strength as a result of slower injection rates and longer packing times. This is seen by the increasing tensile strengths moving along the packing time axis and against the injection rate axis. This is not the same response for nozzle temperature as evidenced by the curved contours achieving higher values at around 250°C. This is readily apparent on the interaction plots. Curves representing tensile strength at different injection speed (Sp) levels deviate significantly from each other, further highlighting the impact of injection rate. Moreover, the slope of tensile strength with respect to speed coupled with packing time seems to be the driving interaction parameter for the resultant strength of the material. It is possible that the main effect of a slower injection rate is the more uniform temperature of the plastic flow front as it passes through the nozzle. The result is a more consistent morphology and improved interface quality, thereby improving the tensile strength of the material.

These results are consistent with the Taguchi design of experiment. However, the temperature setting that would maximize the tensile strength of SIBS does not lie at the

same temperature level predicted by the Taguchi method. The built-in optimization tool available in Minitab for the response surface methodology can maximize or minimize desired responses based on the developed quadratic model. The optimal parameter settings that resulted from the analysis were 245°C, 10 seconds packing time and an injection rate of 45 mm^3/s. Furthermore, the ultimate tensile strength predicted for these parameters settings is 17.9 MPa. Experimental validation of these optimized parameter settings yielded an ultimate tensile strength of 17.7 MPa, which is well within the 95% confidence interval of the prediction. This result is also an improvement over the reported tensile strength by Lim et al. on the tensile strength of the same type of SIBS copolymer from the same manufacturer [82]. Their study reports results of ultimate tensile strength of 12.7 ± 0.7 MPa at a strain rate of 500mm/min fabricated via compression molding at 185°C. The 17.7 MPa tensile strength at the same strain rate reported in this study is an improvement of approximately 40%.

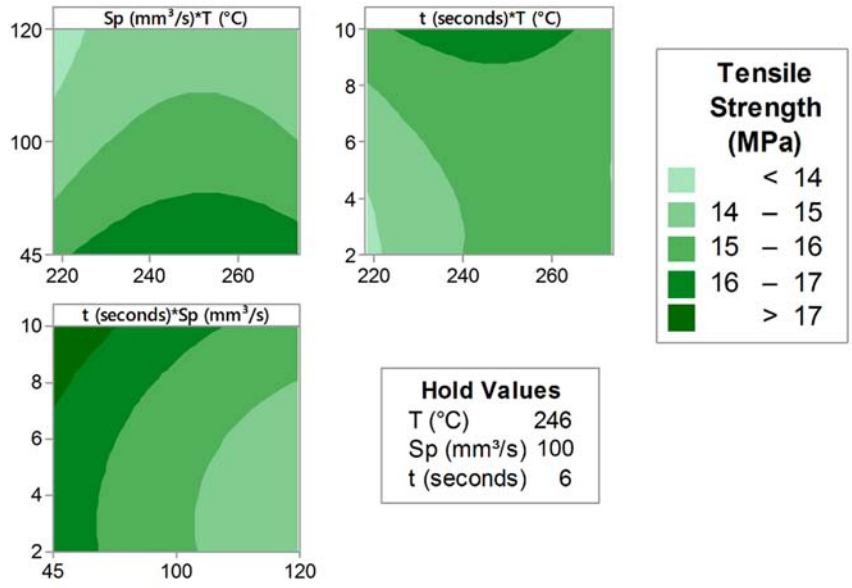

Figure 36-Contour plots of SIBS tensile strength at different parameter levels

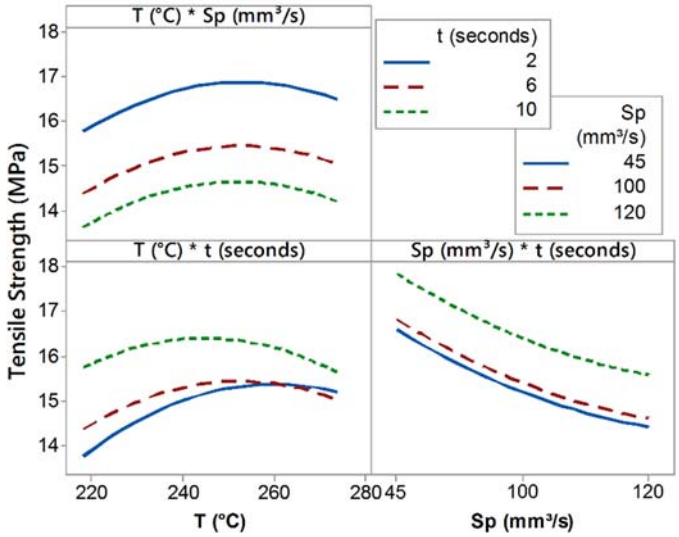

Figure 37-Interaction plots of injection molding parameters

Artificial Neural Network

The back propagation neural network proposed in this study has three layers: an input layer, a hidden layer and an output layer. The samples tested were randomly divided into two sets for training and validation. The training set consisted of 16 different parameter settings, whereas the validation set was composed of three randomly selected parameter settings. Each of the 19 parameter choices were composed of the average response output of 8 samples with the same parameter settings. These parameter choices were the combination of the same parameter levels used for Taguchi method and RSM shown in Table 2 and Table 4 respectively. The network was composed of 30 neuron units for pattern recognition. The number of neurons was based on iterating training and validation runs until marginal improvements were observed. Performance was not noticeably affected by including additional units beyond 30, while computation time using this number of neuron units remained very low.

The input layer receives the information for parameter settings for every data point used in training. It then maps the data to the hidden layer by means of a hyperbolic tangent sigmoid transfer function, and finally projects the information to the output layer by means of a linear transfer function. The hyperbolic tangent transfer function updates the weights and bias values of each neuron every iteration according to the Levenberg-Marquardt optimization methodology. The goal of the optimization training of the ANN is the minimization of the Mean Squared Error (MSE).

Figure 38 shows the performance of the artificial neural network at each training iteration. Best performance of the neural network was measured by means of the MSE, which occurred at iteration number 80 and beyond. Once the training of the network was completed, validation was performed in order to evaluate the accuracy of the tensile strength prediction from the injection molding parameters. Figure 39 shows prediction values of both RSM and ANN methods together with the experimental results. These samples were designated as the validation set of the neural network so they were not used for training purposes.

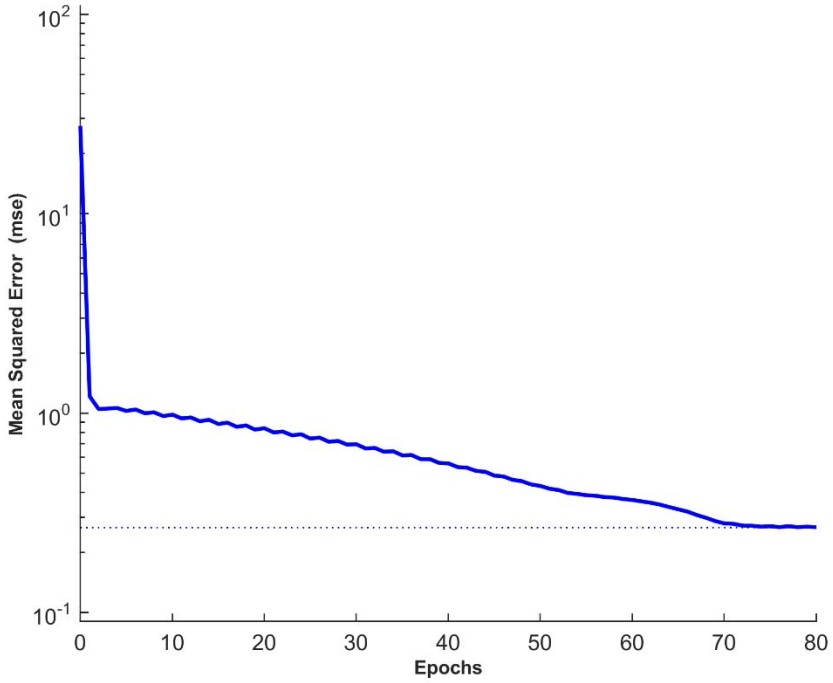

Figure 38-Training performance of the Artificial Neural Network

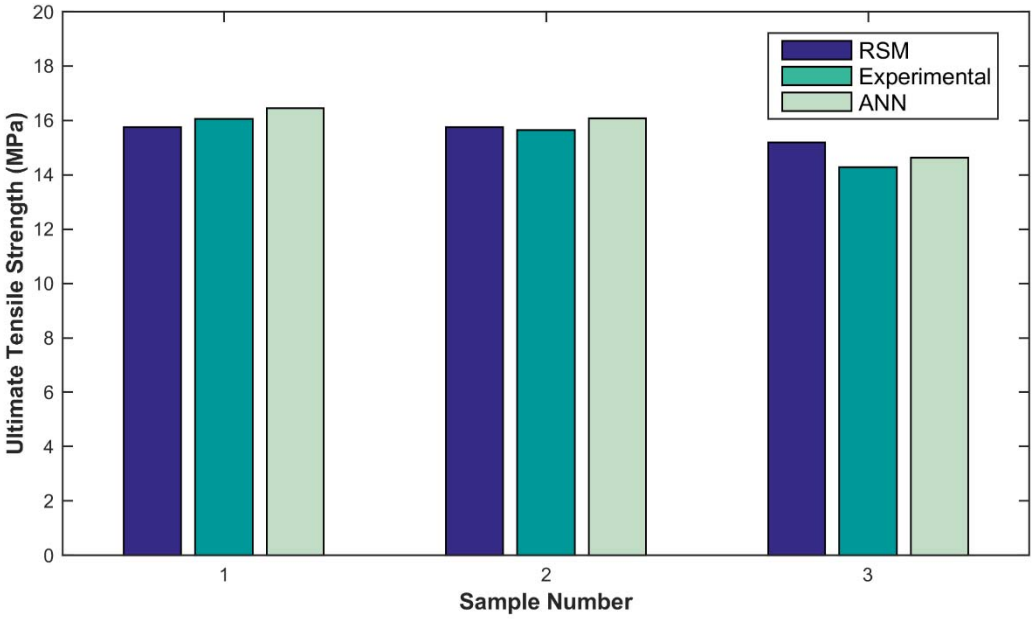

Figure 39-Validation of ANN and RSM methods with experimental results

As shown in Figure 39, ANN over predicts the tensile strength of SIBS for all three samples. RSM over predicted in two cases, and under predicted in the third. Both methods prove successful in predicting the tensile strength of SIBS based on injection molding parameters. The RSM method has an average error of prediction of 3.00% while the ANN performed slightly better with an average error of 2.55%. Both RSM and ANN prove to be useful methods for modeling tensile strength of SIBS based on injection molding parameters. Furthermore, both methods can be easily optimized in order to search for absolute maxima or minima according to the desired response. Taguchi methods proved useful for initial simplification of experimental conditions by reducing the number of significant parameters. Further, Taguchi methods are suitable for providing initial parameters for follow up optimization using other methodologies such as RSM and ANN. However, this approach is limited to discrete parameters and cannot calculate intermediate levels of factors. This is a limiting problem because most, if not all, of the parameters that drive plastic injection molding are continuous. By just utilizing this technique it might not be possible to obtain completely optimized responses when optimal settings fall in between the chosen levels for the Taguchi orthogonal array. Moreover, Taguchi method overestimated the ultimate tensile strength of SIBS from the signal to noise ration function, showing that a more detailed experimental plan is needed to capture material properties from fabrication parameters.

These results and those reported elsewhere in the open literature highlight the importance of processing conditions on mechanical performance of SIBS. Reported tensile strength of this specific SIBS formulation, for example, ranges from 12.7 MPa to 17.7 MPa [82, 83]. In the work by Lim et al., the use of nanofillers was investigated in order to

improve mechanical properties of compression-molded SIBS, though no consideration was given to the effect of process parameters. No improvement was observed from using nanoclay-reinforced SIBS 103T and ultimate tensile strength decreased with increasing filler content. However, no attempt at processing parameter optimization was made. The work we present here emphasizes the importance of optimizing the fabrication process for thermoplastic elastomers to achieve optimal mechanical performance. Furthermore, the addition of nanofillers modifies the rheological properties of thermoplastics, so it is imperative that an independent optimization is also performed for the reinforced plastic. The varying morphology resulting from different processing conditions may be at the core of these discrepancies in maximum tensile strength of SIBS. It is likely that there is a significant effect on the interface between the glassy polystyrene spheres and the rubbery isobutylene domain based on processing parameters. The PS spheres have been characterized in other studies, wherein it is reported that the average diameter of the spherical PS domains is 10 nm and 50 nm for contents of 20 wt. % and 30 wt. %, respectively [22, 82]. The nanometer-scale size of the PS spheres will necessarily result in significant interfacial surface area. As a result, the quality of this interface may have an exaggerated effect on the mechanical properties of the material. For example, if the interface is not fully developed and fused together, the spherical domains may be acting as impurities. This weakened interface between incompatible regions in the block copolymer might be leading to premature failure and stress cracking, thereby significantly deteriorating the mechanical properties. The different failure surfaces observed (Figure 30 through Figure 35) is suggestive of this type of condition, and further bolsters the theory that processing conditions have a major effect on the morphology and micromechanics of

the copolymer. This previously undocumented behavior is expected to immediately contribute to the advancement of the usage and fabrication of SIBS-based biomedical implants and devices.

Conclusion

This work reports methods and results of injection molding parameter optimization on the tensile strength of SIBS, a biocompatible thermoplastic elastomer used primarily in biomedical applications. The triblock copolymer was composed of 30 wt. % PS, 70% polyisobutylene, and had a molecular weight of 105,000 g/mol. The injection molding parameters varied in order to maximize tensile strength were melt temperature, mold temperature, packing time and injection rate. Initially, a Taguchi orthogonal array was utilized to determine rank of importance of the selected parameters. Injection rate was found to be the most important parameter driving tensile strength, while mold temperature was the least significant. Subsequently, a response surface methodology was performed in order to model and predict tensile strength based on melt temperature, packing time and injection rate. Simultaneously, a back propagated artificial neural network was trained with the same empirical data in order to compare performances of the different methods. Both methods were able to predict tensile strength accurately, although the neural network approach was slightly superior. The optimized tensile strength response was predicted to be 17.9 MPa, which was validated by an experimentally measured tensile strength of 17.7 MPa. This value is approximately 40% higher than SIBS tensile strength reported elsewhere in the literature, highlighting the usefulness of injection molding parameter optimization for SIBS and other thermoplastic elastomers. Based partially on fracture surface analysis, it is suggested that the sensitivity of SIBS to injection molding parameters

may be a result of the quality of the interface between the spherical nanoscale polystyrene domains and polyisobutylene. Moreover, this work serves as a guideline to optimize other thermoplastic elastomer block copolymers to achieve desired properties without the need to use additives or nanofillers, which may compromise biocompatibility. Further, these results emphasize the necessity of optimizing the fabrication process concurrently with adding or modifying reinforcements. Failure to do so may mitigate any potential improvements due to the reinforcement as a result of non-optimal processing.

Chapter 5

Materials and methods

KANEKA Corporation generously provided four different SIBS formulations, marketed as SIBSTAR 103T, 102T, 73T and 72T. Table 5 shows the composition of the linear copolymers and their molecular weights according to the material data sheet provided by KANEKA. Gel permeation chromatography was performed on all formulation of SIBS in order to verify the molecular weight with those values reported in Table 5. Pellets were used as received and samples were fabricated via compression molding. All samples were compressed for 10 minutes using 8 MPa of pressure. Once the first cycle was finished, the sheets were allowed to cool down to room temperature. Sheets were then folded and a new cycle was applied to ensure complete fusion of pellets. The result was clear sheets with no weld or flow marks. A temperature of 193 °C was used for SIBS 102T, 72T and 73T; SIBS 103T was compressed at a temperature of 220 °C, due to its higher melt temperature. A custom-made aluminum mold was used to fabricate consistent, 0.5 mm thick sheets of SIBS. The molded SIBS was allowed to cool to room temperature prior to cutting into squares of approximately 60 mm by 60 mm. Samples were stored in an oven at 65 °C for one week in order to remove all residual moisture prior to lipid immersion. The weight was monitored via a high precision analytical balance until all samples had constant weights over a period of 24 hours.

Table 5. SIBS compositions

	SIBS 103T	*SIBS 102T*	*SIBS 73T*	*SIBS 72T*
Styrene content (wt. %)	30	15	30	22
Molecular weight (g/mol)	106,000	117,000	76,000	75,000

Experimental protocol

Dry sample weights were recorded via a high precision analytical balance and thickness values were measured using a rubber thickness gauge to ensure precise measurement of the soft material. Five thickness measurements were recorded and averaged; one at each corner and one on the center of the square sample. Glass containers were filled with palm oil and placed in a constant temperature water bath at 37 °C. Once the oil containers had reached equilibrium temperature, the SIBS samples were immersed and their weight was recorded periodically. At each measurement interval, samples were carefully removed from the oil and dabbed with oil-absorbent cloths to remove as much of the surface oil as possible. Samples were then rinsed in a glass container with acetone for twenty seconds and placed on lint-free cloths to dry. Acetone was the selected solvent because it is moderately volatile and completely nonaggressive to SIBS (no physical changes were observed after 72 hours of full immersion). This cleaning procedure is taken from ASTM D543, on cleaning nonvolatile, nonwater-soluble organic liquids. This ensured full evaporation from the surface prior to weighing. Once the surface acetone had evaporated completely, the weight increase was recorded and specimens were replaced in their respective containers to continue lipid exposure. Thickness measurements were performed on a weekly basis after weighing. This custom procedure was created as a modification and combination of ASTM D543 for evaluating the resistance of plastics to chemical reagents and ASTM D5229 for moisture absorption properties and equilibrium conditioning of polymer matrix composite materials.

Specimen microscopy

Atomic force microscopy (AFM) was performed in samples before and after oil immersion to visualize changes in phase separation. AFM images were recorded with a Bruker MultiMode in tapping mode using etched silicon probes with nominal resonant frequency of 300 kHz and nominal spring constant of 40 N/m. All scans were performed at scanning speeds of 1-2 Hz.

Scanning electron microscopy (SEM) was performed in samples after lipid saturation was reached. Small samples were cut from specimens using a sharp blade and sputter coated with gold prior to imaging in a Jeol JSM-6010PLUS/LA SEM. All samples were imaged under vacuum at an accelerating voltage of 2 kV to reduce charging and avoid melting the polymer in the chamber.

Results and discussion

Gravimetric lipid uptake

The detailed solution to the one dimensional Fickian diffusion equation is readily available in the literature, so it will not be discussed here. The mass gain due to fluid uptake is described by the following equation [49]:

$$\frac{M_t}{M_\infty} = 1 - \frac{8}{\pi^2}\sum_{0}^{\infty}\frac{1}{(2n+1)^2}e^{-\frac{D(2n+1)^2\pi^2 t}{h^2}} \quad (8)$$

Where M_t and M_∞ are the percentage mass uptake at time *t* and at equilibrium respectively, *D* is the diffusion coefficient and *h* is the sample thickness. All experimental lipid uptake data was fitted with Equation (8) and the diffusion coefficient and saturation lipid content were calculated by least squares regression.

The experimental measurements of lipid uptake for SIBS 103 and 102 are shown in Figure 40. The dashed line represent the least squared error (LSE) Fickian fit from Equation (8). The lipid diffusion dynamics follow the Fickian model very closely, although there is a slight deviation after saturation is reached. These deviations could be attributed to relaxation of the polymer network and the associated swelling of the polymer, which is a well-documented phenomenon [53]. As the polymer network swells, voids are created that allow the intrusion of additional lipids, which in turn continue to relax the network. This behavior is most readily apparent for SIBS 102, where the fluid content slowly drifts from the predicted Fickian saturation percentage. In other SIBS compositions, deviations from Fickian equilibrium in the form of mass loss are observed at the later stages of diffusion. These compositions may be more susceptible to earlier onset breakdown which can be attributed to chemical interactions between polymer and penetrant. The diffusing fatty acids may be interacting with the matrix and creating free radicals that are released from the network or scissioning segments of the polymer chains of the network, leading to the mass loss observed for SIBS 103. This phenomenon has been documented in other, similar polymers subject to fluid contamination [54, 84].

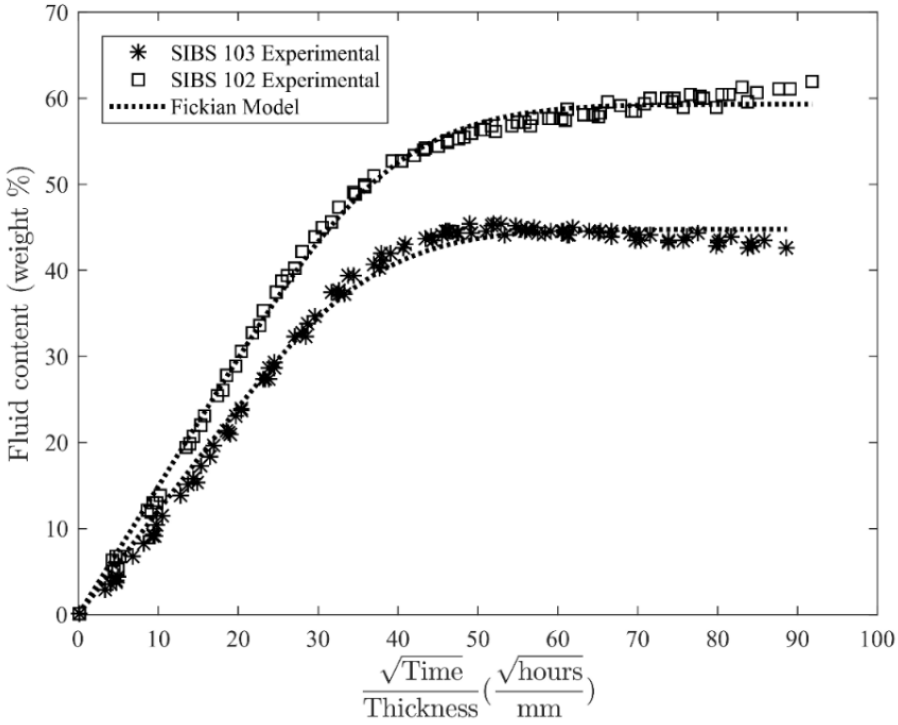

Figure 40-Lipid uptake curve for SIBS 103 and 103 with LSE Fickian fit

The gravimetric lipid uptake curve for SIBS 72 is shown in Figure 41 together with the Fickian model from Equation (8). As the specimens approached lipid saturation, visible degradation was observed for all SIBS 72 specimens. Visible cracks began propagating through the samples, and most corners of the specimens began to physically deteriorate. With continued exposure to lipids, cracks continued to grow until samples began to physically break apart upon handling. Figure 42 shows a picture of one of the SIBS 72 specimens after prolonged lipid immersion. The degradation of the sample is evidenced by the number of visible cracks that propagated through the sample and the deformation from the original (square) shape. This behavior is likely of similar form and origin as that observed for the trileaflet heart valve that failed animal testing due to plasticization and surface cracking [77]. The combination of low molecular weight and low styrene content of SIBS72 likely contributes to the initiation and growth of these cracks. The extremely

high lipid saturation content induced a large swelling deformation that weakened the matrix and facilitated the crack growth due to the induced plasticization. As noted in Figure 41, data points beyond the vertical dashed line were not used for the fit because of the significant breakdown of samples and the associated loss of uptake measurement integrity beyond this threshold. Average fluid content and specimen swelling (see swelling section) started to decrease past this point, skewing the Fickian fit.

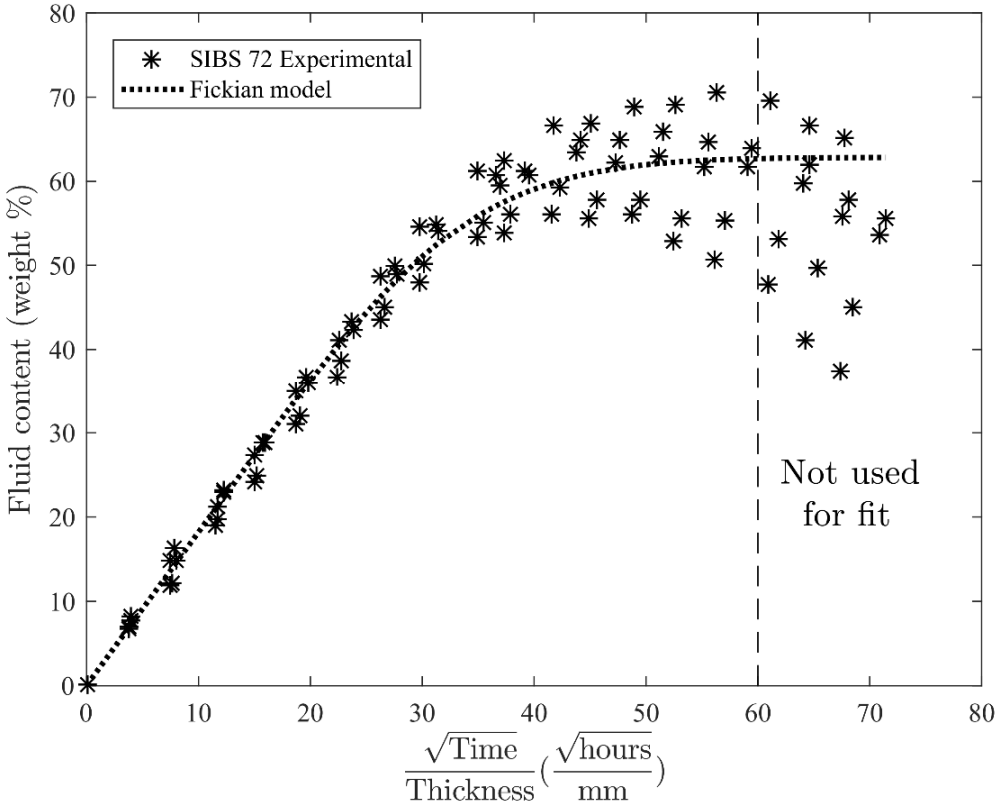

Figure 41-Lipid uptake curve for SIBS 72 with LSE Fickian fit

Figure 42-SIBS 72 Specimen with visible cracks due to long exposure to lipid-rich environment

Using the calculated model parameters from the least squared error fit from SIBS 103, 102 and 72, it is possible to predict the parameters for SIBS 73 based on molecular weight and styrene content. A first order polynomial model, Equations (9) and (10), based on the polymer composition shown in Table 5 was used to predict the diffusion coefficient and saturation lipid content.

$$D = \alpha M_w + \beta w_s \tag{9}$$

$$S_\infty = \gamma M_w + \delta w_s \tag{10}$$

Where M_w is the molecular weight in g/mol, w_s is the styrene content by weight percentage and α, β, γ and δ are fitting coefficients. The predicted behavior is shown in Figure 43 together with the experimental results and the least squared error Fickian fit. As shown in the figure, the new model slightly over predicts the lipid uptake rate of SIBS 73, but it still captures the overall trend with excellent fidelity. In addition, the model slightly under

predicts the saturation lipid content of SIBS 73 compared to the least squared error fit, but it still captures the data to an excellent degree. A summary of the recovered diffusion parameters is shown in Table 6. It can also be seen in Figure 43 that there is some deviation from Fickian equilibrium past 50 hours$^{1/2}$/mm. This is due to relaxation and/or swelling effects in the polymer matrix, and is not predictable using the Fickian model. However, it is realistically unlikely that SIBS would ever experience such a high lipid content *in vivo* as the simulated experiment makes use of pure palmitic oil. For that reason, the Fickian model was used because it best represents diffusion kinetics and it captures the initial uptake trends to an excellent degree.

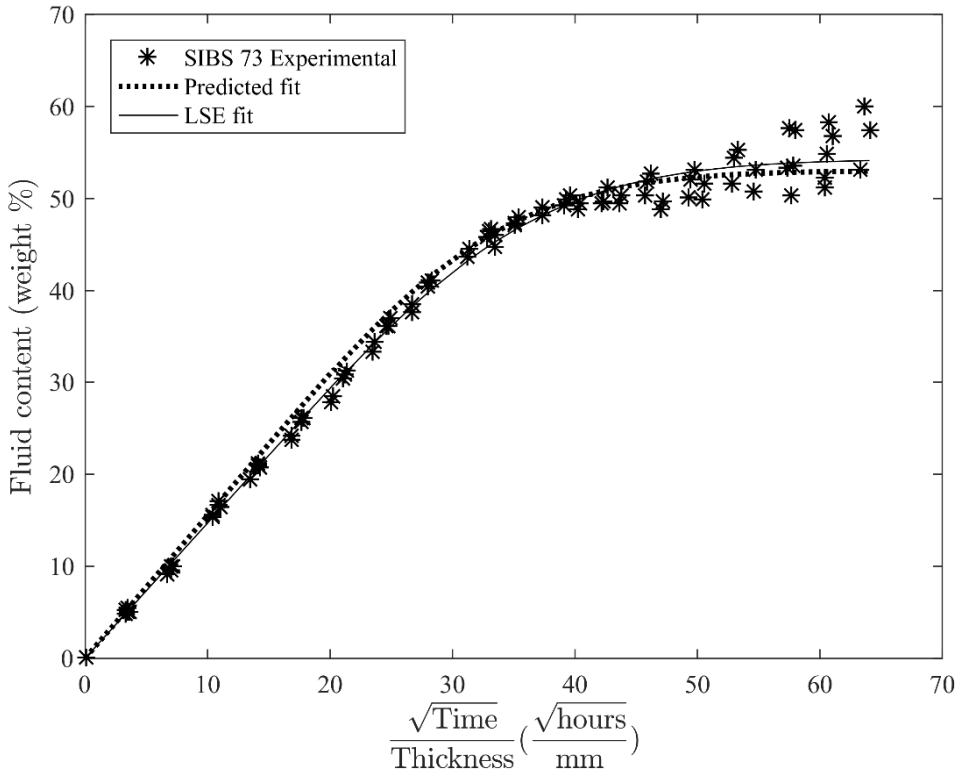

Figure 43-Lipid uptake curve for SIBS 73 with predicted Fickian fit and LSE Fickian fit

Table 6. Recovered diffusion parameters for all types of SIBS

	SIBS 103T	*SIBS 102T*	*SIBS 72T*	*SIBS 73T*	
	LSE	*LSE*	*LSE*	*Predicted*	*LSE*
Diffusion Coefficient $(10^4 \times \frac{mm^2}{hour})$	1.4249	1.2401	1.6481	1.6824	1.4396
Saturation Lipid Content (%)	44.78	59.31	62.84	53.03	54.26

It is readily apparent from these results that there is an inverse relationship between polystyrene content and lipid saturation content, which suggests the soft phase has a higher affinity towards the palmitic and oleic fatty acids found in palm oil. This conclusion is supported by AFM results, as shown in Figure 44. AFM phase imaging was performed for SIBS 103T specimens before and after oil immersion in order to visualize changes in phase separation. Samples imaged before immersion were consistent with morphology reports elsewhere [18, 25]. It was observed that after immersion the observable diameter of the styrene cylindrical/spherical domains was reduced from 30 nm to 26 nm, and that the separation between cylinders/spheres increased from 46 nm to 59 nm. Figure 44 show the polystyrene cylinders/spheres in dark color and the isobutylene in lighter color. This is not a shrinking of the polystyrene domains but rather a swelling of the isobutylene that engulfs the polystyrene as seen by the AFM phase image. There is a clear difference in image quality before immersion and after immersion. This is due to the isobutylene phase swelling and covering the styrene domains, reducing the contrast between phases, effectively reducing image quality. Moreover, the uneven swelling of the specimen increases the surface roughness and deteriorates image quality while scanning via AFM.

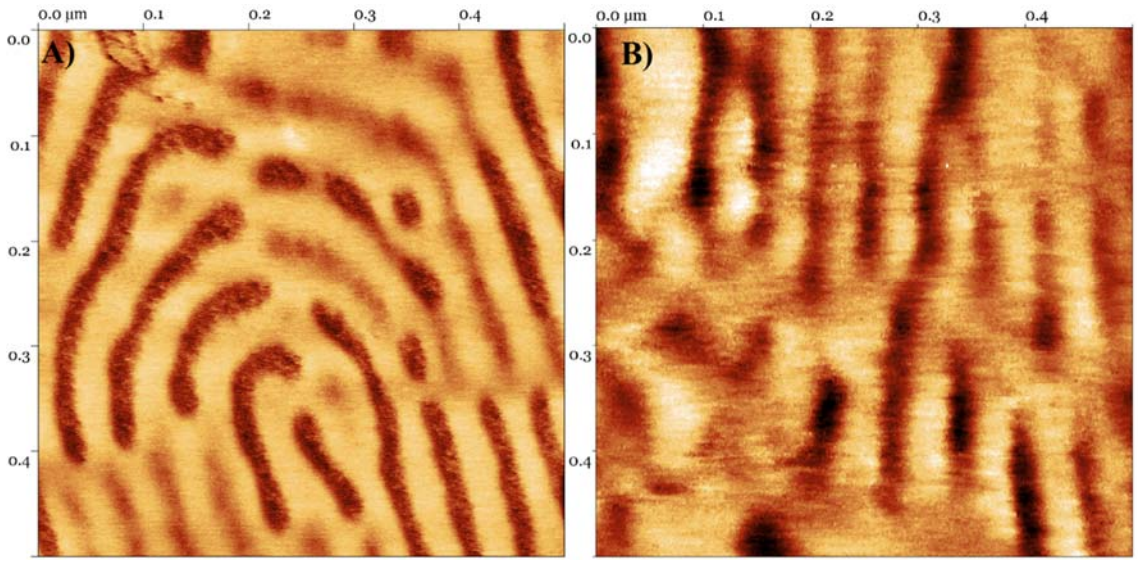

Figure 44-(A) SIBS 103T AFM phase image before lipid immersion. (B) SIBS 103T AFM phase image after lipid immersion

Even though the polystyrene phase exhibits a lower fluid saturation content than polyisobutylene, lipid diffusion in polystyrene occurs more quickly, as evidenced by the larger diffusion coefficient of 103 compared to 102. Higher molecular weight is likely desirable for most applications, as it contributes to lower both lipid saturation content lipid uptake rate. It is very likely that higher molecular weight SIBS has less free space that available for occupation by fatty acids, leading to lower saturation values. Phase separated copolymers with higher molecular weight also exhibit higher network rigidity due to increased physical cross-link density. A more rigid network would not plasticize and swell with the intrusion of fatty acids as readily as a less rigid one, leading to lower void volume and reducing the saturation fluid content as we observe here.

The relationship between SIBS molecular weight, phase composition, lipid uptake rate, and equilibrium lipid content is critical to the performance and longevity of the material in lipid-rich environments. The ability to model and predict this relationship is necessary for the design of long-term SIBS-based implantable devices. Subsequent to developing a

thorough understanding of these interactions, there will exist a need to correlate the degree of expected lipid contamination with the observed relaxation in terms of mechanical and viscoelastic properties for implants that will be subject to loading, such as artificial heart valves or intervertebral disk implants. Figure 45 shows a useful graph of the expected lipid uptake behavior for different SIBS formulations. Selection of a reasonable limit on lipid uptake rate and equilibrium content would allow the designer to narrow the range of potential SIBS formulations. Based on these two parameters, the time-dependent profile of lipid uptake can be fully defined. It should be noted that the model presented here is based on 100% palm oil exposure, but both modeling and experimental methods are readily transferrable to other lipids, including formulations intended to exactly duplicate the conditions of a specific *in vivo* application. The first order polynomial model described above was used to produce the expected diffusion parameters as functions of styrene content and molecular weight. As evidenced by Figure 40-Figure 43 and Table 6, higher molecular weight and higher styrene content seems to be preferred for stability and resistance to lipid-induced plasticization. Throughout the measurements, visible deformation was observed for most types of SIBS. The most stable type, SIBS 103, showed close to no change in geometry and experienced no obvious cracking even after reaching saturation. Type 73 showed very slight deformation subsequent to reaching saturation. In addition, visible blistering was observed on the surface of the specimens during the approach to equilibrium, indicating that the fatty acids might be concentrating in localizations within the polymer matrix instead of being homogeneously distributed throughout. An SEM image of a blister in a SIBS 73 sample is shown in Figure 46. As it can be seen from the figure, the central part of the image is bulging out compared to the

periphery of the image. These blisters were visible to the naked eye and occurred consistently across all SIBS 73 samples. SIBS 102 showed visible warping and stretching of samples shortly after starting the immersion process, but it did not show visible degradation such as surface cracking or blistering as observed for SIBS 73. SIBS 72 showed deformation and visible degradation as saturation was reached; the surface of all specimens started developing dimples and ridges until surface cracks appeared through all specimens, while corners were chipped and specimens became extremely frail. An SEM image of a surface crack for SIBS 72 is shown in Figure 47. Again, in the central part of the figure the crack can be clearly seen through the polymer sample. The most noticeable physical changes (blistering and cracking) happened to samples of SIBS 73 and 72. These compositions have lower molecular weight, which indicates higher molecular weight improves physical stability of samples when exposed to lipid-rich environments.

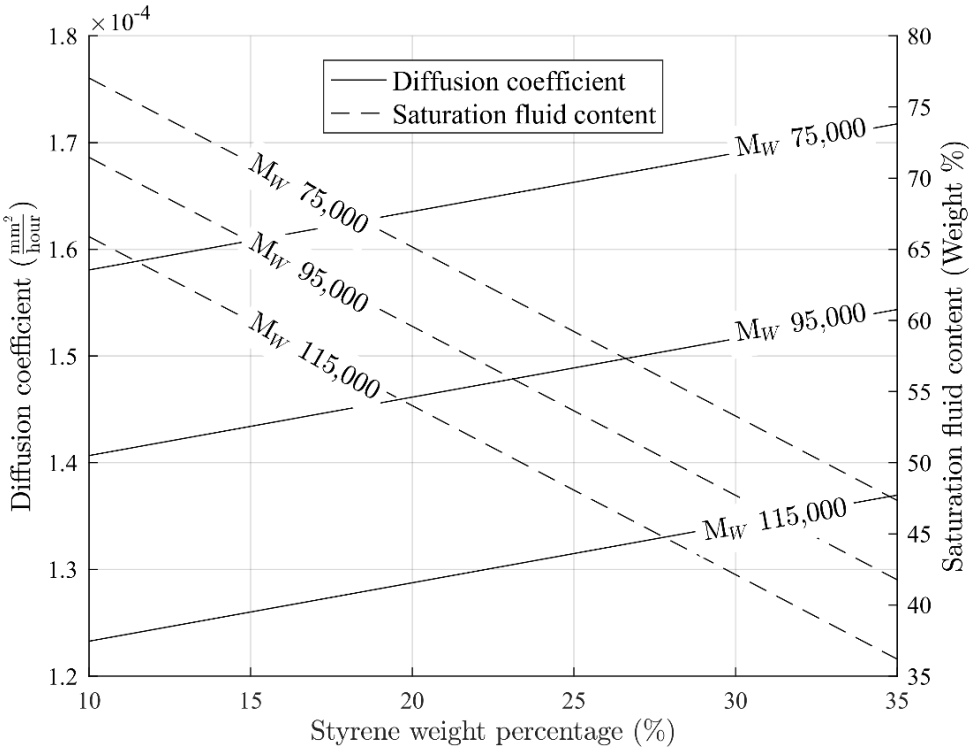

Figure 45-Expected diffusion coefficient and saturation fluid content as a function of molecular weight and styrene content for SIBS

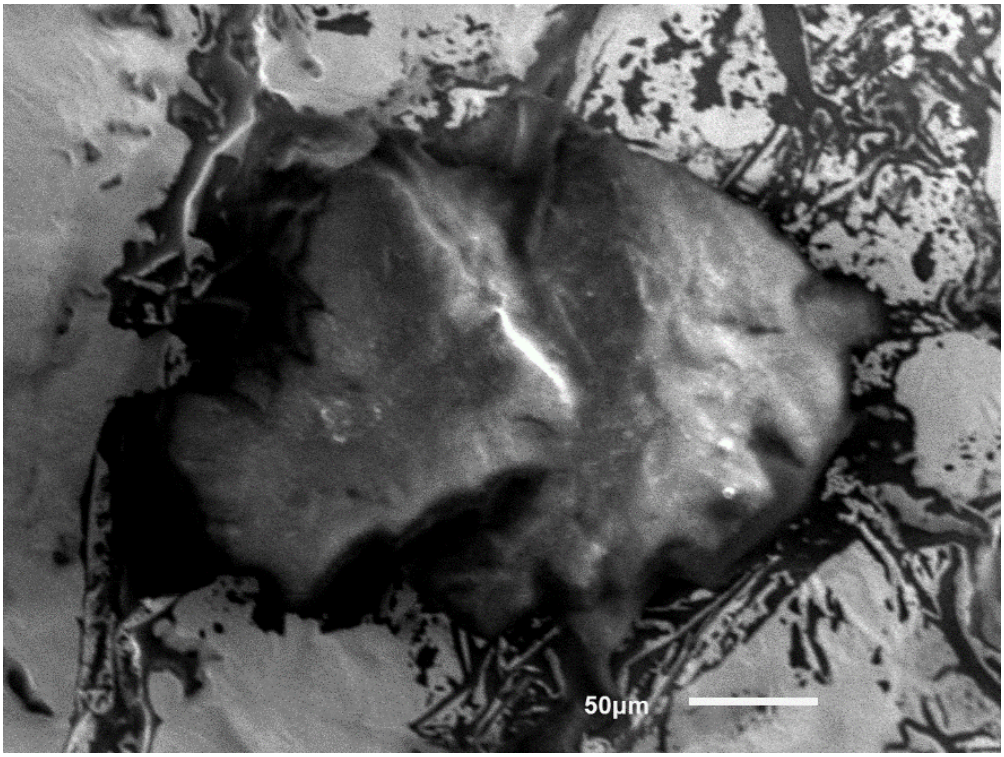

Figure 46-SEM image of a lipid blister in SIBS 73

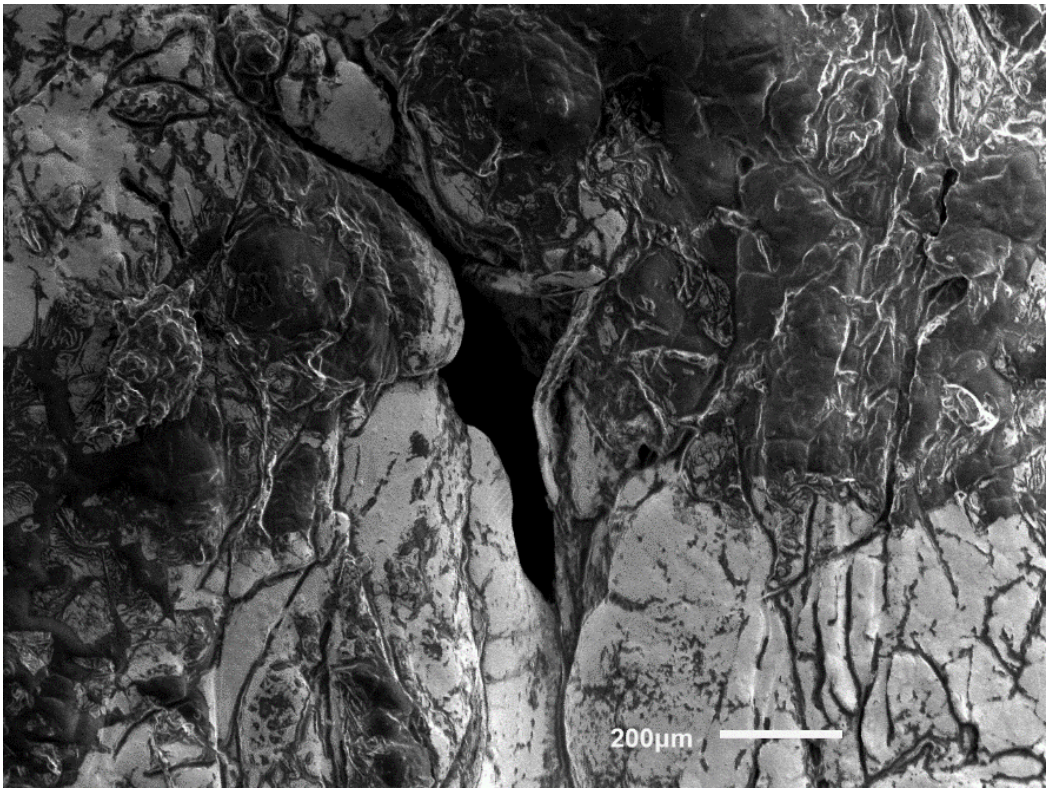

Figure 47-SEM image of a lipid induced crack in SIBS 72

SIBS 73 and 72 started diverging from the saturation lipid content, whereas 102 and 103 remained at a stable saturation level. This could be a product of relaxation or polymer breakdown, or some combination thereof. The observed drop in weight for SIBS 72 samples is most likely a product of polymer scission. Lipids could be interacting with the carbon backbone of the copolymer and breaking down segments of the polymer network that are lost during immersion. Similar phenomena was reported in poly(ethylene oxide terephthalate)/poly(butylene terephthalate) systems during immersion in phosphate buffer saline solutions [85]. The continued increase that was observed for SIBS 73 is most likely related to a plasticization phenomenon. The fatty acids absorbed could be relaxing the network, allowing individual chains to move, creating extra void space for further lipid absorption. This behavior was previously reported in various polymeric systems [52, 53].

Higher molecular SIBS possesses a more stable polymer network that is less susceptible to relaxation or scissioning, making it more desirable for implantation. It is important to note that this is the worst-case scenario for SIBS, as real *in vivo* applications would not see such a high lipid concentration environment.

Polymer swelling

Immediately following immersion in pam oil, thickness of each type of SIBS began changing rapidly due to the absorption of fatty acids. The time evolution of thickness was fitted with a single exponential equation:

$$h = \Delta h\left(1 - e^{-\frac{t}{\tau}}\right) \tag{11}$$

Where h is the percentage swelling, Δh indicates the saturation swelling percentage, and τ indicates the characteristic swelling time. A simple exponential model was selected because of its ease-of-use and because it describes the two important characteristics of swelling: rate and total thickness change. A very similar form was used by Suzuki and Hara to model swelling in hydrogels and the effects of different geometries [86]. The percentage swelling of specimen thickness as a function of immersion time is shown in Figure 48. Table 7 presents the least squares fit parameters for the different types of SIBS analyzed. Swelling appears to be mostly controlled by the soft phase, as samples with higher polystyrene content showed least swelling. This result indicates that most likely the lipid plasticization of the polymer matrix is happening in the rubber phase rather than the glassy chain segments. This conclusion is further supported by the AFM phase images that show a reduction in diameter of the styrene phase after lipid immersion and increase in cylinder/sphere separation, due to the swelling of the isobutylene phase. Note the consistent

drop in swelling for SIBS 72 once saturation was reached around 900 hours is consistent with the vertical dashed line of Figure 41 that represents the onset of rapid deterioration. Molecular weight appears to stabilize the lipid-induced plasticization, as seen in the steady swelling percentage in the saturation state for SIBS 103 and 102. The characteristic swelling times for these formulations are much lower, as constant saturation swelling is reached faster.

Table 7. Swelling exponential fit parameters

	SIBS 103T	*SIBS 102T*	*SIBS 73T*	*SIBS 72T*
Saturation swelling percentage Δh (%)	31.7	56.16	33.31	57.63
Characteristic time τ (hours)	149.3	272.9	532.6	337.2

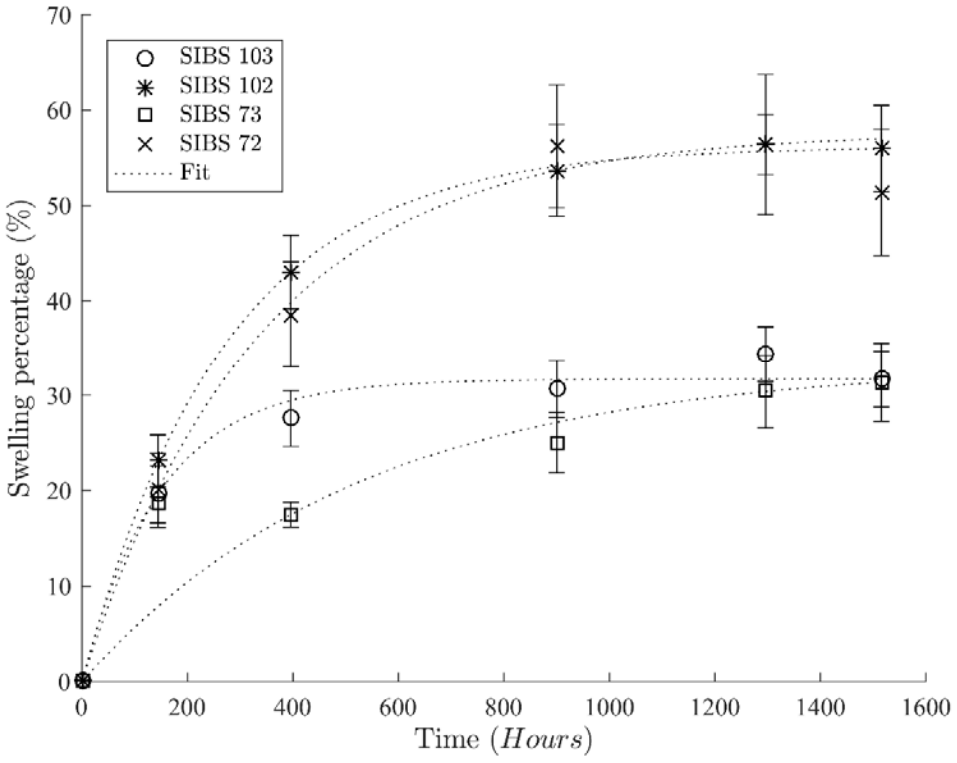

Figure 48-Percent swelling as a function of immersion time

Conclusion

Lipid uptake in four different formulations of a linear triblock copolymer (styrene isobutylene styrene, or SIBS) was studied by gravimetric immersion in palm oil. The diffusion behavior as a function of molecular weight and hard block content was used to developing an understanding of diffusion in the glassy and rubbery phases of the material. Higher molecular weight SIBS formulations exhibited lower lipid saturation content and a slower rate of diffusion, which contributed to the long-term stability and durability of the material under full immersion conditions at body temperature (37 °C). A higher content of the hard phase (polystyrene) in the block copolymer contributed to a lower lipid saturation content and less swelling during immersion, although diffusion occurred faster. This indicates that the soft segments of the polymer matrix (isobutylene) are more susceptible to plasticization compared to the hard segments. This is consistent with the visible changes observed in the specimens, as well as the phase changes observed via AFM imaging. Samples with lower hard phase content visibly deformed and showed surface cracking once saturation was reached. Furthermore, samples with higher hard phase content had much lower thickness swelling than those with low hard phase content, highlighting the importance of SIBS formulation optimization for *in vivo* applications. This study highlights the necessity of developing protocols to characterize uptake of bodily fluids in polymeric materials, and the plasticization and mechanical degradation that these absorbed fluids produce in biocompatible polymers, to fully predict performance for long-term *in vivo* applications.

Chapter 6

Previously, we have reported and characterized lipid diffusion behavior in SIBS. It was observed that lipid diffusion kinetics conform to Fickian diffusion behavior very closely. Additionally, lipids were observed to severely plasticize the isobutylene phase, leading to blistering and surface cracking. Prominent swelling was also observed for all different formulations of SIBS studied, with increased swelling in formulations with higher relative volume of isobutylene [87]. However, the underlying reason for the deleterious effect of lipids in SIBS has not yet been fully understood or modeled, and its early effects on mechanical and viscoelastic properties have not been determined. In this chapter, the mechanical and viscoelastic properties of four different formulations of SIBS are evaluated at different lipid contamination levels in order to determine the effect of lipid-induced softening and network relaxation. These results, coupled with Fourier transform infrared spectroscopy (FTIR), Gel Permeation Chromatography (GPC), and Scanning Electron Microscopy (SEM) analysis, contribute to a better understanding of the long-term performance of SIBS in lipid-rich environments and identification of potential degradation mitigation methods [88].

Materials and Methods

KANEKA Corporation provided four types of SIBS (SIBSTAR 103, 102, 73 and 72) in pellet form. Table 8 shows the composition of SIBS as determined by GPC, along with the diffusion coefficient and the saturation lipid (equilibrium) content obtained via gravimetric analysis [87]. To ensure all residual moisture was removed from the SIBS pellets, they were dried in a vacuum oven until constant weight measurements were recorded over a 12 hour interval. SIBS 102, 73, and 72 pellets were compression molded

using 8 MPa of pressure at 193 °C for 10 minutes, then folded and compressed again for another 10 minutes, and allowed to slowly cool to room temperature in order to fabricate SIBS sheets with no weld or flow lines. SIBS 103 was compressed at 220 °C because of its higher melting temperature, while all other process parameters remained the same as the other formulations. All SIBS sheets had dimensions of 300 by 300 mm and a thickness of approximately 0.5 mm. Tensile and stress relaxation specimens were cut using an arbor press and a die in accordance with ASTM D412 Type C, and dynamic creep specimens were cut using a rectangular die to prepare 6.35 by 33 mm specimens. All weights and dimensions were recorded using a high precision analytical balance and a rubber thickness gauge for consistent measurement.

Table 8. SIBS formulation and diffusion parameters

	Styrene content (wt. %)	*M_w (g/mol)*	*Diffusion coefficient (mm^2/hour)*	*Lipid saturation content (wt. %)*
SIBS 103	30	106,000	1.42×10^{-4}	44.8
SIBS 102	15	117,000	1.24×10^{-4}	59.3
SIBS 73	30	76,000	1.44×10^{-4}	54.3
SIBS 72	22	75,000	1.65×10^{-4}	62.8

Samples were immersed in glass jars filled with palm oil at 37 °C and kept in constant temperature water baths until target saturation contents were reached (5%, 10%, 15%, 20%, 30%, 40%, 60% and 80% of the lipid saturation content). Palm oil was chosen because it is mainly composed of palmitic acid, oleic acid, and linoleic acid in triglyceride form [89-91]. These triglycerides can be found in human plasma, adipose tissue, the stratum corneum, human sebum and in many other areas [68, 92-94], making it a suitable simulant of human body lipids. Lipid concentration *in vivo* is variable, and lower than the conditions described here. However, palm oil was used in its undiluted form for this first-of-its-type

analysis in order to establish a baseline, worst-case exposure condition and to isolate the effect of lipids on plasticization. After each immersion period, specimens were removed from the oil and cleaned by dabbing with oil absorbent towels. To ensure the full removal of all surface lipids, the specimens were rinsed in acetone for twenty seconds, removed and allowed to fully dry before weighing and measuring dimensional changes. Acetone was chosen because it is non-aggressive to SIBS and it is volatile, ensuring that all surface acetone was quickly evaporated.

Dumbbell specimens were tested in a universal testing frame in accordance with ASTM D412 at a rate of 500 mm/min, utilizing self-tightening roller grips to ensure all specimens would break in the narrow section. Stress relaxation experiments were performed for 16 minutes with an initial stress of 5 MPa for all types of SIBS. Rectangular specimens were fatigued for 10,000 cycles in tension using a DMA Q800 (TA Instruments®) at a stress level of 100 kPa for SIBS 72 and 102 and 250 kPa for SIBS 73 and 103. Different stress levels were used in order to accommodate the different strain levels based on relative styrene content. FTIR was performed using a PerkinElmer® Frontier instrument.

Results and Discussion

FTIR and GPC

Figure 49 shows the results of FTIR performed on all samples of uncontaminated SIBS, saturated SIBS and undiluted palm oil. Palm oil showed no broad peak corresponding to the O-H stretch at around 3300 cm^{-1} that would be present for the carboxyl group in free fatty acids. This indicates that all fatty acids are bound to glycerol forming ester bonds, which is identical to how it would be present in blood plasma. The spectra does not show any evidence of chemical interaction between the polymer specimen and the absorbed oil,

nor any chemical degradation of the polymer due to environmental aging. Further inspection reveals that the spectra of saturated SIBS appears to be a linear combination of the uncontaminated SIBS and palm oil spectra. In the region of 1800-1700 cm^{-1} a strong peak corresponding to the C=O stretch can be observed, and is attributed to the ester group in the triglycerides [95]. This peak can be observed for the palm oil spectra and the palm oil saturated sample due to the absorption of triglycerides in SIBS.

GPC was also performed for uncontaminated SIBS samples and SIBS saturated with palm oil. Results, shown in Figure 50, did not show any significant difference in molecular weight between samples before and after immersion. The elution curves consistently showed no significant difference in the molecular weight distribution of SIBS samples, regardless of type. A representative elution curve is shown for SIBS 102 in Figure 51. SIBS appears to be chemically stable and does not interact with absorbed lipids, even at full saturation concentrations. This suggests that all lipid-induced relaxation of SIBS occurs due to internal mechanical straining of the polymer and not due to scissoring and/or chemical interactions.

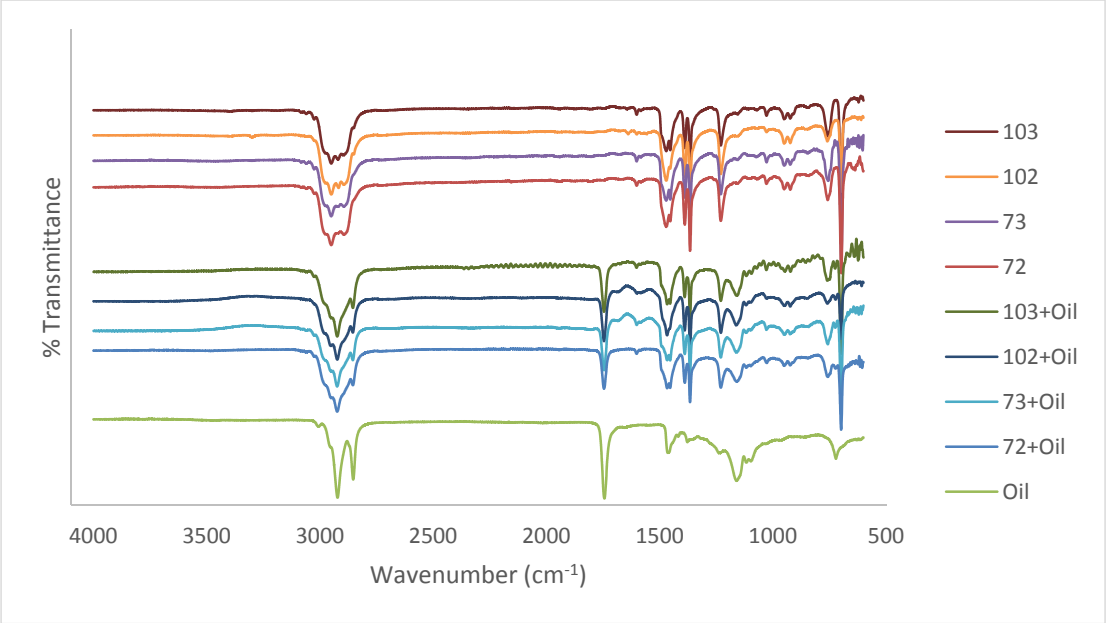

Figure 49-FTIR spectra of SIBS, saturated SIBS and palm oil. Uncontaminated SIBS samples shown on top, saturated SIBS shown in the middle and palm oil shown in the bottom. SIBS labeled according to their commercial name. Saturated samples labeled +Oil.

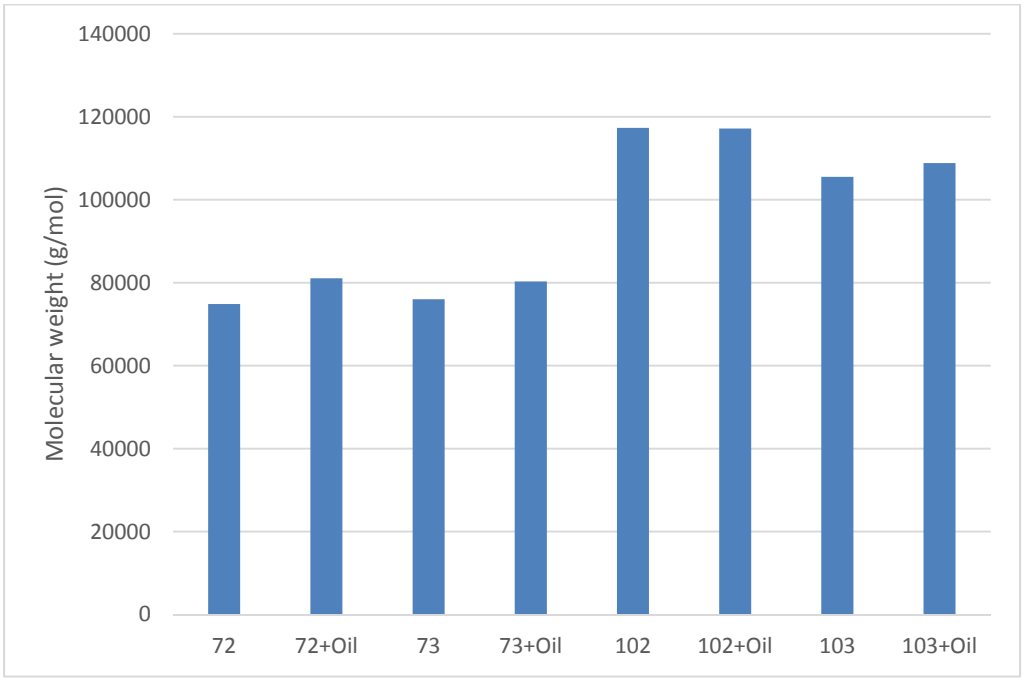

Figure 50-GPC results of SIBS and saturated SIBS.

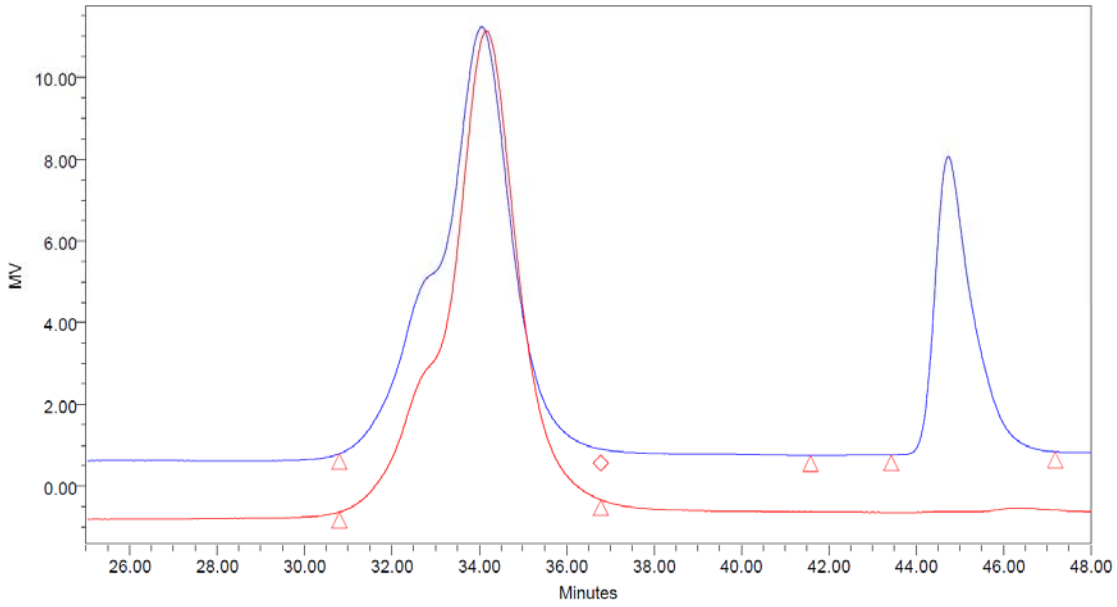

Figure 51- SIBS 102 elution curves. Top curve corresponds to contaminated samples

Tensile Testing

Dumbbell specimens of all four types of SIBS were tested in tension until failure (break). Results are shown in Figure 52 and Figure 53, with corresponding standard deviations for all sets tested. Lipid saturation percentage is relative to the equilibrium saturation condition for each type, as shown in Table 8. It is apparent from these figures that tensile strength is severely affected by the absorption of lipids and even relatively low lipid content can be very detrimental. Tensile strength appears to decrease linearly with increasing lipid content for all types tested. However, elongation at break seems to deteriorate more significantly in formulations with lower molecular weight. Lower molecular weight SIBS has a higher lipid saturation content (see Table 8) that may lead to a higher internal straining that weakens the polymer more rapidly than those compositions with higher molecular weight, which in turn leads to a shorter elongation before break and lower tensile strength. Conversely, the higher molecular weight polymer likely exhibits

higher network entanglement that contributes to higher stiffness and a reduced tendency to relax and swell. Tensile strength results together with the diffusion parameters presented here can be easily coupled in order to predict long-term mechanical behavior of SIBS *in vivo*. This analysis can provide better tools for designing biomedical devices, and can be readily adapted for different material systems or different diffusing liquids.

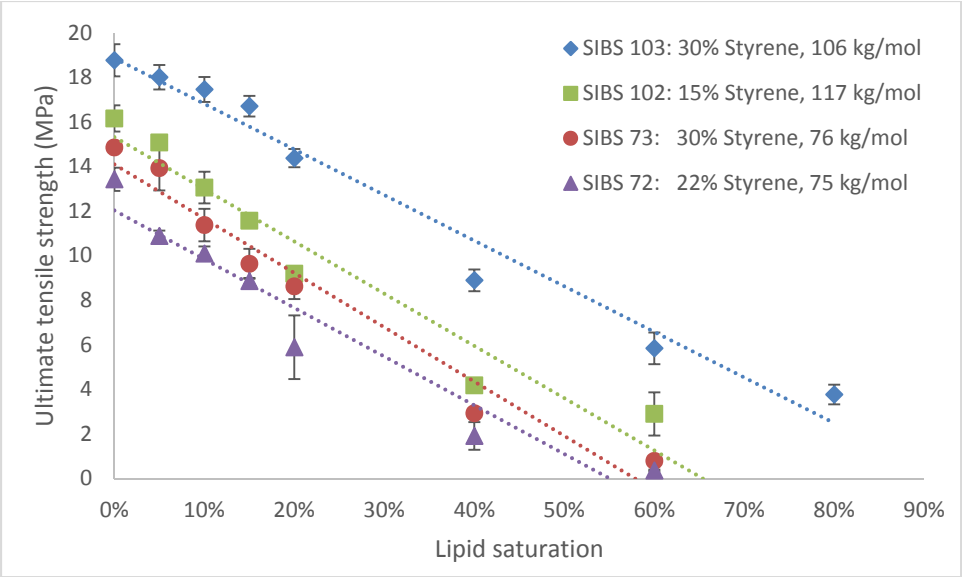

Figure 52-Ultimate tensile strength for various SIBS formulations with multiple lipid contents

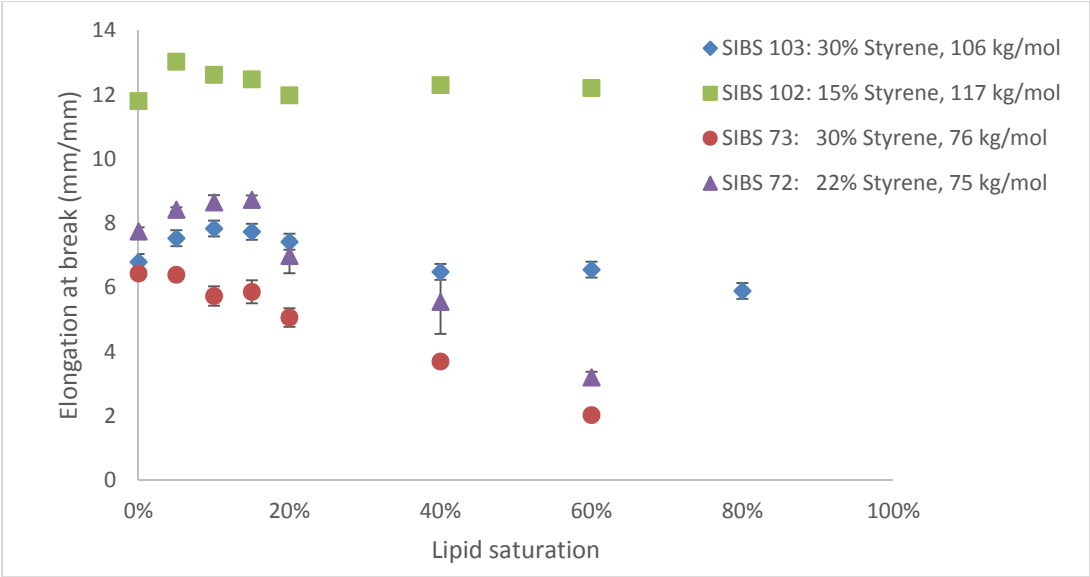

Figure 53-Elongation at break for various SIBS formulations with multiple lipid contents

Stress Relaxation

Stress relaxation response was measured for all formulations of SIBS at multiple lipid contents. Specimens were strained at 1500 mm/min up to 5 MPa and, subsequently, the strain was stopped and held constant for 16 minutes while the stress was monitored. The stress relaxation was performed for 16 minutes in order to observe the entire relaxation performance. Beyond the 16 minute mark no significant relaxation was observed. Stress relaxation was modeled using the Maxwell-Wiechert model with three spring-dashpot elements in parallel [96]. This model allows representation of different molecular segments with different relaxation times. The equation for the three spring-dashpot model is:

$$\sigma = E_\infty + \sum_{i=1}^{3} E_i e^{-t/\tau_i} \tag{12}$$

Where E_i are the tensile relaxation moduli, E_∞ is the modulus of the fully relaxed material, and τ_i are the relaxation times of the material. Figure 54 show the relaxation curves for all SIBS formulations with different lipid contents, with their respective standard deviations. As shown, the presence of lipids relaxes the polymer network even at very low lipid contents. The increase in relaxation is attributed to the plasticizing effect of lipids on the thermoplastic elastomer. In addition, the swelling of the polymer matrix due to the intrusion of lipids between polymer chains facilitates the relative movement of polymer segments, thereby increasing the stress relaxation levels. It is worth noting that the only sample at 40% saturation content that was able to reach 5 MPa was SIBS 103; all other samples showed ultimate tensile strengths lower than 5 MPa (see Figure 52). Lower styrene content samples, SIBS 72 and 102, show a much higher relaxation at very low lipid content relative to the dry state. However, continued lipid absorption results in a higher relaxation rate for

SIBS 72 than 102, likely due to the lower molecular weight of SIBS 72. The same comparison applies for SIBS 73 and 103, pointing to a better performance at higher styrene content and molecular weight due to the lower lipid affinity of styrene and the higher network stiffness.

The relaxed modulus of SIBS showed a decreasing linear relationship with increasing lipid content, as shown in Figure 55. Again, the formulations that showed lower deterioration are those with higher styrene content and higher molecular weight. Styrene acts as a physical crosslink that provides reinforcement to the polyisobutylene. The higher the crosslink density, the higher the rigidity the polymer network and its resistance to lipid intrusion that swells and relaxes the network. An increase in relaxation modulus at three relaxation times (10^{-1}, 10^{1} and 10^{2} seconds) was observed for all formulations of SIBS. However, the early relaxation modulus was more severely affected for low styrene, low molecular weight formulations. Interestingly, the relaxation times seem to be unaffected by the presence of lipids in lower styrene, lower molecular weight formulations, but a slight shift to faster relaxation was observed for the higher styrene formulations. These faster relaxation times in higher styrene formulations are in agreement with the observed higher diffusion coefficient for higher styrene SIBS formulations [87]. As lipids can move more rapidly through the styrenic phases, the onset of the polymer relaxation begins earlier. However, the isobutylene phase undergoes a more intense relaxation for longer time frames.

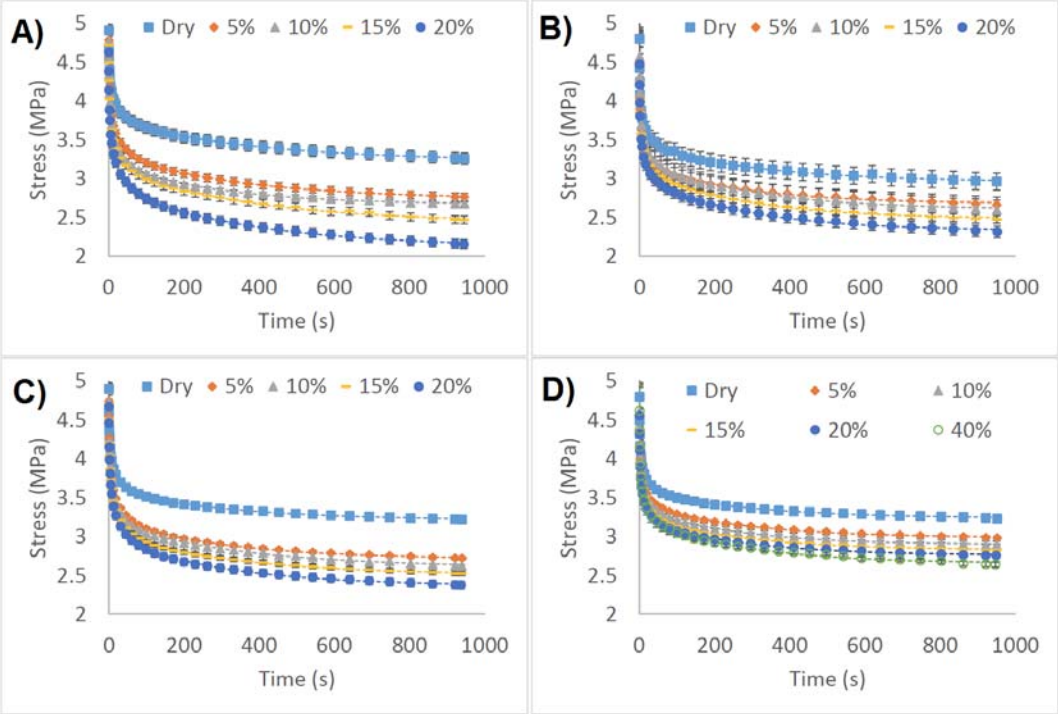

Figure 54-Stress relaxation response of A) SIBS 72, B) SIBS 73, C) SIBS 102 and D) SIBS 103. Dashed lines correspond to the model fit from equation (12)

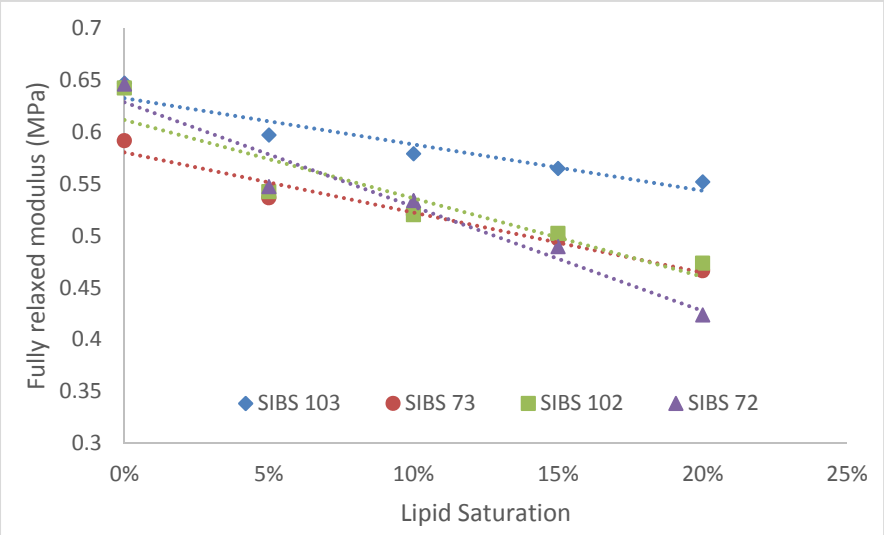

Figure 55-Relaxed modulus as a function of lipid content for four formulations of SIBS

Samples that were tested in stress relaxation mode were observed to develop multiple surface cracks. This type of surface crack was also observed for the trileaflet heart valve implanted in sheep. It was hypothesized that SIBS underwent relaxation due to the

absorption of blood lipids, which in turn promoted polymer creep and led to surface cracking [77]. Surface cracks do not develop solely due to cyclic loading, but also due to the softening of the block copolymer coupled with relaxation effects. Even at very low lipid content, the material is susceptible to relaxation and cracking. Figure 56 and Figure 57 are SEM images of the narrow section of the dumbbell specimens tested in stress relaxation mode. SEM was performed in a Jeol JSM-6010PLUS/LA and all samples were sputter coated with gold before imaging in order to avoid charging and melting the polymer. The only formulation of SIBS that did not show surface cracking or pore opening of the polymer with low lipid content was SIBS 103, which has a combination of high styrene percentage and high molecular weight (Figure 56-A). SIBS 103 displays a smooth surface, even after the 16 minute stress relaxation, and at higher magnifications no surface crack or initiation site was observed. SIBS 102 showed no surface cracking under the microscope, despite being the formulation with the lowest styrene content. Samples of SIBS 102 also showed ridges along the narrow section of the dumbbell specimens that most likely form before separation begins. Figure 56-B shows these ridges along the surface of the relaxed specimen, with no evidence of visible pores or cracks at low magnification. However, Figure 56-C shows a close up on one of "valleys" between these ridges, and the initiation of pores can be clearly seen. These pores do not exhibit the same characteristics as cracks, as they are rounded and do not have a clear tip in the propagation direction. SIBS 73 showed the same ridges observed in SIBS 102, however the pores could be observed along the ridges and even at low magnification. Figure 56-D shows a low magnification image of the ridges observed. A higher magnification image (shown in Figure 57-A), shows the pore opening along the ridges. Although these pores were more

pronounced than those observed for higher molecular weight specimens, no cracking was observed along or between pores. Lastly, SIBS 72 is shown in Figure 57-B, C, and D. Figure 57-B shows an image of the dry polymer after the stress relaxation cycle. It is very similar to the observed behavior of SIBS 103, with no discernible ridges or valleys due to stress relaxation. At higher magnifications no pore or crack initiation sites were observed for the dry polymer. For samples with 5% lipid saturation content, the low magnification image displays a very high pore density and large pore size compared to the other formulations, and even displays some cracks propagating between pores. The higher magnification image shows that all cracks propagate from the pores or ridges that are formed while undergoing relaxation, which corresponds to higher stress concentration regions. Failure started to occur and propagate through the polymer at half the stress level required for static failure, and it is very possible that continued exposure to the constant strain may lead to complete failure. This result is potentially worsened in extended, practical applications, where the softening of the polymer and subsequent pore and crack formation effectively increases the exposed surface area for diffusion, accelerating the lipid uptake and polymer plasticization. The lipid affinity displayed by SIBS is likely one of the contributors to the high biocompatibility of the material. As triglycerides are adsorbed by SIBS, the human body detects a body component instead of a foreign body object, generating no reaction. Moreover, the pore and crack formation are vital processes for the elution of drugs in coating applications. As the SIBS coating cracks, the encapsulated anti-inflammatory drug is slowly released into the bloodstream.

Analysis of the preceding results suggests that molecular weight plays a much more important role during surface cracking and softening of SIBS than styrene content. Higher

molecular weight SIBS has a reduced lipid affinity, as evidenced by its lower diffusion coefficient and saturation lipid content. The higher molecular weight SIBS might display higher polymer packing and entanglement that contributes to higher network rigidity. Consequently, less void space is available for diffusion of lipid molecules through the material, leading to delayed lipid intrusion into the polymer network and the corresponding higher resistance to polymer chain motion and relaxation. High molecular weight formulation of SIBS showed almost no deterioration of elongation capacity even at extremely high saturation contents, which indicates the stiffer polymer networks resist local chain motion and achieve the same elongation as the polymer in the dry state. This is the first documented observation of the effect of molecular weight on the lipid-induced plasticization of SIBS and could be the key to developing a SIBS-based artificial heart valve. It is also possible that hyperbranched SIBS could also display a higher resistance to lipid intrusion and relaxation due to a stiffer polymer network. Even though there is some measurable mechanical property degradation due to lipid-induced plasticization for high molecular weight SIBS, the experimental observations and trends presented here raise the possibility of mitigating plasticization by increasing the molecular weight of SIBS-based implants as much as is practical. In this manner, biocompatibility is not sacrificed and, potentially, longevity is significantly improved. However, a major drawback of using formulations with ultra high molecular weight is that processability of the thermoplastic block copolymer decreases with increasing molecular weight. This observed behavior is consistent with that seen in Figure 40 through Figure 43, and possibly related to the solubility of SIBS in palm oil. As like dissolves like, the lower molecular weight SIBS is much more affected by short chain triglycerides than higher molecular weight

formulations. Figure 50 shows slightly higher molecular weight for contaminated samples, further pushing the idea of solubility of SIBS in oil. This increase in molecular weight is due to the dissolution of lower molecular weight SIBS, effectively increasing the molecular weight of contaminated samples compared to those uncontaminated.

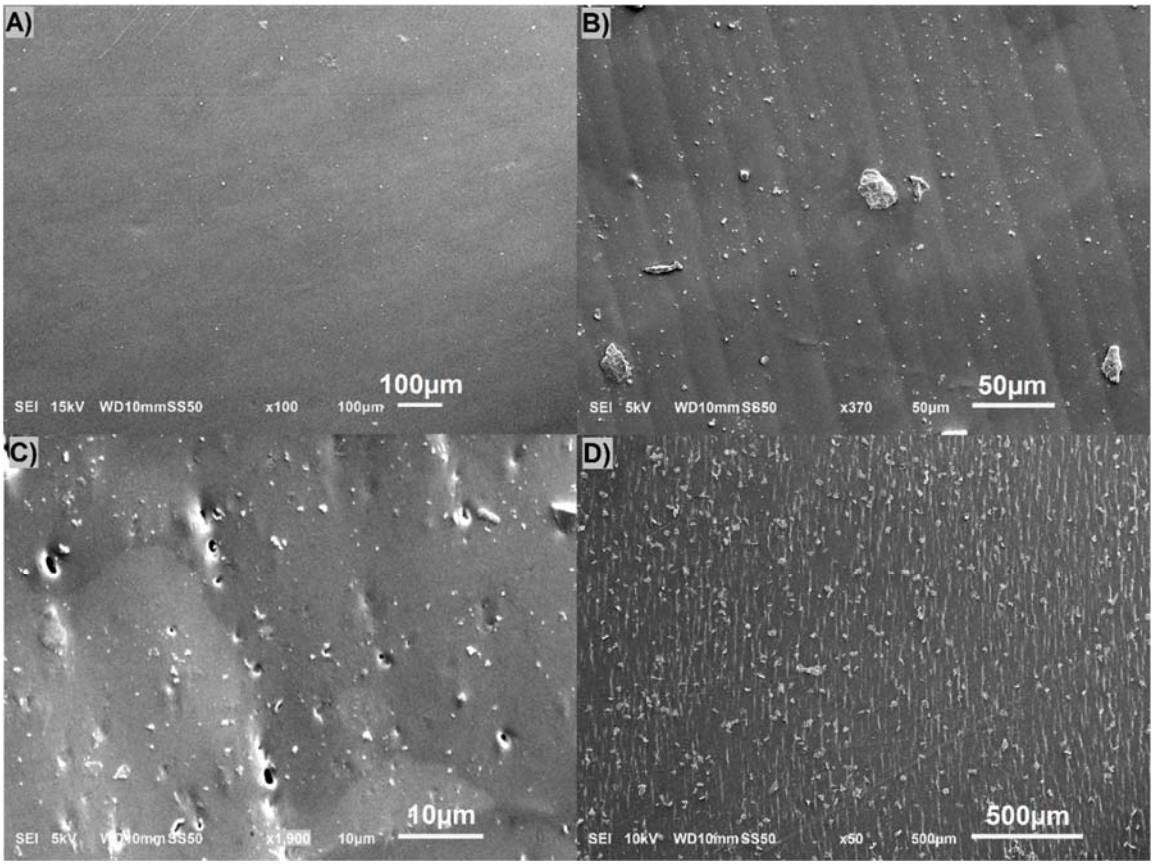

Figure 56-SEM images of different SIBS formulations at 5% lipid saturation content after stress relaxation. A) SIBS 103 at low magnification, B) SIBS 102 at medium magnification, C) SIBS 102 at high magnification and D) SIBS 73 at low magnification

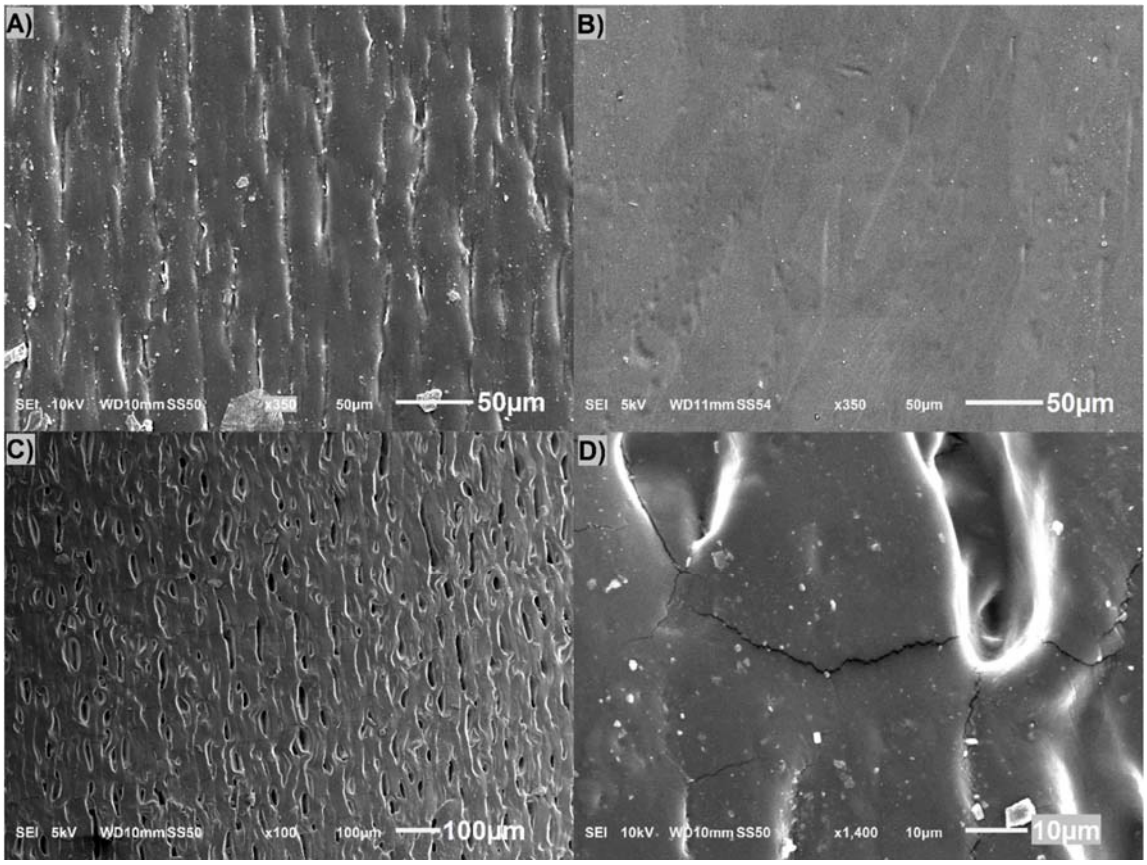

Figure 57- SEM images of different SIBS formulations after stress relaxation. A) SIBS 73 at 5% lipid saturation content, medium magnification, B) SIBS 72 uncontaminated, at medium magnification, C) SIBS 72 at 5% lipid saturation content, low magnification and D) SIBS 72 at 5% lipid saturation content, high magnification

Dynamic creep testing

Rectangular film specimens were tested in a DMA using a stress sweep method. Specimens were tested at 37 °C at a frequency of 1 Hz using a stress level of 250 kPa for SIBS 103 and 73, and 100 kPa for SIBS 102 and 72. Specimens were tested for 10,000 cycles or until failure occurred, either by cracking or by reaching the maximum displacement allowed by the DMA. Figure 58 shows the strain as a function of number of cycles for all specimens tested, and Figure 59 shows the mean increase in strain per cycle for all specimens tested. Comparing the dynamic creep cycles for SIBS 73 and 103, and SIBS 72 and 102 it can be seen that at a certain lipid content performance is severely

affected. This threshold is lower for samples with lower molecular weight. This result is in agreement with SEM observations, which showed increased pore formation for lower molecular weight specimens at very low lipid content. Pore formation during dynamic creep cycling would produce stress concentrations, thereby increasing the strain over each cycle and leading to a higher slope of the strain-cycle curves. At a threshold lipid content value or cycle number, the inter-pore region begins developing cracks that propagate through the pores, causing an abrupt increase in strain until total failure of the specimen. These results further support the idea of a higher network packing and rigidity contributing to slower lipid-induced softening and relaxation and less local chain motions that could potentially lead to overall worsened mechanical and viscoelastic performance.

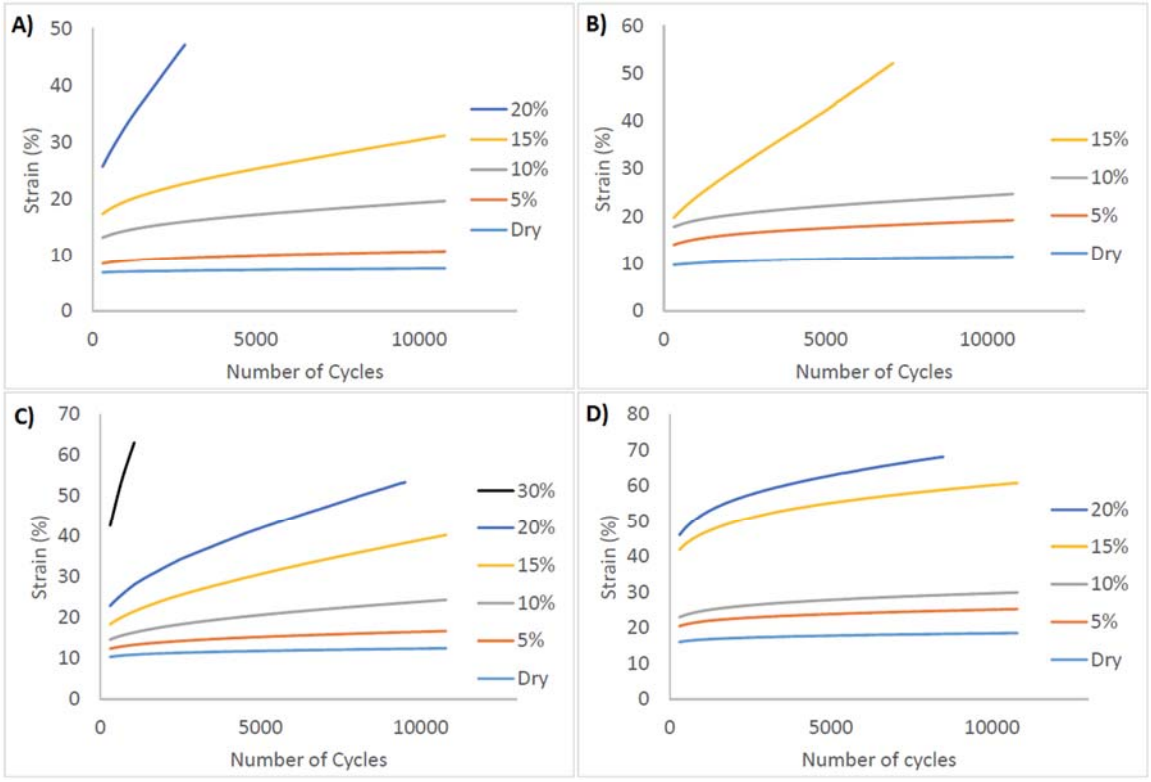

Figure 58-Dynamic creep of four different SIBS formulation at various lipid contents. A) SIBS 72, B) SIBS 73, C) SIBS 102, and D) SIBS 103

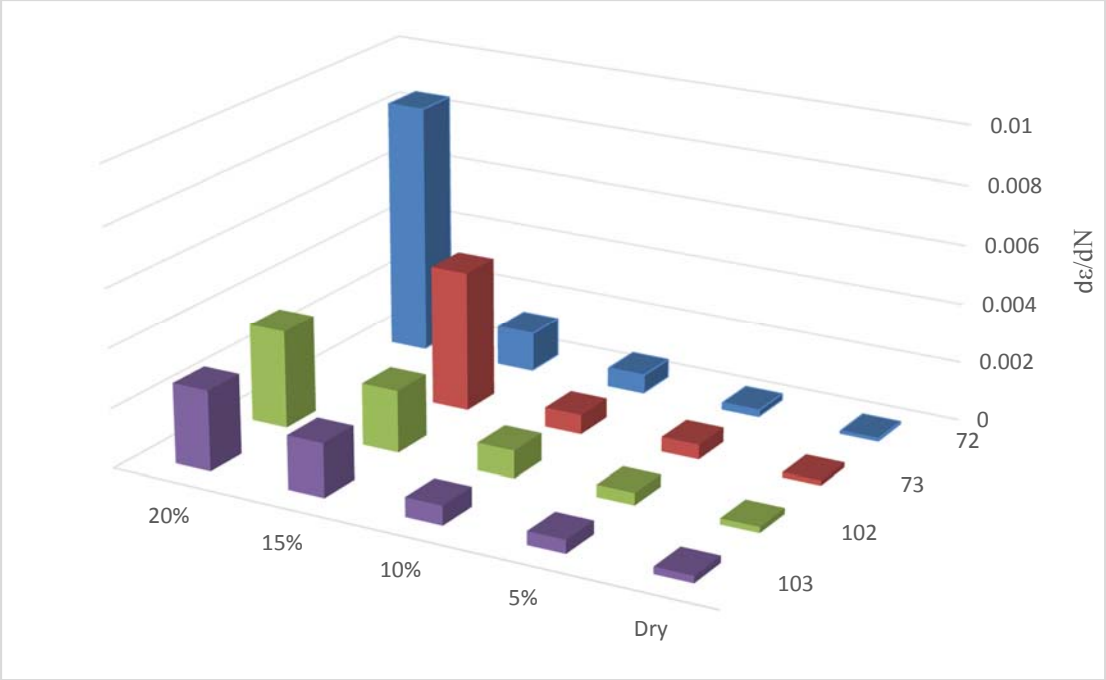

Figure 59-Mean strain increase per cycle for all samples tested

Conclusion

Lipid-induced plasticization in four commercial grades of poly(Styrene-block-Isobutylene-block-Styrene) (SIBS) biocompatible thermoplastic elastomer was analyzed. Results showed no evidence of chemical interactions between the absorbed triglycerides and SIBS; and no significant change in molecular weight of the polymer chains. This suggests that all mechanical degradation is solely due to internal straining of the polymer network as a result of lipid-induced softening and plasticizing. It was observed that the static and dynamic load carrying capacity of the four different formulations of SIBS significantly decreased with increasing lipid content. Microscopy of the specimens showed pore formation and premature failure for samples with lower molecular weight. Higher molecular weight and the associated higher network rigidity due to an increased polymer chain entanglement inhibits lipid intrusion and resists the softening effects of lipids.

The phenomena observed here is one of the most critical barriers to the development of SIBS artificial heart valves and other *in vivo* applications. Analyzing the performance of biomaterials in such complex environments is extremely difficult, costly, and time consuming. Methods to understand individual effects of interactions between biomaterials and different chemicals present in the human body have yet to be developed to the extent that long term performance of implanted biomedical devices can be accurately predicted. These dynamics can have added complexities when there are additional chemical interactions present. For its part, SIBS displays a very stable chemical structure and shows no evidence of chemical bonding with the triglycerides found in palm oil. However, the physical interactions still have to be fully understood in order to predict long term behavior during *in vivo* applications. This becomes indispensable when applications are load-bearing and need to withstand years of fatigue without creep or crack formation necessitating invasive replacement efforts. Evidence indicates that higher styrene content is beneficial. However, the optimal styrene content might vary for different applications requiring different mechanical and viscoelastic responses. Higher molecular weight SIBS is also critical for improved lipid resistance, and may be the key to unlocking the full potential of SIBS in load-bearing implants such as polymeric heart valves.

Chapter 7

In the previous chapter, lipid intrusion in SIBS has been fully characterized and reported. Lipid diffusion followed Fickian diffusion very closely in both the styrene and isobutylene domains. However, the styrene domain displayed a larger diffusion coefficient compared to the isobutylene phase. Contrariwise, the isobutylene phase showed to suffer more softening and plasticization, leading to blistering and surface cracks. Swelling was observed in all the different SIBS formulations tested, with higher swelling in lower molecular weight, and lower styrene weight percentage formulations [87]. Nevertheless, the lipid-induced relaxation mechanism has not been completely understood as of yet and the adverse effects lipids present to SIBS in terms of mechanical and viscoelastic properties have still to be studied. In this study, lipid induced relaxation in four different formulations of commercial SIBS is analyzed in order to better understand long term *in vivo* performance of SIBS. We also propose a new method to determine the coefficient of fluid-induced swelling via coupled finite element method and experimental validation that can be used with any type of non-volatile fluid. This study highlights the importance of predicting long-term performance of biocompatible materials due to the harshness of *in vivo* environments. Also, it provides a method to simulate lipid intrusion and lipid-induced swelling in SIBS, which is critical for the performance of long-term load bearing implantable devices.

Materials and Methods

Four different formulations of SIBS pellets were provided by KANEKA Corporation (SIBSTAR 72, 73, 102 and 103). The different compositions were determined by gel permeation chromatography, and the lipid diffusion coefficient, and lipid saturation content were obtained via gravimetric measurements as described [87]. Table 9 shows the

compositions and mass transport properties of all SIBS studied. Pellets were dried in a vacuum oven to ensure the removal of all residual moisture prior to fabricating specimens. Pellet weight was monitored using a high precision analytical balance, until the weight was constant over a period of 12 hours. SIBS sheets of approximately 300 mm by 300 mm by 0.5 mm were fabricated using a compression molder. Compression cycles were applied using 8 MPa pressure at 193 °C for 10 minutes, sheets were then folded and pressed again for an additional 10 minutes, and allowed to cool down slowly to room temperature. SIBS 103 pellets were pressed at 220 °C due to its higher melting temperature, but the compression cycle remained unchanged. The resulting sheets showed no visible weld lines or flow marks with consistent thickness through the entire sheet. Specimens were punched using an arbor press and an ASTM D412 TYPE C compliant die. Thicknesses and weights of all specimens were recorded using a rubber thickness gauge and an analytical balance.

Table 9. SIBS formulation and diffusion parameters

	Styrene content (wt. %)	*M_w (g/mol)*	*Diffusion coefficient (mm^2/hour)*	*Lipid saturation content (wt. %)*
SIBS 103	30	106,000	1.42×10^{-4}	44.8
SIBS 102	15	117,000	1.24×10^{-4}	59.3
SIBS 73	30	76,000	1.65×10^{-4}	62.8
SIBS 72	22	75,000	1.44×10^{-4}	54.3

Jars filled with palm oil were placed in constant temperature water baths at 37 °C and allowed to reach temperature equilibrium. Specimens were placed in the jars for multiple time periods until different lipid contents were reached (5, 10, 15, 20, 40, 60 and 80% of the total lipid saturation content). Lipid uptake simulation was performed with palm oil due to its composition being mostly palmitic acids, oleic acids and linoleic acids in triglyceride form [89, 90]. Triglycerides found in the human body are mostly composed by these acids, and can be found in blood plasma, adipose tissue and in the stratum corneum,

among others [92-94]. After sufficient immersion time, the specimens were removed from immersion in the palm oil jars and cleaned in order to remove all surface oils. The cleaning was performed by dabbing all specimens with oil absorbent cloths, and followed by rinsing in acetone for twenty seconds to ensure all surface oils were completely removed and the weights could be accurately measured. Dimensional changes were recorded once the acetone had completely evaporated. Acetone was the selected solvent because it is non-aggressive to SIBS and it is volatile at room temperature, ensuring complete evaporation of any residual surface acetone.

All tensile testing was performed in a universal testing frame with a crosshead speed of 500 mm/min. The grips utilized were self-tightening roller grips in order to minimize pinching of the dumbbell specimens. Any specimen that broke close to the grip, or at the grip, was discarded and tested again to ensure all failure would happen in the narrow section.

Results and Discussion

Modelling uniaxial tension

SIBS was modeled using an Ogden hyperelastic model fitting the uniaxial tension data [97]. The Ogden model utilizes a well-defined combination of the stretch invariants for the strain-energy function, which is shown in Equation (13):

$$\Phi(\lambda_1, \lambda_2, \lambda_3) = \sum_{n=1}^{3} \frac{\mu_n}{\alpha_n} \left(\lambda_1^{\alpha_n} + \lambda_2^{\alpha_n} + \lambda_3^{\alpha_n} - 3\right) \quad (13)$$

Where α_n and μ_n are material parameters, and $\lambda_{1,\,2,\,3}$ are the stretch invariants. The shear modulus is related to the Ogden material parameters by the following equation:

$$G = \sum_{n=1}^{3} \mu_n \alpha_n \tag{14}$$

For the case of uniaxial tension, it is possible to relate the stress to the stretch by the following relationship:

$$\sigma = \sum_{n=1}^{3} \mu_n \left(\lambda^{\alpha_n - 1} - \lambda^{-\frac{1}{2}\alpha_n - 1} \right) \tag{15}$$

Where the stretch ratio λ is defined as the ratio of deformed length to original length. All samples were fitted using a least-squared regression of Equation (15), weighing the low stretch data points heavier than the higher stretch values to ensure a better fit through the entire curve. Figure 60 through Figure 63 show the Ogden fit for all four types of SIBS. As it can be seen from the figures and the zoomed in sections, the model fits the entire data properly on the entire stretch domain.

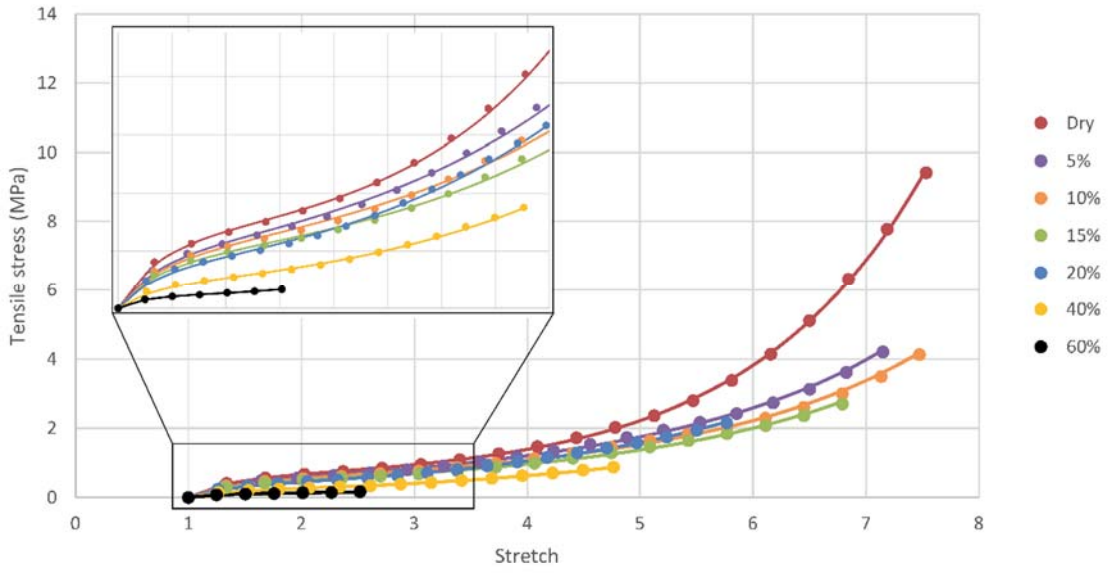

Figure 60-SIBS 72 tensile testing data with Ogden fit from Equation (15). (•) Experimental (-) Ogden fit

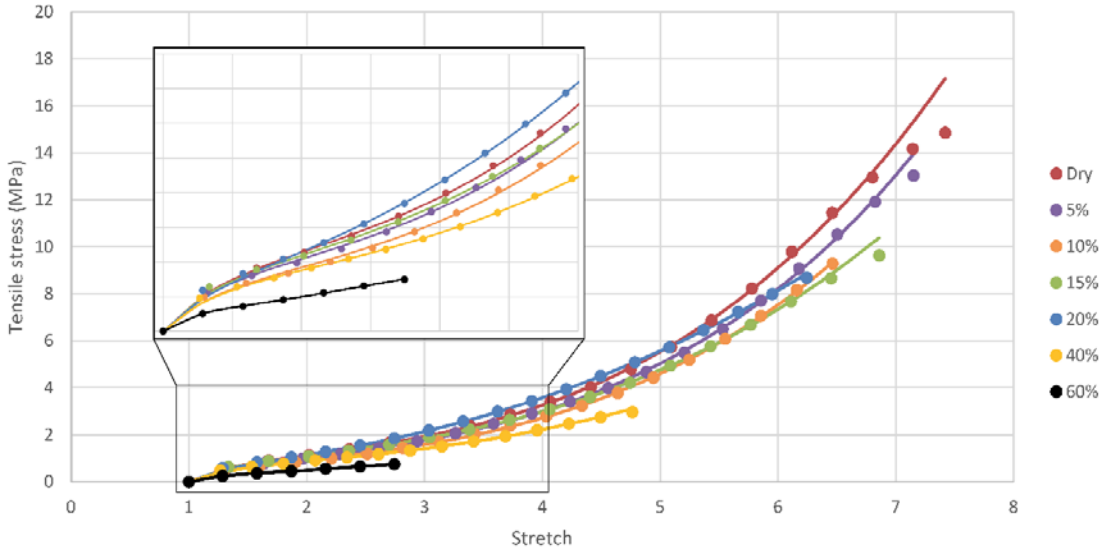

Figure 61-SIBS 73 tensile testing data with Ogden fit from Equation (15). (•) Experimental (-) Ogden fit

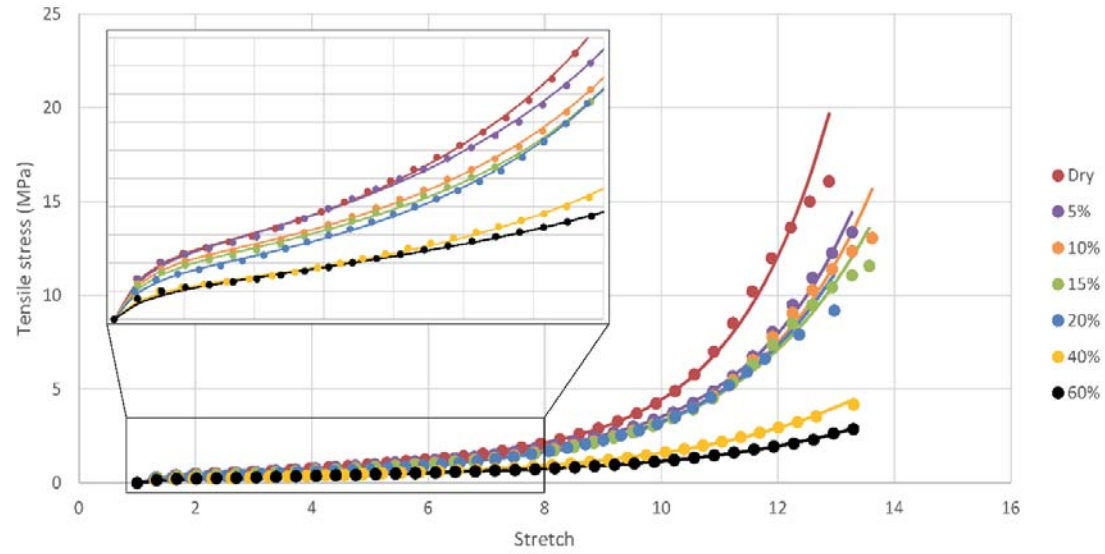

Figure 62-SIBS 102 tensile testing data with Ogden fit from Equation (15). (•) Experimental (-) Ogden fit

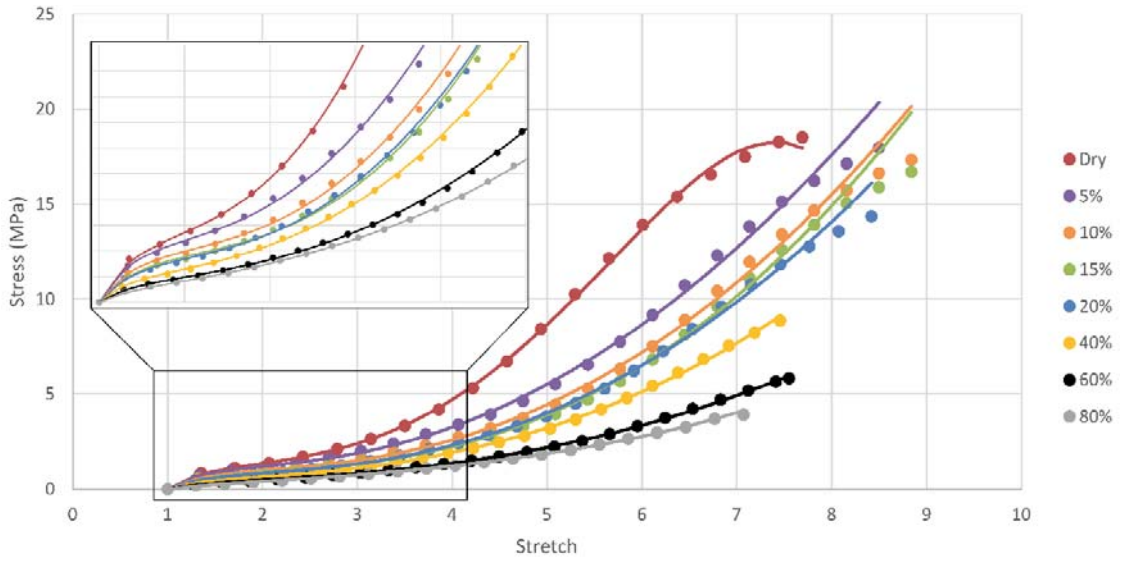

Figure 63-SIBS 103 tensile testing data with Ogden fit from Equation (15). (•) Experimental (-) Ogden fit

As observed in the figures, elongation at break is severely affected for lower molecular weight formulations at high lipid contents. The reduced elongation at break can be attributed to polymer chain slippage due to the plasticization induced by lipids. As the network softens, the polymer network becomes disentangled, allowing the polymer chains to move relative to each other, effectively reducing the load carrying capability and leading to premature failure at lower stretch values. Higher polystyrene content maintained higher tensile strength with the presence of lipids compared to lower polystyrene formulations. The polyisobutylene phase seems to be more susceptible to lipid intrusion, with higher lipid saturation contents. At extremely high lipid saturation contents, formulations with both low molecular weight and low styrene content started behaving like a gum instead of an elastomeric thermoplastic. The internal straining induced during lipid absorption severely limited the load carrying capacity of SIBS. It is important to highlight that SIBS would never reach such high saturation values, as the experimental setup uses undiluted palm oil.

This represents a worst-case scenario for SIBS, but allows for long-term performance prediction at lower saturation values, just as it would be expected *in vivo*.

With the recovered model parameters, the shear modulus was calculated for all samples tested. Shear modulus as a function of lipid content is shown in Figure 64. A clear decreasing trend was observed for the shear modulus as a function of lipid saturation. Lower styrene content samples showed a very linear reduction in shear modulus with increasing lipid content. As styrene content increases the shear modulus showed slight deviation from the linear regression, which could be attributed to a different phase morphology at higher styrene contents and the lower affinity to lipid absorption in the polystyrene phase. The shear modulus calculated from the Ogden model are comparable to similar elastomeric materials, such as natural or silicone rubbers. The recovered parameters were used to model the coupled diffusion and swelling in SIBS, in order to calculate the swelling coefficient.

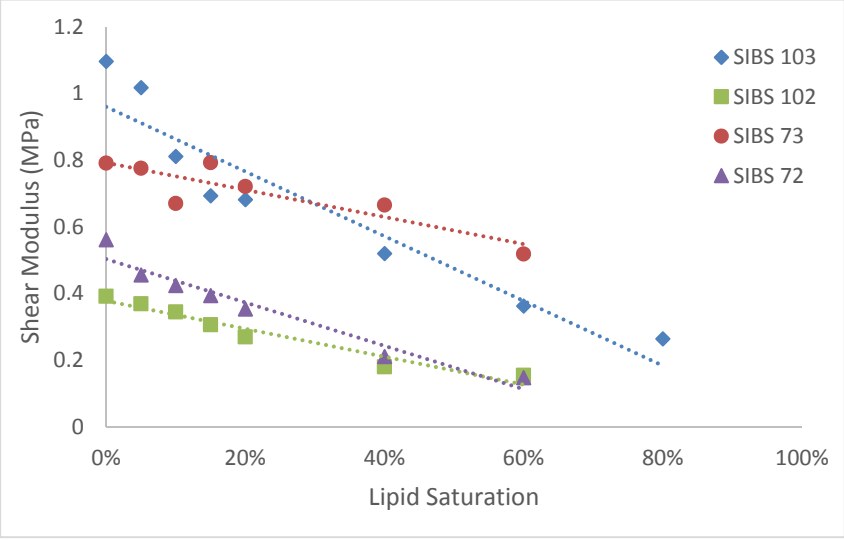

Figure 64-Shear modulus recovered from Ogden model for all SIBS tested in uniaxial tension

Coupled diffusion swelling finite element modelling

Much effort has been put into understanding the mechanics of fluid intrusion and swelling in different material systems. The most popular diffusion model is based on Fick's laws of diffusion, which has been thoroughly reported in the literature [49, 98]. The effect of fluid absorption in different materials produces internal straining that manifests as swelling in unconstrained systems [99, 100]. This effect is extremely important in polymeric materials that are prone to plasticization and relaxation effects that augment fluid-induced swelling. If the relationship between swelling and fluid concentration is linear, the coefficient of fluid swelling, β, can be defined by the following equation:

$$\beta = \frac{\epsilon}{c} \tag{16}$$

Where ϵ is the fluid-induced strain, and c is is the fluid concentration. Most methods to characterize the coefficient make use of high temperature to evaporate water at a constant rate whilst measuring changes in strain by some technique. The most common technique is by a combination of thermogravimetric analysis (TGA) and thermomechanical analysis (TMA). This technique was developed by Wong *et al.* and permits the use of standard instruments to calculate the swelling coefficient [101]. Oher methods include techniques like Moiré interferometry or digital image correlation coupled with thermal deswelling [102, 103]. These techniques can be readily used to quantify moisture induced swelling when high temperature can be applied in order to drive the moisture out of the material. When other non-volatile fluids, such as oils, are absorbed they cannot be easily removed by applying temperatures around 60~85 °C, so the thermal deswelling techniques are not applicable to a system such as SIBS and triglycerides.

Here we propose a new method to calculate the fluid-swelling coefficient by coupling diffusion measurements with finite element method. Diffusion studies were performed as described previously [87], to characterize lipid diffusion coefficient and saturation content for SIBS. The one dimensional diffusion model is based on Fick's second law of diffusion:

$$\frac{\partial c}{\partial t} = D\Delta c \tag{17}$$

Where D is the diffusion coefficient, and c is the lipid concentration.

Chester and Anand have developed a theoretical framework of the multiplicative decomposition of the deformation gradient tensor for isotropic swelling of hyperelastic materials [104]. Liu *et al.* presented a finite element algorithm to simulate the steady swelling of polymeric materials [105]. This method is based on the multiplicative decomposition of the deformation gradient tensor into elastic and swelling components:

$$\boldsymbol{F} = \boldsymbol{F_e F_s} \tag{18}$$

Where $\boldsymbol{F}_e$ is the elastic deformation tensor and $\boldsymbol{F}_s$ is the swelling deformation gradient tensor. For isotropic swelling, the swelling stretch λ_s is related to the swelling deformation gradient as follows:

$$\boldsymbol{F_s} = \lambda_s \boldsymbol{I} \tag{19}$$

Where $\boldsymbol{I}$ denotes the unit tensor. The Jacobian of the deformation gradient is defined by

$$J = \det \boldsymbol{F} = \det \boldsymbol{F_e} \det \boldsymbol{F_s} = J_e J_s \tag{20}$$

From equations (19) and (20), we have $J_s=\lambda_s^3$. Volumetric expansion can only take place due to lipid uptake, and can be described as follows:

$$J_s = 1 + \beta c \tag{21}$$

For large deformations in hyperelastic materials, such as SIBS, the Green strain $\boldsymbol{E}$ is related to the deformation gradient tensor by the following relationship:

$$\boldsymbol{E} = \frac{1}{2}(\boldsymbol{F}^T\boldsymbol{F} - \boldsymbol{I}) \tag{22}$$

And the Cauchy stress tensor is then given by:

$$\sigma = J^{-1}\boldsymbol{F}\boldsymbol{S}\boldsymbol{F}^T \tag{23}$$

Where S is the second Piola-Kirchhoff stress. Finally, the second Piola-Kirchhoff stress can be related to the strain isochoric and volumetric strain energy density function as follows:

$$\boldsymbol{S} = 2\frac{\partial W_s}{\partial \boldsymbol{C}} \tag{24}$$

$$W_s = \frac{1}{2}\kappa(J-1)^2 + \sum_{n=1}^{3}\frac{\mu_n}{\alpha_n}\left(\lambda_1^{\alpha_n} + \lambda_2^{\alpha_n} + \lambda_3^{\alpha_n} - 3\right) \tag{25}$$

Where $\boldsymbol{C}$ is the Cauchy-Green tensor, W_s is the strain energy density function, and κ is the bulk modulus. The first term in Equation (25) corresponds to the volumetric strain and the second term corresponds to the isochoric strain from the Ogden model. The recovered Ogden parameters were used for the coupled diffusion swelling simulation.

The first step was to perform a diffusion simulation to validate the mass transport model with the measured experimental data. All experimental data was one dimensional, so the finite element simulation only modeled one dimensional diffusion. The boundary condition

at the surface of the model corresponded to full immersion in palm oil, the initial condition corresponded to the dry state (zero saturation) inside the boundary of the model, and the simulation was allowed to run until full saturation was reached. The simulation results showed excellent agreement with the experimental measurements. The results of the diffusion simulation are shown in Figure 65. As explained in the previous chapter, the drop observed for SIBS 72 is due to the lipid induced plasticization and degradation. Specimens of low styrene, low molecular weight formulation are the most affected by lipid intrusion, and tend to develop higher internal straining that leads to pore formation and subsequent cracking. As saturation is reached, the internal straining cannot be sustained and the material starts to degrade, becoming extremely frail and breaking down. After the removal from palm oil, the samples have to be cleaned and rinsed, which leads to mass loss due to the fragility of highly saturated SIBS 72. More details on the experimental setup and the effect of lipid absorption in SIBS can be found in our previous work [87].

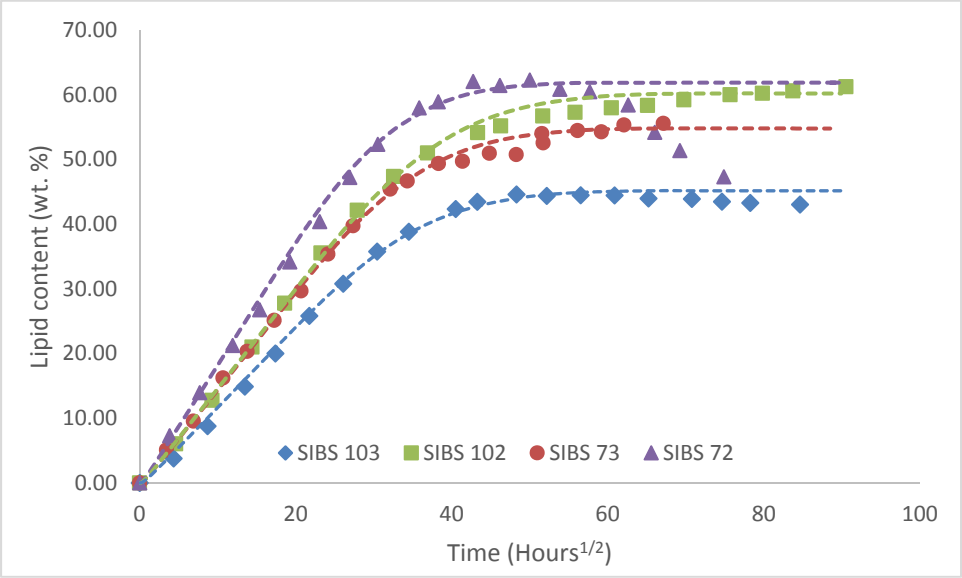

Figure 65-Lipid uptake of four SIBS formulations. Markers indicate experimental results and dashed lines indicate FEM simulation results

Similarly, a virtual tensile test was performed to calibrate the finite element model using the recovered Ogden strain energy density function. A two-dimensional rectangular specimen was modeled using plane strain with a nearly incompressible approximation (bulk modulus three orders of magnitude larger than shear modulus). A boundary was displaced up to different stretch levels, while two adjacent boundaries were assigned roller constraints and the remaining boundary was allowed to translate freely. All specimens were tested using their corresponding Ogden material parameters and compared to the experimental measurements. Simulation results from uncontaminated cases are shown in Figure 66 with the corresponding experimental measurements and the theoretical result calculated from Equation (13). As it can be seen from the figure, FEM result are in very close agreement to experimental and theoretical results.

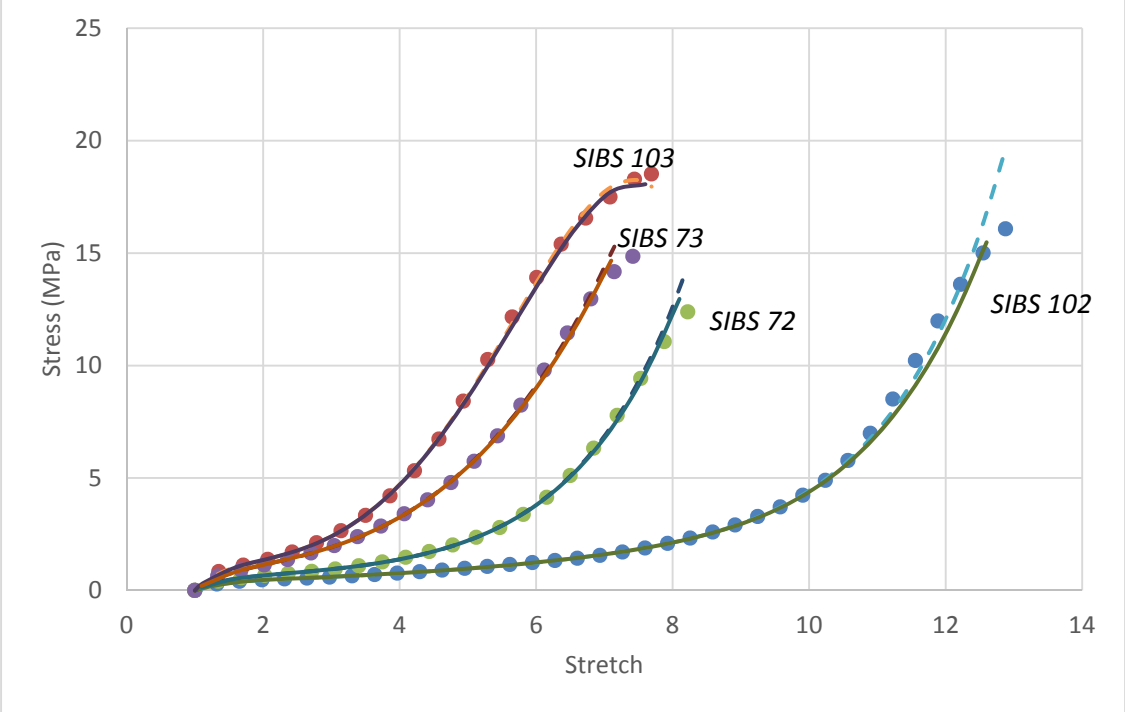

Figure 66-Comparison of virtual testing with experimental and theoretical results. Marker indicates experimental results, dashed lines indicate virtual testing result and lines indicate theoretical results

Once all the diffusion parameters and hyperelastic material parameters were calibrated, the fluid induced swelling was coupled by combining the hyperelastic material method with the diffusion simulation. The material model parameters were updated once the elements reached a lipid saturation content of 5, 10, 15, 20, 40 and 60%, based on Figure 60-Figure 63. Each element was updated individually based on its concentration value, so different elements could have different material parameters. This represents the lipid softening and plasticization more closely compared to adjusting the material parameters for all elements simultaneously at given immersion times. The four different formulations of SIBS were simulated to determine their individual swelling coefficients. In order to do so, multiple simulations were run at different swelling coefficient values while the sample thickness was monitored. The final swelling coefficient was determined by minimizing the mean squared error between the simulation results and the experimental measurements. Figure 67 shows the updated lipid uptake curves for all formulations of SIBS with hyperelastic material parameters and swelling. All the curves show some deviation from the experimental measurements once the lipid content starts to level off, as saturation is reached. This was not observed in Figure 65, for the simulation without the fluid swelling component. The broader leveling-off could be related to the increase in distance, due to swelling, that lipids have to diffuse in order to reach full saturation of the specimen, delaying the time to reach saturation.

Figure 68 shows the thickness swelling resulting from the lipid intrusion. The swelling effect is more pronounced in compositions with lower styrene content, as styrene is less susceptible to lipid plasticization and acts as a physical crosslink providing structural rigidity to the network. Swelling was 31%, 32%, 51% and 54% for SIBS 73, 103, 72, 102

respectively, which corresponds to higher swelling for lower styrene content samples. It can also be noted that SIBS 72 and 102 displayed a slower swelling rate than what was predicted by the finite element simulation. This might be attributed to a viscoelastic swelling response from the lower styrene formulations. There might be some swelling creep effects that keep straining the polymer for longer periods of time. This would not be captured by the simulation as all strain was modeled elastically with no viscoelasticity effects taken into consideration. Higher styrene formulations might display some level of swelling creep, however it would not be as noticeable as the other formulations because of the improved creep performance of styrene. Figure 69 shows the concentration profile for SIBS 73 at different immersion times until full saturation is reached. The concentration profile is plotted on the swelled shape of the specimen, showing a noticeable difference between the dry and saturated states. The calculated swelling coefficients for SIBS 103, 73, 102 and 72 are shown in Table 10. It can be seen from the recovered swelling coefficient that higher styrene content and higher molecular weight formulations have a higher resistance to lipid-induced swelling. This is attributed to the lower lipid affinity showed by the styrene phase, and the higher polymer entanglement density showed by higher molecular weight that resist lipid-intrusion and network swelling. This method allows for the calculation of the swelling coefficient for fluids that are non-volatile and would not be possible to measure using a combination of TGA and TMA. Moreover, this complete characterization of the material allows simulation of the mechanical performance in lipid-rich environments in which the absorption of lipids could significantly deteriorate the material, providing a great tool for designers to better predict long-term performance of implantable devices.

Table 10. Calculated SIBS swelling coefficient

	SIBS 103	*SIBS 73*	*SIBS 102*	*SIBS 72*
Swelling Coefficient (m^3/kg)	2.2×10^{-4}	2.4×10^{-4}	2.6×10^{-4}	2.7×10^{-4}

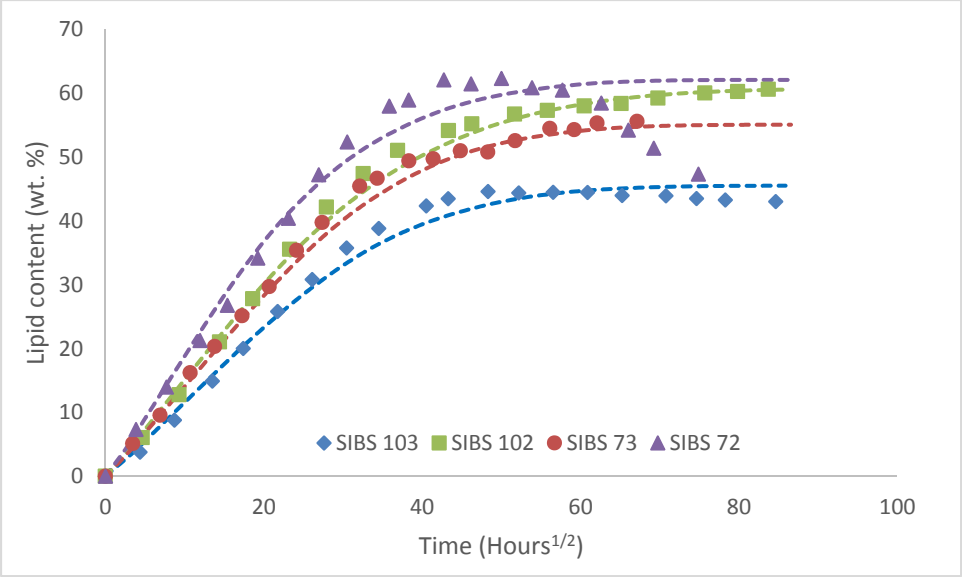

Figure 67-Lipid uptake of four SIBS formulations. Markers indicate experimental measurements and dashed lines indicate FEM simulation results

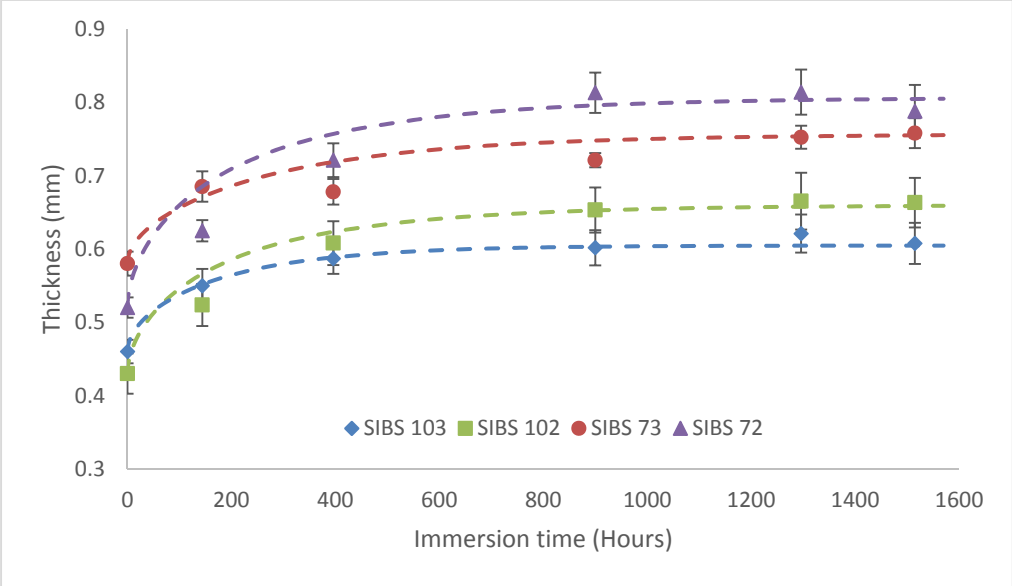

Figure 68-Thickness swelling of four SIBS formulations. Markers indicate experimental measurements and dashed lines indicate simulation results from FEM

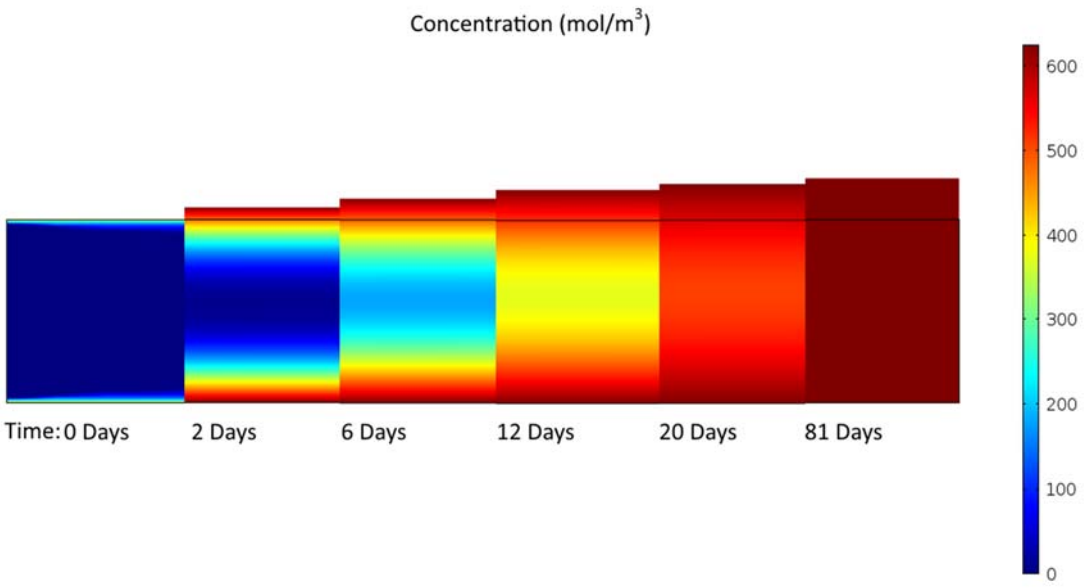

Figure 69-Lipid concentration profile and swelling for SIBS 73 at different immersion times

Conclusion

Lipid induced relaxation in four commercial grades of a biocompatible thermoplastic elastomer was analyzed. Poly(Styrene-block-Isobutylene-block-Styrene) (SIBS) copolymer was immersed up to different lipid saturation contents and tested in uniaxial tension. An Ogden hyperelastic material model was used to model all formulations tested. All SIBS displayed a reduction in tensile strength with increasing lipid content. Elongation at break showed to be negatively affected by lipid intrusion in low molecular weight formulations, however in high molecular weight formulations it did not appear to be affected. This points to a softening of the polymer due to the lipid absorption that leads to a plasticization of the polymer network. Higher molecular weight showed higher network rigidity and better resistance to local chain motion, thus elongation at break remained constant with lipid intrusion. A coupled swelling diffusion simulation was performed in order to characterize the swelling coefficient of SIBS. Due to the non-volatility of lipids, commonly used thermal methods cannot be performed to measure the swelling coefficient.

A combination of experimental measurements and finite element simulations was used to characterize SIBS. A simple diffusion model based on Fick's second law, and the Ogden strain energy density function were coupled in order to recover the swelling coefficient. The simulation results matched very closely with the experimental measurements, allowing to recover the swelling coefficient of SIBS. This technique can be easily applied to different materials systems and non-volatile liquids to recover mass transport properties. The recovered properties can be used to more accurately model and simulate *in vivo* plasticization of biocompatible materials, allowing for better prediction of long term implant performance.

References

[1] B. Shrestha, R. Goveas, S. Thaworanunta, Rapid Fabrication of Silicone Orbital Prosthesis Using Conventional Methods, Singapore Dental Journal 35 (2014) 83-6.

[2] A. Visser, G.M. Raghoebar, R.P. van Oort, A. Vissink, Fate of implant-retained craniofacial prostheses: life span and aftercare, The International journal of oral & maxillofacial implants 23(1) (2008) 89-98.

[3] S. Karakoca, C. Aydin, H. Yilmaz, B.T. Bal, Retrospective Study of Treatment Outcomes with Implant-Retained Extraoral Prostheses: Survival Rates and Prosthetic Complications, The Journal of Prosthetic Dentistry 103(2) (2010) 118-126.

[4] S. Karakoca-nemli, C. Aydin, H. Yilmaz, B.T. Bal, A Method for Fabricating an Implant-Retained Orbital Prosthesis Using the Existing Prosthesis, Journal of Prosthodontics 20(7) (2011) 583-586.

[5] J.C. Markt, J.C. Lemon, Extraoral Maxillofacial Prosthetic Rehabilitation at the M. D. Anderson Cancer Center: A Survey of Patient Attitudes and Opinions, The Journal of Prosthetic Dentistry 85(6) (2001) 608-613.

[6] N. Ariani, A. Visser, R.P. van Oort, L. Kusdhany, T.B.W. Rahardjo, B.P. Krom, H.C. van Der Mei, A. Vissink, Current State of Craniofacial Prosthetic Rehabilitation, The International Journal of Prosthodontics 26(1) (2013) 57.

[7] F. Yoshioka, S. Ozawa, S. Okazaki, Y. Tanaka, Fabrication of an Orbital Prosthesis Using a Noncontact Three-Dimensional Digitizer and Rapid-Prototyping System, Journal of Prosthodontics 19(8) (2010) 598-600.

[8] S. Li, C. Xiao, L. Duan, C. Fang, Y. Huang, L. Wang, CT Image-Based Computer-Aided System for Orbital Prosthesis Rehabilitation, Medical & Biological Engineering & Computing 53(10) (2015) 943-950.

[9] S. Jin, X. Yaoyang, C. Xiaobo, X. Juntong, Imperfect Symmetry Transform for Orbital Prosthesis Modelling, Rapid Prototyping Journal 19(3) (2013) 180-188.

[10] Y. Bi, S. Wu, Y. Zhao, S. Bai, A New Method for Fabricating Orbital Prosthesis with a CAD/CAM Negative Mold, The Journal of Prosthetic Dentistry 110(5) (2013) 424-428.

[11] L. Pinchuk, G.J. Wilson, J.J. Barry, R.T. Schoephoerster, J.M. Parel, J.P. Kennedy, Medical Applications of Poly(Styrene-Block-Isobutylene-Block-Styrene) ("SIBS"), Biomaterials 29(4) (2008) 448-60.

[12] M. Boden, R. Richard, M.C. Schwarz, S. Kangas, B. Huibregtse, J.J. Barry, In vitro and in vivo evaluation of the safety and stability of the TAXUS Paclitaxel-Eluting Coronary Stent, Journal of Material Science: Materials in Medicine 20(7) (2009) 1553-62.

[13] F. Strickler, R. Richard, S. McFadden, J. Lindquist, M.C. Schwarz, R. Faust, G.J. Wilson, M. Boden, In Vivo and in Vitro Characterization of Poly(Styrene-B-Isobutylene-B-Styrene) Copolymer Stent Coatings for Biostability, Vascular Compatibility and Mechanical Integrity, Journal of biomedical materials research. Part A 92(2) (2010) 773-82.

[14] M. El Fray, P. Prowans, J.E. Puskas, V. Altstadt, Biocompatibility and Fatigue Properties of Polystyrene-Polyisobutylene-Polystyrene, an Emerging Thermoplastic Elastomeric Biomaterial, Biomacromolecules 7(3) (2006) 844-50.

[15] K.R. Kamath, J.J. Barry, K.M. Miller, The Taxus Drug-Eluting Stent: A New Paradigm in Controlled Drug Delivery, Advanced drug delivery reviews 58(3) (2006) 412-36.

[16] J.Z. Zhu, X.W. Xiong, R. Du, Y.J. Jing, Y. Ying, X.M. Fan, T.Q. Zhu, R.Y. Zhang, Hemocompatibility of Drug-Eluting Coronary Stents Coated with Sulfonated Poly (Styrene-Block-Isobutylene-Block-Styrene), Biomaterials 33(33) (2012) 8204-12.

[17] Z. Jaffery, A. Prasad, J.H. Lee, C.J. White, Drug- Eluting Coronary Stents - Focus on Improved Patient Outcomes, Patient Related Outcome Measures 2 (2011) 161.

[18] P. Antony, Y. Kwon, J.E. Puskas, M. Kovar, P.R. Norton, Atomic Force Microscopic Studies of Novel Arborescent Block and Linear Triblock Polystyrene–Polyisobutylene Copolymers, European Polymer Journal 40(1) (2004) 149-157.

[19] D.M. Crawford, E. Napadensky, N.C. Beck Tan, D.A. Reuschle, D.A. Mountz, K.A. Mauritz, K.S. Laverdure, S.P. Gido, W. Liu, B. Hsiao, Structure/Property Relationships in Polystyrene–Polyisobutylene–Polystyrene Block Copolymers, Thermochimica Acta 367-368 (2001) 125-134.

[20] R.F. Storey, B.J. Chisholm, M.A. Masse, Morphology and Physical Properties of Poly(Styrene-B-Isobutylene-B-Styrene) Block Copolymers, Polymer 37(14) (1996) 2925-2938.

[21] T. Kwee, S.J. Taylor, K.A. Mauritz, R.F. Storey, Morphology and Mechanical and Dynamic Mechanical Properties of Linear and Star Poly(Styrene-B-Isobutylene-B-Styrene) Block Copolymers, Polymer 46(12) (2005) 4480-4491.

[22] S. St. Lawrence, D.M. Shinozaki, M. Gerchcovich, U. Myler, J.E. Puskas, G. Kaszas, Micromechanical Testing of Polyisobutylene—Polystyrene Block-Type Thermoplastic Elastomers, Rubber Chemistry and Technology 74(4) (2001) 601-613.

[23] G. Kaszas, J.E. Puskas, J.P. Kennedy, W.G. Hager, Polyisobutylene-Containing Block Polymers by Sequential Monomer Addition. Ii. Polystyrene–Polyisobutylene–Polystyrene Triblock Polymers: Synthesis, Characterization, and Physical Properties, Journal of Polymer Science Part A: Polymer Chemistry 29(3) (1991) 427-435.

[24] J.E. Puskas, G. Kaszas, J.P. Kennedy, W.G. Hager, Polyisobutylene-Containing Block Polymers by Sequential Monomer Addition. Iv. New Triblock Thermoplastic Elastomers Comprising High Tg Styrenic Glassy Segments: Synthesis, Characterization and Physical Properties, Journal of Polymer Science Part A: Polymer Chemistry 30(1) (1992) 41-48.

[25] J.E. Puskas, P. Antony, M. El Fray, V. Altstädt, The Effect of Hard and Soft Segment Composition and Molecular Architecture on the Morphology and Mechanical Properties of Polystyrene–Polyisobutylene Thermoplastic Elastomeric Block Copolymers, European Polymer Journal 39(10) (2003) 2041-2049.

[26] M. Fittipaldi, L.A. Rodriguez, A. Damley-Strnad, L.R. Grace, Improving Tensile Strength of an Injection-Molded Biocompatible Thermoplastic Elastomer, Materials & Design 86 (2015) 6-13.

[27] E.A. Foreman, J.E. Puskas, G. Kaszas, Synthesis and Characterization of Arborescent (Hyperbranched) Polyisobutylenes from the 4-(1,2-Oxirane-Isopropyl)Styrene Inimer, J Polym Sci Pol Chem 45(24) (2007) 5847-5856.

[28] J.E. Puskas, Y. Kwon, P. Antony, A.K. Bhowmick, Synthesis and Characterization of Novel Dendritic (Arborescent, Hyperbranched) Polyisobutylene-Polystyrene Block Copolymers, J Polym Sci Pol Chem 43(9) (2005) 1811-1826.

[29] J.E. Puskas, E.A. Foreman-Orlowski, G.T. Lim, S.E. Porosky, M.M. Evancho-Chapman, S.P. Schmidt, M. El Fray, M. Piatek, P. Prowans, K. Lovejoy, A Nanostructured Carbon-Reinforced Polyisobutylene-Based Thermoplastic Elastomer, Biomaterials 31(9) (2010) 2477-88.

[30] K.J. Gilmore, S.E. Moulton, G.G. Wallace, Incorporation of Carbon Nanotubes into the Biomedical Polymer Poly(Styrene-B-Isobutylene-B-Styrene), Carbon 45(2) (2007) 402-410.

[31] L. Pinchuk, I. Riss, J.F. Batlle, Y.P. Kato, J.B. Martin, E. Arrieta, P. Palmberg, R.K. Parrish, B.A. Weber, Y. Kwon, J.-M. Parel, The Use of Poly(Styrene-Block-Isobutylene-Block-Styrene) as a Microshunt to Treat Glaucoma, Regenerative Biomaterials 3(2) (2016) 137.

[32] G. Teck Lim, S.A. Valente, C.R. Hart-Spicer, M.M. Evancho-Chapman, J.E. Puskas, W.I. Horne, S.P. Schmidt, New Biomaterial as a Promising Alternative to Silicone Breast Implants, Journal of the Mechanical Behavior of Biomedical Materials 21 (2013) 47-56.

[33] X.P. Dang, General Frameworks for Optimization of Plastic Injection Molding Process Parameters, Simul Model Pract Th 41 (2014) 15-27.

[34] B. Ozcelik, A. Ozbay, E. Demirbas, Influence of Injection Parameters and Mold Materials on Mechanical Properties of Abs in Plastic Injection Molding, Int Commun Heat Mass 37(9) (2010) 1359-1365.

[35] W.C. Chen, M.W. Wang, C.T. Chen, G.L. Fu, An Integrated Parameter Optimization System for Miso Plastic Injection Molding, The International Journal of Advanced Manufacturing Technology 44(5-6) (2008) 501-511.

[36] H. Shi, Y. Gao, X. Wang, Optimization of Injection Molding Process Parameters Using Integrated Artificial Neural Network Model and Expected Improvement Function Method, The International Journal of Advanced Manufacturing Technology 48(9-12) (2009) 955-962.

[37] H. Oktem, T. Erzurumlu, I. Uzman, Application of Taguchi Optimization Technique in Determining Plastic Injection Molding Process Parameters for a Thin-Shell Part, Materials & Design 28(4) (2007) 1271-1278.

[38] M.T. Chuang, Y.K. Yang, Y.H. Hsiao, Modeling and Optimization of Injection Molding Process Parameters for Thin-Shell Plastic Parts, Polym-Plast Technol 48(7) (2009) 745-753.

[39] W.J. Deng, C.T. Chen, C.H. Sun, W.C. Chen, C.P. Chen, An Effective Approach for Process Parameter Optimization in Injection Molding of Plastic Housing Components, Polym-Plast Technol 47(9) (2008) 910-919.

[40] N.M. Mehat, S. Kamaruddin, Multi-Response Optimization of Injection Moulding Processing Parameters Using the Taguchi Method, Polym-Plast Technol 50(15) (2011) 1519-1526.

[41] P. Zhao, H. Zhou, Y. Li, D. Li, Process Parameters Optimization of Injection Molding Using a Fast Strip Analysis as a Surrogate Model, The International Journal of Advanced Manufacturing Technology 49(9-12) (2009) 949-959.

[42] C.Y. Shen, L.X. Wang, Q. Li, Optimization of Injection Molding Process Parameters Using Combination of Artificial Neural Network and Genetic Algorithm Method, J Mater Process Tech 183(2-3) (2007) 412-418.

[43] S. Mamaghani Shishavan, T. Azdast, S. Rash Ahmadi, Investigation of the Effect of Nanoclay and Processing Parameters on the Tensile Strength and Hardness of Injection Molded Acrylonitrile Butadiene Styrene–Organoclay Nanocomposites, Materials & Design 58 (2014) 527-534.

[44] M. Altan, Reducing Shrinkage in Injection Moldings Via the Taguchi, Anova and Neural Network Methods, Materials & Design 31(1) (2010) 599-604.

[45] B. Farshi, S. Gheshmi, E. Miandoabchi, Optimization of Injection Molding Process Parameters Using Sequential Simplex Algorithm, Materials & Design 32(1) (2011) 414-423.

[46] C.J. Tzeng, Y.K. Yang, Y.H. Lin, C.H. Tsai, A Study of Optimization of Injection Molding Process Parameters for SGF and PTFE Reinforced PC Composites Using Neural Network and Response Surface Methodology, Int J Adv Manuf Tech 63(5-8) (2012) 691-704.

[47] W.C. Chen, P.H. Liou, S.C. Chou, An Integrated Parameter Optimization System for MIMO Plastic Injection Molding Using Soft Computing, Int J Adv Manuf Tech 73(9-12) (2014) 1465-1474.

[48] W.C. Chen, G.L. Fu, P.H. Tai, W.J. Deng, Process Parameter Optimization for MIMO Plastic Injection Molding Via Soft Computing, Expert Syst Appl 36(2) (2009) 1114-1122.

[49] C. Garcia, M. Fittipaldi, L.R. Grace, Epoxy/Montmorillonite Nanocomposites for Improving Aircraft Radome Longevity, Journal of Applied Polymer Science 132(43) (2015) np-n/a.

[50] W.K. Loh, A.D. Crocombe, M.M. Abdel Wahab, I.A. Ashcroft, Modelling Anomalous Moisture Uptake, Swelling and Thermal Characteristics of a Rubber Toughened Epoxy Adhesive, International Journal of Adhesion and Adhesives 25(1) (2005) 1-12.

[51] L.R. Grace, The Effect of Moisture Contamination on the Relative Permittivity of Polymeric Composite Radar-Protecting Structures at X-Band, Composite Structures 128(0) (2015) 305-312.

[52] A.R. Berens, Diffusion and Relaxation in Glassy Polymer Powders: 1. Fickian Diffusion of Vinyl Chloride in Poly(Vinyl Choride), Polymer 18(7) (1977) 697-704.

[53] A.R. Berens, H.B. Hopfenberg, Diffusion and Relaxation in Glassy Polymer Powders: 2. Separation of Diffusion and Relaxation Parameters, Polymer 19(5) (1978) 489-496.

[54] S.A. Grammatikos, B. Zafari, M.C. Evernden, J.T. Mottram, J.M. Mitchels, Moisture Uptake Characteristics of a Pultruded Fibre Reinforced Polymer Flat Sheet Subjected to Hot/Wet Aging, Polymer Degradation and Stability 121 (2015) 407-419.

[55] M.H. Mondal, M. Mukherjee, Effect of Thermal Modification on Swelling Dynamics of Ultrathin Polymer Films, Polymer (United Kingdom) 53(22) (2012) 5170-5177.

[56] T.P. Hong, O. Lesaint, P. Gonon, Water Absorption in a Glass-Mica-Epoxy Composite I: Influence on Electrical Properties, Ieee Transactions on Dielectrics and Electrical Insulation 16(1) (2009) 1.

[57] J. Kim, C. Hu, R. Woo, M. Sham, Moisture Barrier Characteristics of Organoclay-Epoxy Nanocomposites, Composites Science and Technology 65(5) (2005) 805-813.

[58] W. Liu, S.V. Hoa, M. Pugh, Fracture Toughness and Water Uptake of High-Performance Epoxy/Nanoclay Nanocomposites, Composites Science and Technology 65(15) (2005) 2364-2373.

[59] A.P. Shah, R.K. Gupta, H.V.S. Gangarao, C.E. Powell, Moisture Diffusion through Vinyl Ester Nanocomposites Made with Montmorillonite Clay, Polymer Engineering & Science 42(9) (2002) 1852-1863.

[60] H.G. Carter, K.G. Kibler, Langmuir-Type Model for Anomalous Moisture Diffusion in Composite Resins, Journal of Composite Materials 12(2) (1978) 118-131.

[61] L.R. Grace, M.C. Altan, Non-Fickian Three-Dimensional Hindered Moisture Absorption in Polymeric Composites: Model Development and Validation, Polymer Composites 34(7) (2013) 1144-1157.

[62] Y. Weitsman, Diffusion With Time- Varying Diffusivity, With Application to Moisture- Sorption in Composites, Journal of Composite Materials 10(3) (1976) 193-204.

[63] A.C. Dumitru, F.M. Espinosa, R. Garcia, G. Foschi, S. Tortorella, F. Valle, M. Dallavalle, F. Zerbetto, F. Biscarini, In Situ Nanomechanical Characterization of the Early Stages of Swelling and Degradation of a Biodegradable Polymer, Nanoscale 7(12) (2015) 5403-5410.

[64] J. Yoon, S. Cai, Z. Suo, R.C. Hayward, Poroelastic Swelling Kinetics of Thin Hydrogel Layers: Comparison of Theory and Experiment, Soft Matter 6(23) (2010) 64-612.

[65] T. Tanaka, D.J. Fillmore, Kinetics of Swelling of Gels, The Journal of Chemical Physics 70(3) (1979) 1214.

[66] C. Wang, Y. Li, Z. Hu, Swelling Kinetics of Polymer Gels, Macromolecules 30(16) (1997) 4727-4732.

[67] D.A. Mountz, R.F. Storey, K.A. Mauritz, Fourier Transform Infrared/Attenuated Total Reflectance Analysis of Water Diffusion in Poly[Styrene-B-Isobutylene-B-Styrene] Block Copolymer Membranes, Journal of Polymer Science Part B-Polymer Physics 43(7) (2005) 764-776.

[68] M. Picardo, M. Ottaviani, E. Camera, A. Mastrofrancesco, Sebaceous Gland Lipids, Dermato-Endocrinology 1(2) (2009) 68.

[69] E. Oral, B.W. Ghali, A. Neils, O.K. Muratoglu, A New Mechanism of Oxidation in Ultrahigh Molecular Weight Polyethylene Caused by Squalene Absorption, Journal of Biomedical Materials Research Part B: Applied Biomaterials 100B(3) (2012) 742-751.

[70] L. Puppulin, W. Zhu, N. Sugano, G. Pezzotti, Microstructural Modifications Induced by Accelerated Aging and Lipid Absorption in Remelted and Annealed UHMWPEs for Total Hip Arthroplasty, Journal of Biomaterials Applications 29(6) (2015) 791-800.

[71] H. Sakoda, S. Niimi, Impact of Lipid-Induced Degradation on the Mechanical Properties of Ultra-High Molecular Weight Polyethylene for Joint Replacements, Journal of the Mechanical Behavior of Biomedical Materials 53 (2016) 218-225.

[72] V. Thomas, M. Jayabalan, A New Generation of High Flex Life Polyurethane Urea for Polymer Heart Valve - Studies on in Vivo Biocompatibility and Biodurability, Journal of Biomedical Materials Research - Part A 89(1) (2009) 192-205.

[73] A. Takahara, J. Tashita, T. Kajiyama, M. Takayanagi, Effect of Aggregation State of Hard Segment in Segmented Poly(Urethaneureas) on Their Fatigue Behavior after Interaction with Blood Components, Journal of Biomedical Materials Research 19(1) (1985) 13-34.

[74] A. Takahara, R.W. Hergenrother, A.J. Coury, S.L. Cooper, Effect of Soft Segment Chemistry on the Biostability of Segmented Polyurethanes. II. In Vitro Hydrolytic Degradation and Lipid Sorption, Journal of Biomedical Materials Research 26(6) (1992) 801-818.

[75] W. Yin, S. Gallocher, L. Pinchuk, R.T. Schoephoerster, J. Jesty, D. Bluestein, Flow-Induced Platelet Activation in a St. Jude Mechanical Heart Valve, a Trileaflet Polymeric Heart Valve, and a St. Jude Tissue Valve, Artificial organs 29(10) (2005) 826-31.

[76] S.L. Gallocher, A.F. Aguirre, V. Kasyanov, L. Pinchuk, R.T. Schoephoerster, A Novel Polymer for Potential Use in a Trileaflet Heart Valve, Journal of biomedical materials research. Part B, Applied biomaterials 79(2) (2006) 325-34.

[77] Q. Wang, A.J. McGoron, R. Bianco, Y. Kato, L. Pinchuk, R.T. Schoephoerster, In-Vivo Assessment of a Novel Polymer (SIBS) Trileaflet Heart Valve, Journal of Heart Valve Disease 19(4) (2010) 499-505.

[78] R.W. Baloh, A.W. Sills, W.E. Kumley, V. Honrubia, Quantitative Measurement of Saccade Amplitude, Duration, and Velocity, Neurology 25(11) (1975) 1065.

[79] C.J. Lueck, T.J. Crawford, H.C. Hansen, C. Kennard, Increase in Saccadic Peak Velocity with Increased Frequency of Saccades in Man, Vision Research 31(7) (1991) 1439-1443.

[80] J. Babcock, J. Pelz, Building a Lightweight Eyetracking Headgear, Proceedings of the 2004 Symposium on Eye tracking Research & Applications, San Antonio, Texas, 2004, pp. 109-114.

[81] G.E.P. Box, D.W. Behnken, Some New Three Level Designs for the Study of Quantitative Variables, Technometrics 2(4) (1960) 455-475.

[82] G.T. Lim, E.A. Foreman-Orlowski, S.E. Porosky, P. Pavka, J.E. Puskas, C. Gotz, V. Altstadt, Novel Polyisobutylene-Based Biocompatible Tpe Nanocomposites, Rubber Chemistry and Technology 82(4) (2009) 461-472.

[83] P. Antony, J.E. Puskas, M. Kontopoulou, Investigation of the Rheological and Mechanical Properties of a Polystyrene-Polyisobutylene-Polystyrene Triblock Copolymer and Its Blends with Polystyrene, Polym Eng Sci 43(1) (2003) 243-253.

[84] T. Morii, H. Hamada, Z.-i. Maekawa, T. Tanimoto, T. Hirano, K. Kiyosumi, Weight Change Mechanism of Randomly Oriented Gfrp Panel Immersed in Hot Water, Composite Structures 25(1) (1993) 95-100.

[85] M. Kellomäki, S. Paasimaa, D.W. Grijpma, K. Kolppo, P. Törmälä, In Vitro Degradation of Polyactive ® 1000peot70pbt30 Devices, Biomaterials 23(1) (2002) 283-295.

[86] A. Suzuki, T. Hara, Kinetics of One-Dimensional Swelling and Shrinking of Polymer Gels under Mechanical Constraint, Journal of Chemical Physics 114(11) (2001) 5012-5015.

[87] M. Fittipaldi, L.R. Grace, Lipid Diffusion and Swelling in a Phase Separated Biocompatible Thermoplastic Elastomer, Journal of the Mechanical Behavior of Biomedical Materials 64 (2016) 1-9.

[88] M. Fittipaldi, L.R. Grace, Lipid-Induced Degradation in Biocompatible Poly(Styrene-Isobutylene-Styrene) (SIBS) Thermoplastic Elastomer, Journal of the Mechanical Behavior of Biomedical Materials 68 (2017) 80-87.

[89] C. Tan, Y. Che Man, Differential Scanning Calorimetric Analysis of Edible Oils: Comparison of Thermal Properties and Chemical Composition, J Amer Oil Chem Soc 77(2) (2000) 143-155.

[90] T. Haryati, Y. Che Man, H. Ghazali, B. Asbi, L. Buana, Determination of Iodine Value of Palm Oil Based on Triglyceride Composition, Journal of American Oil Chemistry Society 75(7) (1998) 789-792.

[91] A. Mancini, E. Imperlini, E. Nigro, C. Montagnese, A. Daniele, S. Orru, P. Buono, Biological and Nutritional Properties of Palm Oil and Palmitic Acid: Effects on Health, Molecules, 2015, pp. 17339-17361.

[92] K.J. Kingsbury, S. Paul, A. Crossley, D.M. Morgan, The Fatty Acid Composition of Human Depot Fat, The Biochemical Journal 78 (1961) 541.

[93] M.A. Lampe, A.L. Burlingame, J. Whitney, M.L. Williams, B.E. Brown, E. Roitman, P.M. Elias, Human Stratum Corneum Lipids: Characterization and Regional Variations, Journal of Lipid Research 24(2) (1983) 120.

[94] L. Hodson, C.M. Skeaff, B.A. Fielding, Fatty Acid Composition of Adipose Tissue and Blood in Humans and Its Use as a Biomarker of Dietary Intake, Progress in Lipid Research 47(5) (2008) 348-380.

[95] A. Rohman, Y.B.C. Man, Fourier Transform Infrared (FTIR) Spectroscopy for Analysis of Extra Virgin Olive Oil Adulterated with Palm Oil, Food Research International 43(3) (2010) 886-892.

[96] B. Babaei, A. Davarian, K.M. Pryse, E.L. Elson, G.M. Genin, Efficient and Optimized Identification of Generalized Maxwell Viscoelastic Relaxation Spectra, Journal of the Mechanical Behavior of Biomedical Materials 55 (2016) 32-41.

[97] R.W. Ogden, Large Deformation Isotropic Elasticity - on the Correlation of Theory and Experiment for Incompressible Rubberlike Solids, Proceedings of the Royal Society of London. Series A, Mathematical and Physical Sciences 326(1567) (1972) 565-584.

[98] Y. Li, J. Miranda, H.J. Sue, Moisture Diffusion Behavior in Bismaleimide Resin Subjected to Hygrothermal Cycling, Polymer Engineering & Science 42(2) (2002) 375-381.

[99] J.H. Perez, F. Tanaka, T. Uchino, Comparative 3d Simulation on Water Absorption and Hygroscopic Swelling in Japonica Rice Grains under Various Isothermal Soaking Conditions, Food Research International 44(9) (2011) 2615-2623.

[100] J. Zhou, J.S. Law, Effect of Non-Uniform Moisture Distribution on the Hygroscopic Swelling Coefficient, Ieee T Compon Pack T 31(2) (2008) 269-276.

[101] E.H. Wong, R. Rajoo, S.W. Koh, T.B. Lim, The Mechanics and Impact of Hygroscopic Swelling of Polymeric Materials in Electronic Packaging.(Abstract), Journal of Electronic Packaging 124(2) (2002) 122.

[102] E. Stellrecht, B. Han, M. Pecht, Measurement of the Hygroscopic Swelling Coefficient in Mold Compounds Using Moiré Interferometry, Experimental Techniques 27(4) (2003) 40-44.

[103] C. Jang, S. Yoon, B. Han, Measurement of the Hygroscopic Swelling Coefficient of Thin Film Polymers Used in Semiconductor Packaging, Ieee T Compon Pack T 33(2) (2010) 340-346.

[104] S.A. Chester, L. Anand, A Coupled Theory of Fluid Permeation and Large Deformations for Elastomeric Materials, Journal of the Mechanics and Physics of Solids 58(11) (2010) 1879-1906.

[105] Y. Liu, H. Zhang, Y. Zheng, A Multiplicative Finite Element Algorithm for the Inhomogeneous Swelling of Polymeric Gels, Computer Methods in Applied Mechanics and Engineering 283 (2015) 517.